DISS. ETH Nr. 13803

Measurement of
WW production cross section
and
mass of the W boson

Dissertation submitted to the
SWISS FEDERAL INSTITUTE OF TECHNOLOGY ZURICH

for the degree of
Doctor of Natural Sciences

presented by
Artur J. Barczyk

Dipl.–Phys. ETH-Zürich

born December 25th, 1969
in Warsaw, Poland
Citizen of Switzerland (from Herisau AR) and Poland

Accepted on the recommendation of

Prof. Dr. H. Hofer   examiner
Prof. Dr. A. Rubbia   co-examiner
PD Dr. M. Pohl   co-examiner

- 2000 -

Abstract

In this thesis, the analysis of data collected by the L3 experiment in 1997 and 1998 is presented. A tool was developped for selection of $e^+e^- \to WW \to qq\mu\nu$ events, with the goal of measurement of the cross section of this process. The data samples were collected at the centre-of-mass energies of $\sqrt{s} = 183$ and 189 GeV, with the collected luminosities of 55.5 pb^{-1} and 176.8 pb^{-1}, respectively. The measured cross sections at these energies are

$$\sigma_{qq\mu\nu}^{\sqrt{s}=183 \text{ GeV}} = 2.09 \pm 0.23(stat.) \pm 0.05(syst.) \text{ pb}$$

$$\sigma_{qq\mu\nu}^{\sqrt{s}=189 \text{ GeV}} = 2.26 \pm 0.14(stat.) \pm 0.03(syst.) \text{ pb}.$$

Both values are in good agreement with the Standard Model prediction.

The data selected in all semileptonic channels as well as in the fully hadronic final state was used for the measurement of the mass of the W boson. A new method based on maximum likelihood fit was evaluated for this purpose for a first time in experimental environment. The high statistics data sample collected at $\sqrt{s} = 189$ GeV was used to extract the W mass, with the result of

$$M_{\text{W}} = 80.33 \pm 0.10(stat.) \pm 0.07(syst.) \text{ GeV}.$$

The method makes use only of quantities which are directly measured in the experimental apparatus. Semi-analytical expressions for the differential cross section with respect to these variables are evaluated on event-by-event basis to construct the probability density function. The detector effects are taken into account by folding the differential cross section with the detector response functions determined for the chosen variables. Since the set of variables was chosen such as to optimize the effect of the detector resolutions, this procedure is well suited for a high precision measurement of the W boson mass.

Zusammenfassung

Die vorliegende Arbeit stellt die Analyse der Daten vor, die gesammelt wurden von dem L3-Experiment in den Jahren 1997 und 1998. Es wurde ein Selektionsprogramm entwickelt, um die Ereignisse des Processes $e^+e^- \rightarrow WW \rightarrow qq\mu\nu$ zu analysieren, mit dem Ziel, dessen Wirkungsquerschnitt zu messen. Die Daten wurden gesammelt bei Schwerpunktsenergien von $\sqrt{s} = 183$ und 189 GeV, wobei die gesammelten Luminositäten jeweils 55.5 pb^{-1} und 176.8 pb^{-1} betragen. Der gemessene Wirkungsquerschnitt bei diesen Energien beträgt

$$\sigma_{qq\mu\nu}^{\sqrt{s}=183 \text{ GeV}} = 2.09 \pm 0.23(stat.) \pm 0.05(syst.) \text{ pb}$$

$$\sigma_{qq\mu\nu}^{\sqrt{s}=189 \text{ GeV}} = 2.26 \pm 0.14(stat.) \pm 0.03(syst.) \text{ pb}.$$

Beide Werte stimmen sehr gut mit den Vorhersagen des Standard-Models überein.

Die gesammelten Daten aller semi-leptonischer Zerfallskanäle sowie auch des vollständig hadronischen Endzustandes wurden dann für die Messung der Masse des W bosons benutzt. Eine neue Methode, basierend auf der Methode des 'maximum likelihood fit' wurde zum ersten Mal in einer Experimentellen Umgebung angewandt und ausgewertet. Dazu wurden die Daten benutzt, die bei der Schwerpunktsenergie von $\sqrt{s} = 189$ GeV selektiert wurden. Die gemessene W-boson Masse beträgt

$$M_{\text{W}} = 80.33 \pm 0.10(stat.) \pm 0.07(syst.) \text{ GeV}.$$

In dieser Methode werden nur diejenigen Grössen benutzt, die im Experiment direkt gemessen werden. Semi-analytische Ausdrücke für den differentiellen Wirkungsquerschnitt bezüglich dieser Variablen wurden ausgewertet für jedes der selektierten Ereignisse, um die Wahrscheinlichkeitsdichtenfuntion zu bilden. Detektoreffekte wurden berücksichtigt mittels faltung des differentiellen Wirkungsquerschnittes mit den Auflösungsfuntionen. Die Variablen wurden ausgewählt mit dem Ziel, den Einfluss der Detektor-auflösung zu minimieren, wodurch die Methode bestens geeignet ist, eine Präzisionsmessung der Masse des W-Bosons durchzuführen.

Contents

List of Figures

Chapter 1

Introduction

The direct observation of the W and Z bosons by the UA1 [2] and UA2 [3] collaborations marked a milestone in the verification of the electroweak theory, first proposed by Glashow, Weinberg and Salam [1]. Within this theory, spin $\frac{1}{2}$ fields (fermions) representing quanta of matter interact with each other by means of exchange of particles with spin 1 (bosons). It unifies the electromagnetic force with its massless vector boson, the photon, and the weak interaction mediated by the massive bosons Z and $W^\pm$.

The mass of the elementary particles (fermions as well as vector bosons) is given by the strength of their couplings to the Higgs field, postulated by P.Higgs in [4]. Together with Quantum Chromodynamics, the theory of strong interaction, the electroweak theory forms the Standard Model of elementary particle interaction.

So far, no significant deviation from the predictions given by the Standard Model have been found experimentally. The Higgs particle itself, the mass of which is not predicted by the theory and can be constrained only by experimental data from measurements of various Standard Model parameters, has so far evaded direct observation. Should the Higgs mechanism be indeed incorporated by nature, the model will be left with many a priori unknown parameters such as the masses of the fermions and bosons and the couplings among them, which can be only determined in experimental way. The quest for the Higgs particle itself is nowadays accompanied by high precision measurements of these parameters.

Of particular interest is the measurement of the masses of the Z and W bosons. The Z mass was measured to high degree of precision at the LEP and SLC colliders through the electron-positron annihilation process $e^+e^- \rightarrow Z/\gamma \rightarrow f\bar{f}$ [5]. Until 1996, the mass of the W boson could only be measured at $p\bar{p}$ colliders at CERN and FNAL. Due to the unknown effective energy in parton-parton interaction, only the transverse mass of the W could be measured, and the W mass was derived from a fit to Monte Carlo prediction as a function of M_W. Clearly, a lepton collider with a precisely known centre-of-mass energy allows for a more precise determination of the W mass. The most precise measurement of the W mass today is obtained from the invariant mass spectrum of the W decay products in the process $e^+e^- \rightarrow W^+W^- \rightarrow f\bar{f}f\bar{f}$.

In its simplest form with two doubletts, the Higgs sector of the Standard Model relates the W and Z masses to the weak mixing angle θ_W: $\sin^2 \theta_W = 1 - M_W^2/M_Z^2$. Also, the W mass is connected through radiative correction to the mass of the Higgs boson and the top quark. With no a priori theory prediction for the masses of the vector bosons, the importance of a precision measurement of these fundamental parameters of the Standard Model becomes obvious: on the one hand, yet another consistency check of the model is performed, while, together with the measurement of the top mass at TEVATRON, a constraint can be put on the mass of the Higgs

boson.

Another interesting aspect of the Standard Model is the self-interaction among gauge bosons. The non-abelian structure of the theory predicts the existence of self-couplings of the electroweak fields, a prediction which can be tested in W pair production in two ways: first, the shape of the cross section depends strongly on the existence of diagrams with vertices of three bosons, and, secondly, the coupling strength can be measured in a direct way. Both, the WW cross section, as well as the couplings of the W boson to Z and γ are well predicted by the theory, and any measured deviation would indicate physics beyond the currently valid Standard Model.

This thesis deals with two of the above mentioned topics: the measurement of the cross section of the process $e^+e^- \rightarrow WW \rightarrow f\bar{f}f\bar{f}$ with one of the Ws decaying in a pair of quarks, e.g. $W^- \rightarrow \bar{u}d$, and the other one in a muon-neutrino pair. This measurement performed at centre-of-mass energies of $\sqrt{s} = 183$ and 189 GeV is presented in chapter 5. The second part deals with the measurement of the W boson mass using the data collected at $\sqrt{s} = 189$ GeV, and is described in chapter 6. Basis for both these measurements is of course the event selection, which is presented in chapter 4 for the case of $e^+e^- \rightarrow WW \rightarrow qq\mu\nu$ final state.

Chapter 2

Experimental Apparatus

In this section, a description of the LEP collider and the L3 experiment is given.

2.1 The LEP Collider

The Large Electron Positron collider (LEP, c.f. Fig. 2.1) was built at CERN to study electron-positron collisions at centre-of-mass energies between 90 and $\sim$ 200 GeV. After several years of running at the Z pole, LEP started it's second phase of operation in 1995 with a run at $\sqrt{s} = 130$ GeV. Since then the energy has been steadily increased to reach $\sqrt{s} = 202$ GeV in 1999. During this time, LEP was operating in a mode with four bunches of electrons and four positron bunches. The peak luminosity reached was $\mathcal{L} = 1.2 \times 10^{32} \text{cm}^{-2}\text{s}^{-1}$.
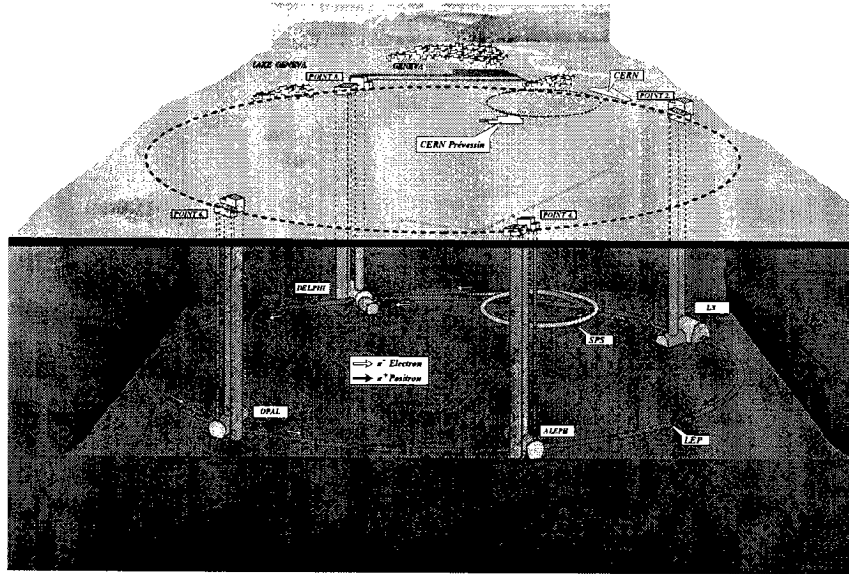
Figure 2.1: A view of the LEP collider area.

There are four detectors ALEPH [6], DELPHI [7], L3 [8] and OPAL [9] installed at LEP, located at the four interaction points where the beams are brought to collision.

2.2 The L3 Detector

The L3[1] detector was designed as a general purpose detector for physics at LEP. A schematic view of the detector is shown in Fig. 2.2. With a high resolution electromagnetic calorimeter and large volume muon chambers, emphasis was laid on precise measurement of electrons, photons and muons. The main subdetectors are the central tracker, the electromagnetic and hadron calorimeters, the muon spectrometer and the luminosity monitor. The whole detector, apart from the forward/backward muon chambers, is located inside a magnet generating solenoidal field of 0.5T along the beam direction. Windings around the magnet doors generate a 1.24T toroidal field therein, necessary for momentum measurement of muons going in the forward/backward direction.
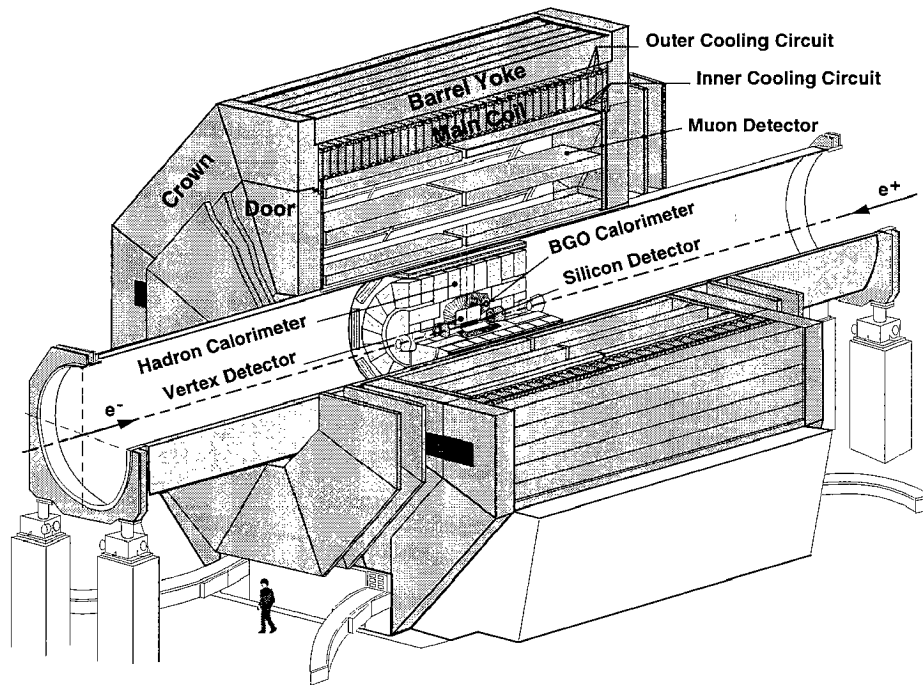
Figure 2.2: The L3 detector.

2.2.1 The Central Tracker

The central track detector consists of a Silicon Microstrip Detector (SMD), a Time Expansion Chamber (TEC), and a proportional chamber for position measurement along the beam direction (Z-chamber).

The SMD [11] contains two cylindrical layers of double sided silicon detectors, the inner sensor plane with a radius of 6cm and the outer sensor plane with a radius of 8cm. Each sensor plane is built of 12 modules, the so-called ladders. Due to an overlap of the ladders in the inner sensor plane, there are at most three possible SMD hits for one track. The resolution of the SMD is 9.8μm in the $R - \phi$ plane and 36.1μm in the Z direction [12].

---

[1]The letter of intent submitted to the LEP experiment committee was the third one, this fact giving the experiment its name.

The Time Expansion Chamber [13], used for the measurement of charged particle momenta, is a special type of drift chamber with an additional plane of grounded grid wires between the anode and cathode plane, as illustrated in Fig. 2.3. This grid plane divides the chamber in two regions: the drift region and the detection or amplification region. The detection region works with a high field strength to generate a measurable signal on the anode wires. In the drift region, a weak and homogeneous field is required, in order to get a low drift velocity. This results in an improved space and double track resolution - a single hit resolution of $50\mu m$ has been achieved through the use of a low diffusion drift gas (a mixture of 80% CO_2 and 20% C_4H_{10}) and by determining the drift time with a centre-of-gravity method.
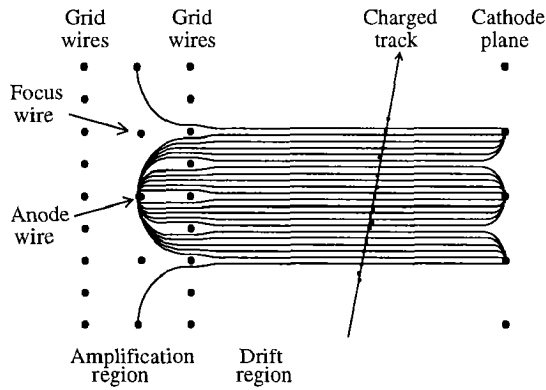
Figure 2.3: The TEC principle. Grid wires divide the region between anode and cathode planes into amplification region with high field strength, and the drift region with low field strength and thus low drift velocity.
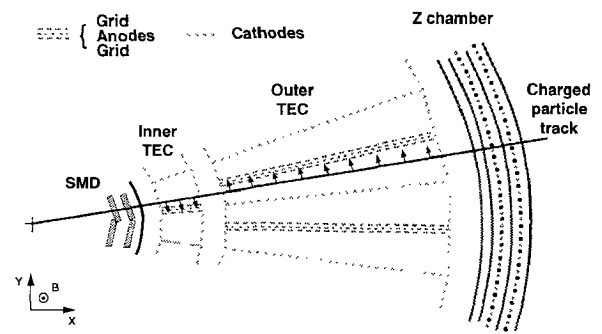
Figure 2.4: A schematic view of one inner and two outer sectors of the TEC. Cathode planes act as borders of one sector, the anode plane dividing a sector in two half-sectors.

The L3 TEC design [10] is illustrated in Fig. 2.4. The chamber has an outer radius of 457mm and is divided in two concentric rings, the Inner TEC (TECI) and the Outer TEC (TECO). TECI consists of 12 sectors with 8 anodes per sector, while TECO has 24 sectors with 54 anodes each. This special arrangement is used to solve the problem of mirror tracks - using only outer TEC hits, it is a priori impossible to tell which half-sector the drift electrons originate from. Matching TECI hits solve this ambiguity.

The distance between the innermost anode in TECI and the outermost anode in TECO is 317mm, which is thus also the maximum measurable track length in the TEC.

For the measurement of the Z coordinate, a separate subdetector, the Z-chamber was installed around the TEC. It consists of two cylindrical proportional chambers with cathode pad readout, and has a Z resolution of $320\mu m$.

2.2.2 Electromagnetic Calorimeter

The electromagnetic calorimeter (ECAL) [14] is built of ~ 11000 scintillating bismuth germanium oxide (BGO, $Bi_4Ge_3O_{12}$) crystals of 24 cm length, corresponding to 22 radiation lengths. Signal readout is achieved using two silicon photodiodes at each BGO crystal.

11

The crystals have a pyramidal shape with 2×2 cm^2 cross section at the inner and 3×3 cm^2 at the outer end. They are arranged in two parts: the barrel region surrounding the TEC, and two endcaps, as shown in Fig. 2.5. Together they cover a polar angular range of $0.98 > |\cos\theta|$ with a gap at $0.72 < |\cos\theta| < 0.80$.

The spatial resolution of electromagnetic showers in the ECAL is 2 mm at an energy $E > 2$ GeV. The energy resolution is 5% at 100 MeV and is decreasing down to 1% above 2 GeV.

A lead-scintillating fibre calorimeter [15] was installed in order to fill the gap between the barrel and endcap regions.

2.2.3 The Luminosity Monitor

For the measurement of the luminosity, low angle Bhabha scattering, $e^+e^- \to e^+e^-(\gamma)$ is used, since this cross section can be calculated with high precision from QED. A detector with well known geometry, high trigger efficiency and full coverage of the azimuthal angle is necessary for precise measurement of the luminosity. Such a detector was implemented in L3 [22], consisting of a BGO calorimeter with very good energy resolution and high trigger efficiency, and a silicon tracker (SLUM). The arrangement can be seen in Fig. 2.5. The luminosity monitor is positioned at small polar angle, i.e. in an angular region where the Bhabha cross section is higher than the hadron production cross section, and the interference between the photon and Z exchange diagrams is small, thus reducing the systematic uncertainties on the measurement.
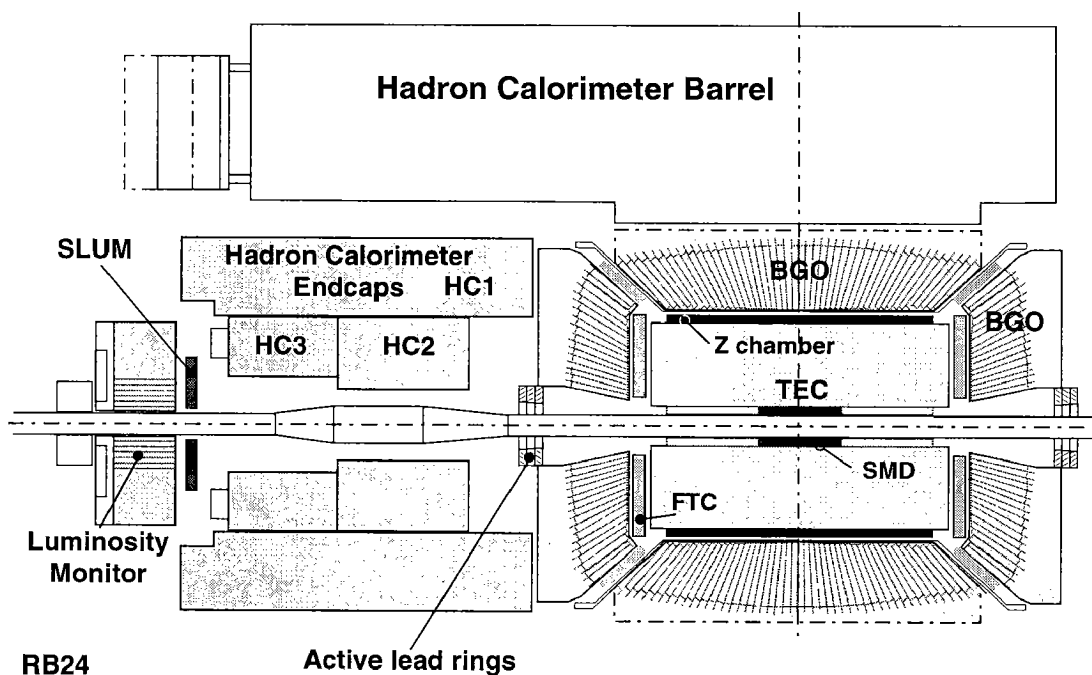
Figure 2.5: Side view of the L3 central detector part, showing the position of the BGO electromagnetic calorimeter, the hadron barrel and endcap calorimeter. Also shown is the luminosity monitor with its silicon tracker (SLUM).

Energy measurement in the luminosity BGO calorimeter is used to select high purity sample of events, while the SLUM tracker guarantees a selection in a precisely defined fiducial volume.

This high precision detector enabled a luminosity measurement with an accuracy of 0.07% during the $\sqrt{s} = 189$ GeV run.

2.2.4 Scintillation Counters

30 barrel and 32 endcap scintillators [16] are located between the electromagnetic and hadron calorimeters, and cover together the region $|\cos\theta| < 0.98$. The time resolution is 0.8 ns in the barrel, and 1.9 ns in the endcap region. The measured scintillator times are mainly used to reduce the cosmic ray background by time-of-flight measurement of muons and for triggering of high multiplicity events as described in Sec. 2.3.1. While LEP was running in bunch train mode, the scintillator counter system was also used for bunch tagging.

2.2.5 Hadron Calorimeter

The Hadron Calorimeter (HCAL) [17] consists of depleted uranium plates interspersed with proportional chambers. Uranium has beed chosen as absorber material due to its short hadronic absorption length. The HCAL is built in two parts: the barrel and the endcap region, which cover together the angular region of $5.5° < \theta < 174.5°$. The jet energy resolution obtained is 10.2% in the central region and 13.8% in the forward/backward region. Together with the surrounding muon filter (brass absorber plates interspersed with proportional tubes), the HCAL acts also as a shield of the muon system against hadronic particles, and can be used for identification of minimum ionizing particles which have a typical energy loss of ~ 2 GeV in the HCAL (c.f. App. A).

2.2.6 The Muon Spectrometer

The muon detector in L3 consists of two distinct parts: the barrel and the forward/backward muon chambers. A side view of the detector is shown in Fig. 2.6, where the two parts can be seen.

The barrel muon detector [18] has a polar angle coverage of $44° \leq \theta \leq 136°$. It is arranged in eight octants, each octant containing three layers of drift chambers (MI, MM and MO) for measurement in $R - \phi$ plane (called P-chambers), as shown in Fig. 2.7. For technical reasons, the whole chambers were built in two parts along the beam direction, and also, the big MM and MO chambers are subdivided in two parts each, as can be seen in Fig. 2.7. The chambers are arranged in cells with 16 (MI, MO chambers) or 24 (MM chambers) sense wires each. One layer is built of 19, 30 and 42 cells in the MI, MM, and MO, respectively.

For the measurement in the $R - Z$ plane, there are four layers of Z-chambers (II, IM, OM, OO) attached to the inner and outer side of the MI and MO chambers. These chambers consist of two layers of rectangular drift tubes.

A hit in a cell of a P-chamber consists of several wires being hit, and results in a measurement of a point on and local slope of the muon track. For the muon momentum reconstruction, at least two cells must be hit in different layers. In the barrel region, a circular fit to three space points given by the hit cells is performed for a muon track having all three layers hit, while in the two hits case, also the slopes at both segments must be used. The large lever arm of 2.9m makes a precision measurement of the muon momentum possible with a resolution of 2.5% at 45 GeV in the case of a triplet muon track, and 21.3% in the case of a doublet [19].

The forward/backward muon detector [20] consists of three layers of drift chambers, one being mounted on the inside of the magnet door, two on the outside, c.f. Fig. 2.6. Each

13
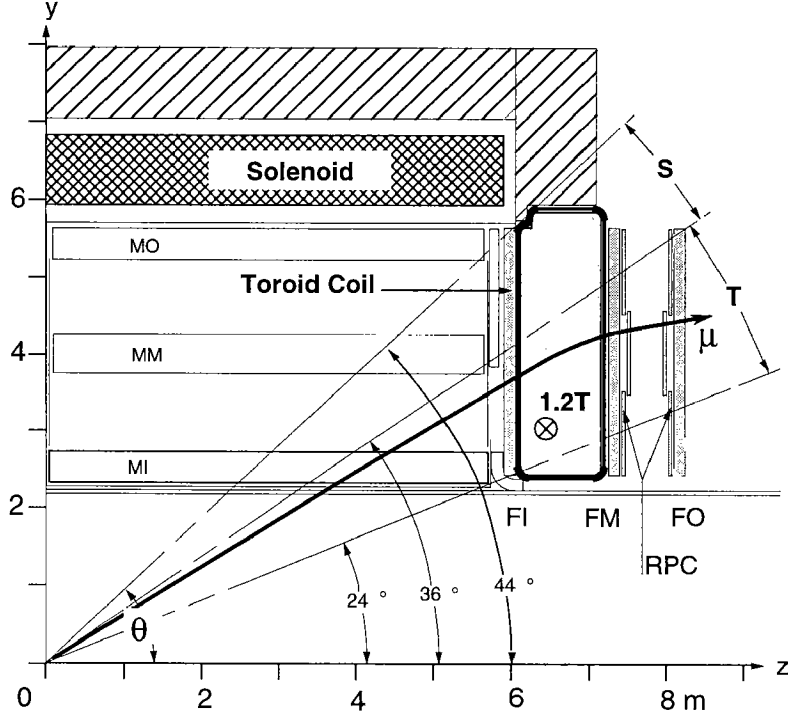
Figure 2.6: Side view of one quater of the L3 muon detector. Visible are the two parts: barrel muon chambers, containing the MI, MM and MO layers; as well as the forward/backward muon chambers with the FI, FM and FO layers. Also shown are the resistive plate chambers used for triggering.

chamber is built of three layers (Y, X, W), with W and X performing a measurement in the $R - \phi$ plane, and the Y chamber in the $R - Z$ plane. Between the outer two layers, resistive plate counters (RPC) [21] are installed for triggering purposes.

The momentum resolution of the forward/backward muon detector varies with the polar angle, and ranges from $\sim 4\%$ for tracks having also hits in the MI and MM chambers (barrel), down to $\sim 30\%$ for very forward tracks. The latter value is limited by multiple scattering in the magnet door, which is located between the inner and the two outer detector layers.

The barrel and forward/backward detectors together cover a polar angular region of $|\cos\theta| <$ 0.91. Due to gaps at $\theta = 90°$ and at the boundaries of the octants, the muon detector covers $\sim 85\%$ of the full solid angle.

2.3   Trigger and Data Acquisition System

The purpose of the L3 trigger and data acquisition system is to select, digitize, assemble and record events from e^+e^- interactions at LEP.

Analog signals from detector front end have to be converted to numerical data, and read out at high speed, in order to fully exploit the luminosity delivered by LEP. The modularity of the L3 detector allows for parallel data taking in various parts of the DAQ system, maximizing its throughput. With LEP operating in four bunch mode, the beams cross each other with 45 kHz frequency. Not every beam crossing results in a e^+e^- collision. In fact, the expected physics

14
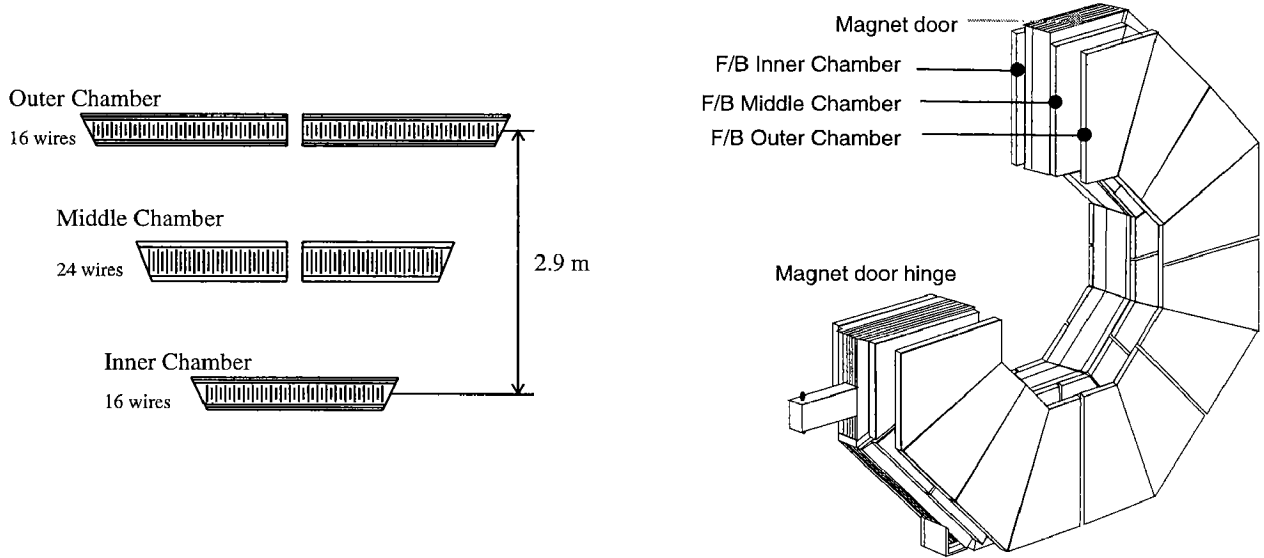
Figure 2.7: $R - \phi$ view of one muon chamber octant on the left, and schematic view of the forward/backward muon chambers (right).

event rate at $\sqrt{s} = 189$ GeV and a luminosity of $10^{32}\text{cm}^{-2}\text{s}^{-1}$ lies around 3 Hz. The purpose of the trigger system is therefore to decide with high efficiency whether the beam crossing resulted in a physics event, while rejecting noise events. The sources of the latter could be of various nature: electronic noise, beam particles hitting remnant gas inside the beam pipe, synchrotron radiation hitting beam pipe walls and also cosmic radiation muons passing the detector. The trigger system is built in threee stages, with first and second level triggers evaluating coarse subdetector data, whereas the third level trigger uses the full detector readout to make its decision. It also has access to the level 1 and 2 trigger data for monitoring purposes.

The structure of the trigger and data acquisition system is shown in Fig. 2.8. The four main subdetectors (tracker, electromagnetic calorimeter, hadron calorimeter, muon chambers) each have their own readout chain, readout and ditization being performed in parallel upon reception of positive level 1 trigger decision. The fifth chain running in parallel is the trigger stream up to second level trigger. The data in this stream has coarser granularity in order to make the decision time short. The central event builder combines and synchronizes the data arriving from the subdetector and trigger readout chains, and passes then the complete event to the third level trigger for final decision and storage.

The system is built in FASTBUS technology, with four subdetector segments plus one central segment. It is controlled by tasks running on a cluster of VAX computers.

2.3.1 First Level Trigger System

There are five independent first level triggers: TEC trigger, inner TEC trigger, scintillator multiplicity trigger, muon trigger and energy trigger. All of them use coarse (trigger) data, with the requirement of decision being taken before the next beam crossing, i.e. within less than $22.2\mu s$.

The whole level 1 trigger system is controlled by the trigger control logic, which also is
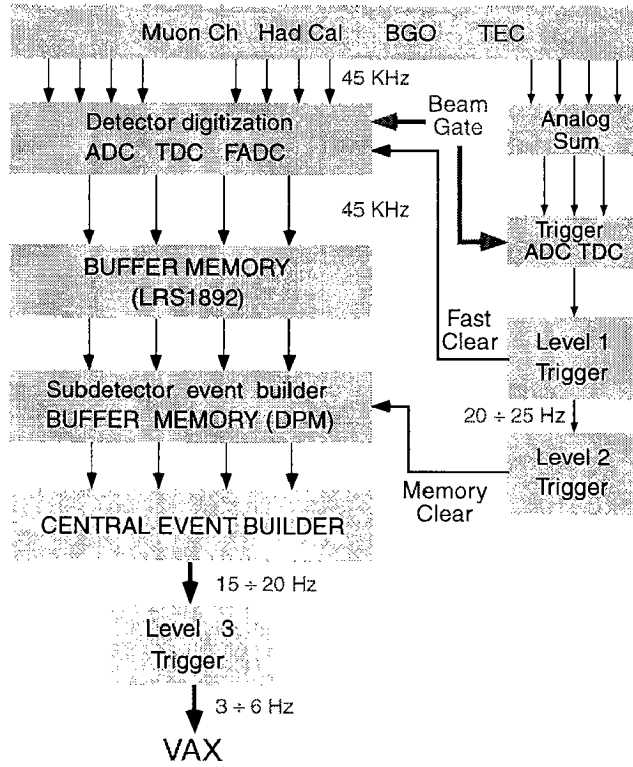
Figure 2.8: Overview of the L3 DAQ system.

responsible for the time synchronization of the whole DAQ system. The timing diagram is shown in Fig. 2.9. The absolute time zero of the system is defined as the time when the beam bunches pass the interaction point. The positron bunches passing by a beam pickup induce a signal which appears at discrimator output 75ns after the beam crossing. This signal is available in two forms: ungated (GATE0), which comes every $22.2\mu s$, i.e. every beam crossing, and gated (GATE1), which is disabled while the DAQ system is busy.

An accurate digital delay generator is triggered by the beam crossing signal, and generates a delayed signal which precedes the next beam crossing by $2.1\mu s$. Upon reception of this signal, trigger control takes one of the following steps:

i. If an event has been accepted, trigger control checks the READY status of the subdetectors. If all subdetectors have finished readout of the event data, it sends a CLEAR to reset all the trigger and subdetectors to start a new data acquisition cycle. If the DAQ is not ready yet, it does nothing and waits for the next cycle.

ii. If a new DAQ cycle has been just started, then the trigger control checks the level 1 trigger results, and compares it with a trigger mask which has been sent to it during initialization at the beginning of a fill. If the decision is positive, trigger control sends an ACCEPT signal to all subdetectors, and inhibits any further data acquisition cycles. At next cycle, it continues with step i. If the decision is negative, it sends out a CLEAR signal to fast clear the trigger and DAQ system, and starts a new cycle.

ACCEPT and CLEAR signals are sent about $1.74\mu s$ before the next beam crossing, such as to allow for enough time for the subdetectors to take corresponding action, and be ready for next beam crossing if the current event was rejected. After the ACCEPT signal is sent, the following

16
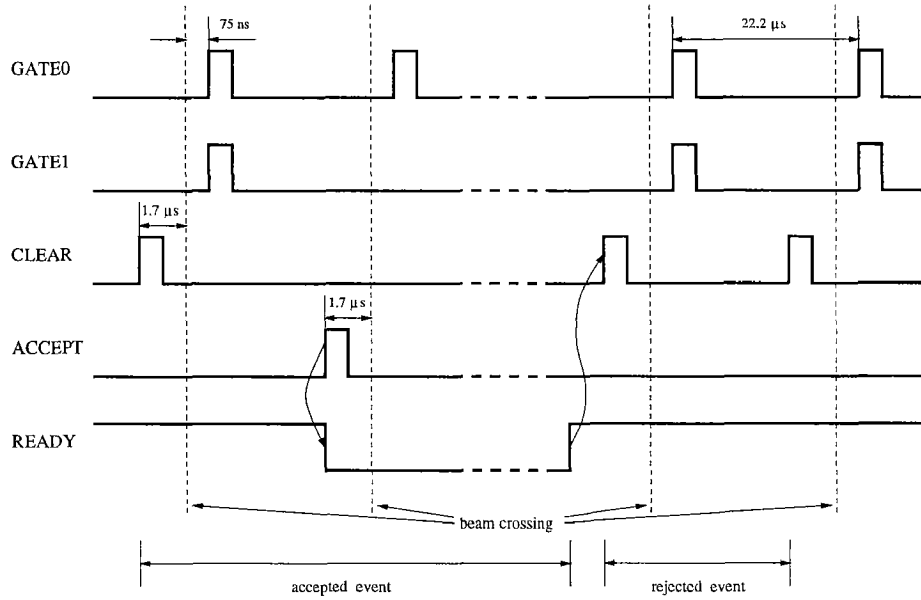
Figure 2.9: Trigger control logic timing diagram.

gated beam crossing (GATE1) and CLEAR signals will be disabled to allow subdetectors to finish the data readout. Subdetectors respond to the ACCEPT signal by negating a READY signal for the time they are busy with data acquisition. Trigger control waits for at least 300μs before it starts to check the READY status of the subdetectors. Any delay in data acquisition will be propagated in this way to the trigger control, which will hold the DAQ cycle until all subdetectors are ready. This ensures data integrity under all circumstances.

200ns after the ACCEPT signal, trigger control also sends two data words to all subdetectors together with a STROBE signal. The first word contains an event number, which is incremented with every ACCEPT, and is used for synchronization of subdetector data at higher DAQ levels. The second word contains a trigger bit pattern, in which every level 1 trigger has its corresponding bit set if its decision is positive. This pattern is used in the second and third level triggers.

TEC Trigger

The TEC trigger [25] selects events with charged particle tracks in the central tracker. It processes the analog signals from 14 out of the 54 anode wires of the outer TEC sectors. The decision is obtained in three steps:

i. The discriminated analog signals are digitized, and a hit pattern is produced in the $R - \phi$ projection. Each sector is divided in four (trigger) subsectors.

ii. A search for tracks in the subsectors is performed based a lookup-table technique. This very fast method is applied in all 96 subsectors simultaneously.

iii. The trigger decision is taken based on the total number of tracks and number of pairs of coplanar tracks.

The system is very flexible, with all parameters being programmable, and searches possible for tracks contained in several subsectors.

Inner TEC Trigger

The inner TEC trigger [26] was added to the L3 DAQ system in 1996. It is using the information from the eight signal wires in each inner TEC sector. The trigger is based on a neural network approach, implemented in custom-built hardware modules [27], which implements a feed-forward network with 55 input, 2 hidden and one output node. A neural network model to classify one inner TEC sector according to the quality of tracks inside was established, and a 12-fold replication thereof enables a parallel evaluation of hits in the complete inner TEC detector. The neural network was trained to select good sectors in a most general way. Samples of selected Bhabha events, selected $e^+e^- \rightarrow q\bar{q}$ events, MC generated $\gamma\gamma$ events and beam-gate events[2] were used for training. The latter sample represent events which have to be rejected by the trigger.

For the final selection, the inner TEC sectors are classified depending on the number of wires without any hit, and if they have less than 4 of those, triggered sectors are chosen to be 'good' if the neural network output is above a predefined threshold, otherwise they are labelled 'bad'. Positive trigger decision is reported if there are at least two 'good' sectors, and there are more 'good' than 'bad' sectors. A coincidence with at least one outer TEC track found by the TEC trigger is also required.

Scintillator Trigger

The scintillator multiplicity trigger [16] requires a time coincidence of 5 out of the 16 scintillator pairs in the barrel part. It is used to select high multiplicity events. Apart of this trigger, scintillator data is used in the muon (both barrel and forward/backward) trigger.

Muon Trigger

The muon trigger consists of two distinct parts: the Barrel Muon Trigger [28] and the Forwad/Backward Muon Trigger. The two parts act independent of each other in terms of trigger decision, nevertheless, intermediate results are sent from the Barrel Trigger to the Forward/Backward Trigger, since some subtriggers of the latter are using coincidence with tracks in the barrel part of the detector.

Barrel Muon Trigger

Amplified and discriminated signals from the barrel muon chambers are picked up for trigger purposes before they are encoded by the TDCs. The number of channels is reduced by performing a logical OR of two adjacent wires in a cell (for the P-chambers) or two cells (in the case of Z-chambers, which have just one wire per cell). For this purpose, a special FASTBUS Auxiliary Function Card was developped, the so called Muon Personality Card (MPC) [29]. One MPC is connected to a TDC from which it receives the data via the Auxiliary Connector. The memory on this card is enabled for writing during $1.3\mu s$ and $2.41\mu s$ for P and Z-chambers, respectively. This time corresponds to the characteristic drift time of the muon chambers.

The data stored in the MPCs is read out by a FASTBUS module, the Personality Card Controller (PCC) [29] via a 48 bit wide data bus linking all the MPCs of one octant. All modules receiving data from one octant of P-chambers occupy one FASTBUS crate, while two Z-chamber octants are hosted in one crate. In both cases, there is one PCC per octant. The

---

[2]Beam-gate events are events which are triggered on the beam gate only, i.e. despite negative level 1 decision. These events are mainly used for monitoring of the level 1 triggers.

PCCs reorganize the data according to trigger cell structure, compare the number of hits in a cell with a threshold value, and send out the layer and cell number of any cell above threshold to the muon trigger processor. The same information is also sent to the second level trigger.

The PCC possesses the ability of disabling noisy wires as well as compensating for dead wires: at the input of the PCC, a logical AND is performed with a preprogrammed 'enable' pattern, as well as an OR operation with a 'set' pattern. These patterns are stored in the PCC for every MPC in a so called compensation memory, which consists of eight banks: 'AND compensation' (four banks) and 'OR compensation' memory (four banks).

The input from MPC has to be mapped onto the physical structure of the muon chambers. For this purpose, the PCCs contain a cell size memory. This enables very flexible configuration, with the possibility even to split muon chamber cell wires between different MPCs.

After the data has been formatted according to the cell structure, the number of hits in every cell is counted in a two stage adder and compared with the threshold. The threshold values for P-chamber cells are set to 2, and to 1 for Z-chambers. They can be set for every cell independently, thus enabling to set a higher threshold for noisy cells, or even, when set to zero, to always enable a certain cell.

The ouput of the comparators is fed into a scanner unit which serializes the up to this point parallel data. It also reformats the data in order to get a layer and cell number with the corresponding number of hits. This setup is stored in a reformat memory inside the PCC module.

Fig. 2.10 shows the readout chain with the example of one MI or MO cell (16 wires) and one MM cell (24 wires).

The cell size, compensation, reformat and threshold memories are accesible via FASTBUS and are downloaded to the PCCs during initialization, i.e. at the beginning of every fill.

The processing of the data in the PCCs is done in parallel for each octant, and simultaneously for P and Z-chambers. 16 parallel ECLine buses (8 for P-chambers and 8 for Z-chambers) connect the PCCs with the trigger processor for data transfer. The layer and cell number of each cell above threshold is put on the bus by the PCC, and is seen by three (four) Data Arrays corresponding to the three (four) layers of P (Z) chambers. The data array, the layer of which corresponds to the layer number put on the bus, picks up the data, and stores a '1' at the memory location assigned to the cell number following on the bus. In this way, the data arrays represent a map of the muon chambers' cell structure in a digital memory.

The 'processor unit' of the muon trigger consists of a number of Programmable Logic Units, registers to store intermediate data, Memory Lookup Units plus some additional ECLine logic modules.

Triggered by the All Data In (ADI) signal from the PCCs, the PLUs access the data stored in the data arrays to check for track patterns in the $R - \phi$ and $R - Z$ projections in each octant. These track patterns, called roads, represent hit patterns left in the MI, MM and MO chambers (in case of P-chambers) by a muon originating in the interaction point. A second set of PLUs is performing a search in the Z-chambers.

The roads, parametrized by the cell number and half width of the road at each layer (resulting in 6 parameters for tracks in the P-chambers, 8 in the Z-chambers) were predetermined using the GEANT simulation package, for muons of both charges with a momentum above 2 GeV, and are stored in modules called ECLine Drivers. Each PLU has access to the data of three octants, since muon tracks bent in the magnetic field can cross two octants.

The barrel muon trigger consists of three subtriggers: dimuon trigger, small angle dimuon trigger and single muon trigger. The PLUs also check for coincidence condition, which is

Figure 2.10: Muon trigger data readout chain. The encoders (ENC) count the number of hits in a group of four inputs. Two stage adder unit can be configured by software according to the number of encoders needed for the complete cell - this setup is stored in the Cell Size Memory. The Cell Size and Reformat memories are not shown in this picture.

different for the three subtriggers:

    i. **Dimuon trigger** requires for each of the muons 2 out of 3 layers in the P-chambers to be hit within a road. No requirement is put on the Z-chambers.

    ii. **Small Angle Dimuon trigger** requires at least a hit in the MI chamber. On the Z part, at least one hit in the II or IM chambers are needed.

    iii. **Single Muon trigger** requires 2 out of 3 hits in the P-chambers. Hits in 3 out of 4 layers are required in the Z-chambers.

Results from the PLUs are stored in registers, to which Memory Lookup Units have access, in order to take the final decision. For the dimuon trigger, two P tracks fullfilling the above criteria are required in any two octants, except adjacent ones. The single muon trigger requires a P and a Z component in the same octant. The small angle muon trigger is the most stringent one, since it is the most exposed to backgrounds. The coincidence of a P and Z component in the forward and in the backward direction is required separately. The muon tracks must match back-to-back in ϕ, plus-minus one octant.

The final first level barrel muon trigger decision is a logical OR of the three subtriggers.

The different subtriggers cover different polar angle regions: the single muon trigger covers $45° < \theta < 135°$, the dimuon trigger $35° < \theta < 145°$, and the small angle dimuon trigger acceptance region is between $24° < \theta < 45°$ and $135° < \theta < 156°$.

The level 1 muon trigger rate is about 10Hz, dominated by cosmic muons. To further reduce this backgrond, coincidence with at least one scintillator hit within a time window of ±30 ns around the beam crossing is required, not regarding the position of the scintillator hit. This reduces the trigger rate to ~ 1 Hz.

Forward/Backward Muon Trigger

The amplified and discriminated signals from the forward/backward muon chambers are first passed to an 8:1 multiplexer (DIMUX) which performs also address encoding. The timing signals are sent via detector communication cards (DETCOM) to TDCs for time encoding, while the cell address information is sent to Forward/Backward Read-Out Controller (FBROC) modules. The schematics of the forward/backward muon chambers readout is shown in Fig. 2.11. The FBROC [30] module collects and stores the address data of hit cells. It counts the number of hits in every chamber, and sends a 1 or a 0 signal to the forward/backward muon trigger for every chamber in each layer (FI, FM, FO), depending on whether the number of hits is above threshold or not. The forward/backward chamber trigger is fired if there are at least two chambers hit in the same half octant, with a hit in the inner chamber (FI) being required.

The data from the resistive plate chambers is first processed in a track finder unit. A search is performed for coincidences in a 96 × 96 matrix for elements defining particles coming from the interaction point. The pattern for such elements has been defined by a Monte Carlo simulation, and depends on the polar production angle and momentum of the particle, magnetic deflection and multiple scattering in the magnet door. If a coincidence has been found in the preprogrammed pattern, a signal is sent to the forward/backward muon trigger module, indicating the half door traversed by the muon.

The forward/backward muon trigger receives also various intermediate results from the barrel muon trigger [33]:

- the P component of the single and dimuon barrel trigger in each octant;

21
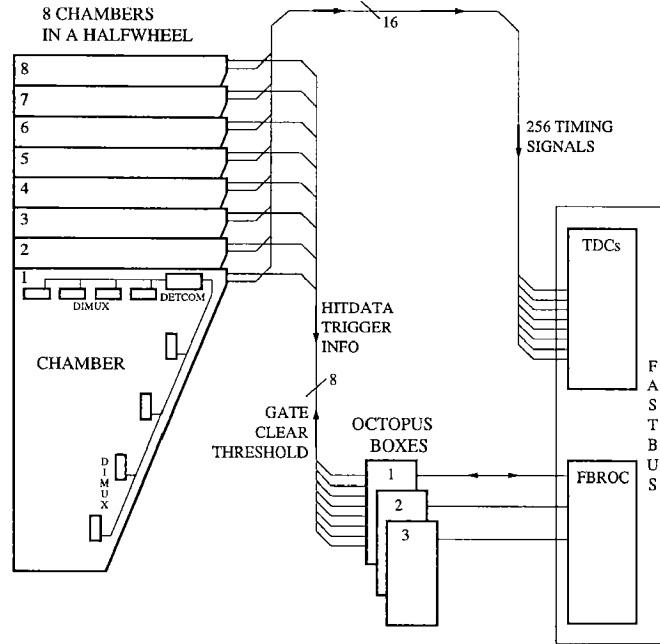
Figure 2.11:

- the sixteen small angle dimuon trigger decisions;

- a logical OR of the MI , and the logical OR of the MM trigger cells in each octant ;

- a logical OR of the II and IM trigger cells in each octant, separately for both sides.

All the above data, together with the data from barrel and endcap scintillators is used in the forward/backward muon trigger. There are four single muon and five dimuon subtriggers. The conditions to fire a particular subtrigger are listed in Tables 2.1 and 2.2. Although the basic combinations are hard wired, all the subtriggers can be enabled/disabled by software. A parameter file is downloaded to the forward/backward muon trigger during initialization at the beginning of each fill. Also, some conditions can be tightened or released depending on background conditions. The SMB single muon trigger has an optional requirement of hits in the MI and/or MM chamber in the same octant. For all the dimuon triggers, a maximum collinearity requirement is set separately. For the high energy runs, the collinearity was set to ±4 octants, which represents the maximum in L3. Dimuon triggers DMA, DMC and DME can trigger on muons on the same side of the detector.

Contrary to the barrel muon trigger, the forward/backward muon trigger rate is highly dependent on the beam energy and luminosity. A typical rate is of the order of 1 − 2.5Hz. The forward/backward trigger is also very sensitive to beam conditions, since many components like the endcap scintillators and the RPCs are exposed to synchrotron radiation.

The forward/backward muon trigger is implemented in just six home made CAMAC modules, each one containing a processor, with the predefined subtrigger conditions and patterns stored in EPROMS. Compared with the more than 100 modules needed for the barrel muon trigger, the forward/backward trigger presents a very elegant solution. Even if redefining the

subtrigger	condition	acceptance region
SMA	RPC & f/b chamber	$24° - 34°$
SMB	barrel scint. & f/b chamber (& MI and/or MM) (& II and/or IM)	$34° - 45°$
SMC	RPC & endcap scint.	$24° - 34°$
SMD	endcap scint. & f/b chamber	$24° - 34°$

Table 2.1: The level 1 forward/backward single muon trigger conditions. '&' means a coincidence in the same octant.

subtrigger	condition
DMA	RPC × RPC
DMB	RPC × barrel P track
DMC	endcap scint. × small angle barrel muon
DMD	endcap scint. & f/b chamber × RPC
DME	endcap scint. & f/b chamber × endcap scint. & f/b chamber

Table 2.2: The level 1 forward/backward dimuon trigger conditions. '&' means a coincidence in the same octant, while 'A × B' denotes condition A for first and condition B for the second muon.

basic trigger classes would mean that one needs to reburn the EPROMS, it is much more efficient than rebuilding a trigger using standard available CAMAC modules.

Muon Trigger Monitoring System

The online monitoring of the barrel muon trigger was implemented since the beginning of L3 data taking as a task running on the main VAX computer. A simulation program was evaluating the trigger data part of a complete event received from the central event builder 2.3.3, and compared its own decision with the decision actually taken by the level 1 trigger. In this manner about 10% of the events could be cross checked. The output of the simulation appeared on a terminal display in the L3 control room, visible to the person on shift.

This solution proved unsatisfactory after the upgrade of L3, in particular the simulation of the forward/backward muon trigger would have required too much CPU time of the online machines needed for data taking. It was therefore decided to move the forward/backward muon trigger simulation which was written for offline monitoring [34], as well as the existing barrel trigger monitor program, to a machine dedicated mainly to interactive online activities, and not critical from the time consumption point of view.

The current monitoring task is acting as a TCP/IP client running on an Alpha VAX. A server process [35], still running on the main VAX, delivers complete events from the central event builder. The second new feature, apart of the online monitoring of the forward/backward trigger behaviour, is the interface to the Central Error Analyzer [36]. The trigger data is analyzed, compared to the decisions of the triggers, and if necessary, a message is sent to the CEA. Central Error Analyzer instructs the shift personnel about eventual malfunctioning and a possible solution by popping up a message window on his terminal, and/or sends a notification message via GSM to the expert on call. The CEA is also logging all received messages, which can be evaluated at a later time by the expert. Correlations between different error messages

from a single device to be monitored, as well as from different subdetector components, can be evaluated in order to pinpoint a specific problem. This correlations can be stored in CEAs data base, and will be used for faster problem solution, should the same or similar problem occur again at a later time.

This complete system has shown very good performance, with very short reaction time on error conditions, and resulted in basically no beam time loss due to muon trigger problems in 1999.

Energy Trigger

The energy trigger [37] selects events with energy deposits in the electromagnetic and hadron calorimeters. For trigger purposes, the electromagnetic calorimeter is divided in 512 blocks, with 32×16 elements in the $\phi - \theta$ plane. The hadronic calorimeter is divided in two layers: first layer is made of 176 blocks with a segmentation of 16×11 in $\phi - \theta$, while the second layer consists of 208 blocks (16×13). Each luminosity monitor delivers 16 signals corresponding to segmentation in ϕ. This results in 928 analog sum signals which are digitized and converted into energy deposits.

The energy trigger is a logical OR of the following conditions:

- *Total Energy:* The sum of the energy deposits in all calorimeters is above a certain threshold. There are four different trigger thresholds based on the values of

  i. total energy in all calorimeters must be above 20 GeV,

  ii. total energy in the electromagnetic calorimeter (barrel and end cap) must be above 20 GeV,

  iii. total energy in the barrel electromagnetic and hadron calorimeter must be above 15 GeV

  iv. total energy in the barrel electromagnetic calorimeter must be above 10 GeV

- *Cluster Trigger:* A cluster is defined as a localized energy deposit in different detector layers at same θ and ϕ coordinates. A threshold on the energy of at least 7 GeV in one such cluster defines this trigger condition. If a TEC track was found by the TEC trigger at the same coordinates, the threshold is lowered to 3 GeV.

- *Hit Counting Trigger:* At least two trigger cells have recorded energy above 5 GeV.

- *Single Photon Trigger:* 80% of the energy recorded in the electromagnetc calorimeter must be confined to a single cluster.

- *Luminosity Trigger:* Bhabha events in the luminosity monitor are triggered in one of two ways: the 'luminosity' trigger requires back-to-back segments with an energy above a threshold of 15 GeV on each side. For the 'double-tag' trigger it is required that the total energy in the calorimeters be more than 25 GeV for the larger measured energy and 5 GeV for the smaller, irrespective of their angular correlation.

Fast Encoding and Readout ADCs (FERA) are used to digitize the analog sum signals from the calorimeters.

2.3.2 Second Level Trigger

The second level trigger receives trigger data during level 1 processing time. Upon reception of positive first level triger decision (ACCEPT), it starts processing the data to make its own decision. At the same time, it is ready to receive data of the next event, which is then stored at the next position in the buffer. In the opposite case (CLEAR reception), the current buffer is reused for the next event.

Three filter algorithms are implemented at the second level [38]: energy, muon and TEC algorithm.

- **Energy algorithm:** BGO trigger elements are formed by grouping of 30 crystals. In the hadron calorimeter, towers located on a ring are added up to form two layers with a ϕ segmentation of 16 trigger elements. Several classes of second level energy trigger are considered: electromagnetic (single) cluster, electromagnetic at large angle, electromagnetic at small and large angles, electromagnetic and hadronic jet components, hadronic jet components, total energy at large angle and total energy at large and small angles - each of them has a predefined energy threshold.

- **Muon algorithm:** In addition to a time correlation with a scintillator hit performed at first level, the second level trigger demands also that the scintillator hit corresponds in space with the muon track, i.e. is in the same octant. In addition, events with less than 7 hits in the central tracker are also rejected.

- **TEC algorithm:** Constructed to reject beam-gas and beam-wall interactions, which are characterized by many hits in the central tracker, the TEC algorithm analyzes events with high multiplicity in the TEC. Drift time measurement is used to reconstruct the tracks in the $R - \phi$ plane and its distance of closest approach (DCA) to the interaction point. Events with at least one track with the DCA of less than 10mm are accepted.

With an efficiency of 99.99% for e^+e^- events, the rejection rate of the second level trigger is of the order of 60%.

The whole level 2 trigger is implemented in transputer technology, consisting of 29 T9000 transputers interconnected via two C104 dynamic routers from SGS-Thomson [39]. The system is able to receive data into its memory at 45kHz, with an output rate of 30Hz and no deadtime introduced into the DAQ system.

2.3.3 Event Builder

Upon reception of positive level 1 trigger decision, subdetectors start readout and digitization of data, which is first assembled in four parallel Subdetector Event Builder (SEB) units. The maximum deadtime introduced in the system is $500\mu s$ arizing from the readout of the hadron calorimeter. This is also the maximum deadtime in the whole DAQ system. Data from SEBs are stored in four dual port memories, which are read out by the Central Event Builder (CEB), if the event was accepted by the level 2 trigger. The central event builder combines data from all subdetectors and trigger data as received from the second level trigger. For this purpose, the event number distributed by the trigger control logic, as described in Sec. 2.3.1, is used. The CEB then sends the complete event to the third level trigger for final decision.

2.3.4   Third Level Trigger

The third level trigger is the first stage in the L3 DAQ chain to analyze the complete event with the same granularity as offline analysis. It is built as a farm of two Alpha VAX machines. The Central Event Builder dispatches the events accepted by the level 2 trigger to a free Alpha through the SCSI bus.

Each Alpha machine is running three tasks: The *SCSI handler* receives events from the CEB, and writes them in a first (input) global memory. The *level 3 filter* task reads from this memory, analyses the event, and writes the accepted events to a second (output) global memory. Finally, the *data sender* reads the second global memory contents, and sends them via FDDI to the main VAX computer for storage.

Just as the level 2 trigger, the level 3 filter consists of three algorithms: energy, muon and TEC algorithm.

- **The energy algorithm** first looks for clusters in the calorimeters. As the granularity is much finer than at the earlier trigger levels, the thresholds can be set at lower values. The event is accepted if the highest BGO cluster energy is above 1 GeV, or the total energy in the BGO is above 3 GeV, or if the sum of cluster energies in the BGO and HCAL is above 10 GeV. The region between $18° < \theta < 162°$ is taken into account for the measurement of the above quantities. In the BGO barrel region, the threshold is lowered to 0.6 GeV to accept single photon events.

  Calorimetric clusters are then grouped into 'mini-jets' by combining clusters in the same θ and ϕ region, and a threshold of 5 GeV is applied. If two minijets are found in the opposite hemisphere, the threshold is lowered to 3 GeV.

- **The muon algorithm** performs a pattern recognition in the $R - \phi$ plane of the muon chambers. A more stringent cut of ± 10 ns is applied on the time of the scintillator hit matching the muon track. For tracks found in the forward/backward region, a spatial coincidence with at least one RPC hit is required within a window of ± 50 ns around the beam crossing. The event is accepted, if at least one track-scintillator or track-RPC coincidence is found. In addition, a search for Minimum Ionizing Particle signature is performed in the hadron calorimeter. The event is accepted, if at least one muon track is found in the HCAL.

  Events with a high hit multiplicity in the TEC are analyzed according the two algorithms mentioned above. Otherwise,

- **the TEC algorithm** looks for ϕ angular correlations between TEC tracks and *i)* BGO clusters with more than 150 MeV energy, *ii)* HCAL clusters with more than 500 MeV, and *iii)* scintillator hits. The event is accepted, if at least one track matches at least two of the elements *i) - iii)*, or if it matches a BGO cluster with more than 2 GeV energy.

  In order to trigger on two photon physics events, which are characterized by few low energy particles that can be only detected in the BGO, a cut on the quality of the reconstructed vertex is applied, using the DCA of the tracks with respect to the vertex. If the event passes the vertex cut, tracks are matched in ϕ with BGO clusters: for only one match, the BGO bump is required to have at least 200 MeV energy, for 2 or more, 50 MeV is enough to accept the event.

The average processing time at level 3 is of the order of 100 ms/event, with a rejection rate of $\sim 30 - 50\%$, and a measured efficiency of 100%.

2.4 Real Detector Simulation

Monte Carlo generated events pass two steps of detector simulation: in the first step, the passage of the particles is simulated according to the detector material they pass. For this purpose, a precise description of the L3 detector using GEANT package is used. This results in the so called 'ideal detector' simulation. In addition, time dependent effects are taken into account, which results in most realistic description of the detector response.

During a run, the status of all subdetectors is monitored and stored in a database. Tripping HV units in the TEC or muon chambers, BGO crystals becoming 'hot' or dying during the running period, dead channels and wafer inefficiencies in the SMD, dead towers in the HCAL, noise conditions in all subdetectors as well as changing trigger conditions are monitored in this way.

After the running period is finished, the existing 'ideal detector' Monte Carlo event samples are mapped run by run onto the run conditions which existed during data taking. In addition to the online information stored in the corresponding database, offline quantities are also used: calibration parameters for all subdetectors and beam spot position calculated after data taking. The real detector simulated event samples have the same run numbers assigned as the data to which they are mapped.

2.5 Particle Signatures in L3

In every analysis, a crucial point is the proper identification of the particles seen in the detector. The modular structure of L3 is exploited for this purpose, with the combinations of signals in different subdetectors serving as particle signatures. The principle of particle identification in L3 is shown in Fig. 2.12.
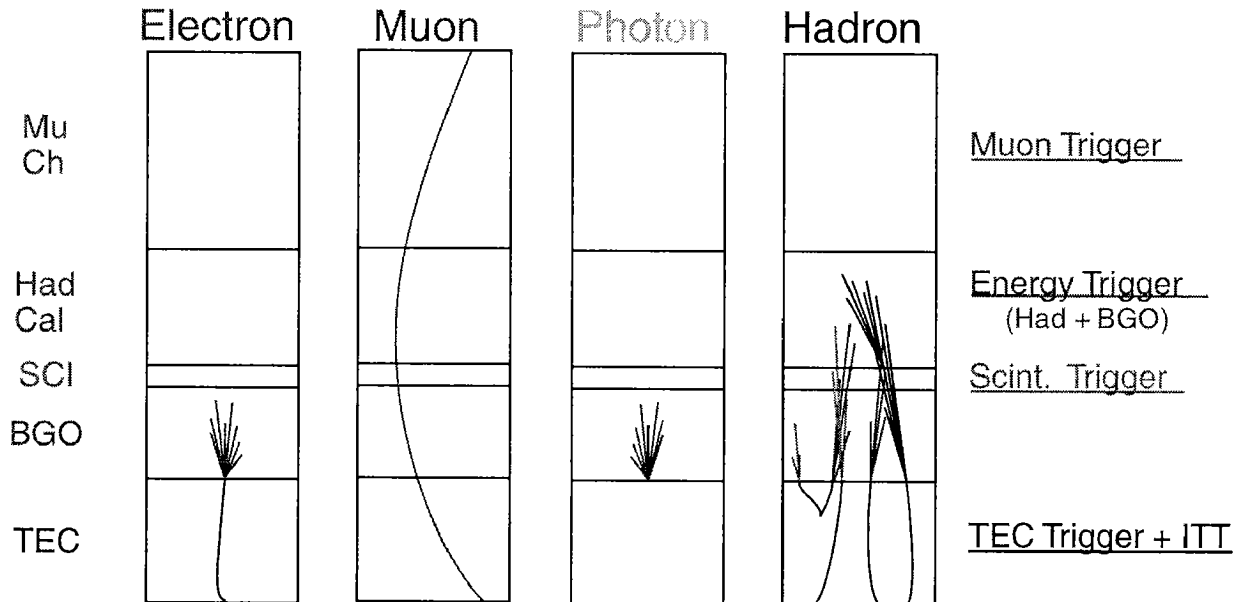
Figure 2.12: Particle signatures as seen in the L3 subdetectors.

Photon

The only signature of the photon in L3 is it's energy deposit in the electromagnetic calorimeter. Carrying no charge, the photon traverses the TEC without leaving a track, thus one requires no track matching the BGO bump. In order to distinguish photons from low energy neutral hadrons decaying into multi-photon states, the energy deposit in the ECAL is examined. The ratio of energy in a matrix of 3×3 and 5×5 crystals (E_9/E_{25}) around the most energetic one is evaluated. Electrons and photons deposit their energy in a narrow shower, therefore E_9/E_{25} is close to 1.0 for these particles, and enables discrimination from multi-photon states originating in π^0 decay. A neural network based approach using shower shape variables has also been developped [40].

Electron

Electron candidates are recognized by an energy deposit in the ECAL, together with a matching TEC track within a narrow cone with tip in the interaction point. Electrons are distinguished from charged hadrons by the energy deposit shape, by requiring a high value of the E_9/E_{25} variable described in the paragraph above. Very energetic electrons can have a small amount of energy in the HCAL, due to avalanche electrons leaking out of the BGO crystals.

Muon

A muon with at least 2.5 GeV momentum traversing the L3 detector passes usually all subdetectors. It is identified by a reconstructed track in the muon spectrometer. It leaves an energy deposit in the electromagnetic calorimeter of $\sim$ 0.5 GeV, and about 2 GeV in the hadron calorimeter. In addition, usually a TEC track can be matched to the muon track, resulting in a better measurement of the azimutal angle and the DCA to the interaction point.

Muons traversing the calorimeters but passing through the gaps in the muon spectrometer can be found by looking for energy deposits in ECAL and HCAL matching a TEC track, as described in App. A.

Jets and Hadrons

Hadrons are detected in L3 due to their energy deposits in the electromagnetic and hadron calorimeters. In addition, charged hadrons leave a track in the TEC and produce hits in the scintillators. The 8 absorption legths of the hadron calorimeter result in the hadrons being stopped in the calorimeter to a high extent, and the few 'punchthrough' hadrons are easily recognized in the muon detector due to their high hit multiplicity.

Quark and gluon jets are identified by high multiplicity in the central tracker, together with a high number of energy clusters in the calorimeters at the same angular position.

Tau jets are recognized by their low decay multiplicity and very narrow jet opening angle.

Chapter 3

The $e^+e^- \rightarrow WW \rightarrow \bar{f}f\bar{f}f$ process

At tree level in the Standard Model, there are three diagrams contributing to W-pair production, the electron-positron annihilation into a virtual γ or a Z, which then couples to a W^+W^- pair, and the double conversion diagram with t-channel neutrino exchange. These diagrams, denoted CC03, are shown in Fig. 3.1. Each of the W bosons decays into a pair of quark and antiquark,
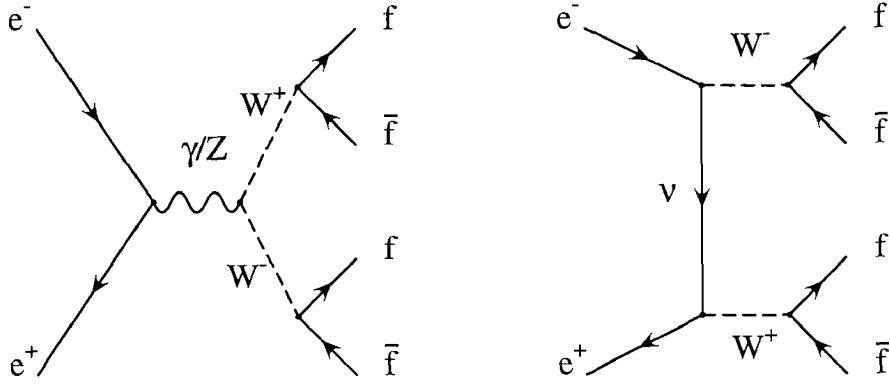
Figure 3.1: Tree level diagrams contributing to W pair production.

e.g. $W^+ \rightarrow u\bar{d}$ or $c\bar{s}$, or a lepton-neutrino pair, e.g. $W^+ \rightarrow l^+\nu$. The W-pair production process is thus a subset of the general four fermion final state processes. Other diagrams contributing to a particular final state may contain only one or no W bosons at all. An example of a non-WW diagram contributing to the $qq\mu\nu$ final state is shown in Fig. 3.2. While a complete classification of four fermion production processes is given in Ref. [42], Table 3 shows the number of diagrams contributing the W pair mediated final states. In particular, for final states with

	du	$\bar{s}c$	$\bar{e}\nu_e$	$\bar{\mu}\nu_\mu$	$\bar{\tau}\nu_\tau$
$d\bar{u}$	43	11	20	10	10
$e\bar{\nu}_e$	20	20	56	18	18
$\mu\bar{\nu}_\mu$	10	10	18	18	9

Table 3.1: Number of Feynman diagrams for W-pair produced four fermion final states.

electrons or electron-neutrinos, additional singly resonant diagrams must be taken into account.

In final states with particle-antiparticle pairs, there are also contributions from Z-pair mediated processes, and QCD diagrams with intermediate gluons contribute to the final states with two quark-antiquark pairs.
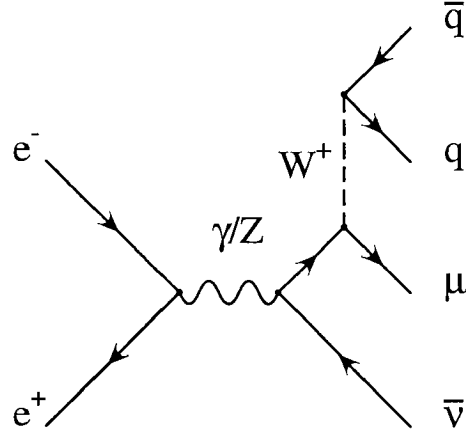
Figure 3.2: Example of a singly resonant diagram contributing to the qq$\mu\nu$ final state.

The leptonically decaying W will result in a visible lepton in the detector in the case of $e^{\pm}$ and $\mu^{\pm}$ or $\tau^{\pm}$ decaying into lepton and neutinos, or a narrow low multiplicity hadronic jet, if the τ should decay hadronically.

If the W decays into a quark-antiquark pair, the process is described by perturbative QCD. In a first stage, showers of coloured partons are produced, which then fragment into colourless hadrons. In a last stage, unstable hadrons decay into particles which are finally detected in the experimental device. Two jets (neglecting the possible hard gluon radiation) are the visible signature of a hadronically decaying W.

Apart from the fragmentation being a field of intensive study within the framework of QCD, where many phenomenological models are tested by comparison with data, the difficulties in this process arise from interconnection effects. In particular, in the case where both Ws decay hadronically, gluon exchange between quarks from different Ws can lead to distortions in jet shapes as well as particle multiplicities, and therefore influence the W mass measurement. Further, the production probability of identical bosons close in phase space can be enhanced by Bose-Einstein effects.

Chapter 4

Event Selection

The selection procedure will be described in this chapter, with emphasis given to the $qq\mu\nu$ channel. It is based on a set of event parameters which are either characteristic for the signal process, or which take different values for signal and background processes, and can therefore be used to reject the latter.

Since the only difference between muons detected in the muon chambers and through their signature as MIP is the resolution in the momentum measurement, the same set of cuts is applied with different cut values where necessary.

The considered centre-of-mass energies for which the analysis was performed are sufficiently far away from the threshold energy for W-pair production. The signal event characteristics at these energies are very similar, thus the same set of cuts, optimized at both energies, has been used. The results and efficiencies will be reported in Sec. 5.2 and 5.3.

4.1 WW $\rightarrow$ qq$\mu\nu$

This decay channel is characterized by two jets resulting from the hadronization of the two quarks, a high energy muon and missing energy carried away by the undetected neutrino. A typical $qq\mu\nu$ event in the L3 detector is shown in Fig. 4.1. Main non-WW background processes are the hadronic Z decays, $e^+e^- \rightarrow \gamma\gamma \rightarrow e^+e^- +$ hadrons with muons from heavy hadron decay, and the neutral current $e^+e^- \rightarrow ZZ \rightarrow qq\mu^+\mu^-$ process. The Standard Model expectation of the signal cross section, as well as the cross section of the above background processes is summarized in Table 4.1. Cosmic events with highly energetic muons traversing the detector and leaving energy deposits in the calorimeters could also mimic signal signature. Main background to the $qq\mu\nu$ channel coming from the WW process itself is the $qq\tau\nu$ channel with the τ decaying in $\mu\nu\nu$.

To discriminate the signal from these various backgrounds, a cut based analysis was applied which will be described in detail below. The efficiencies and accepted non WW background at the energies of $\sqrt{s} = 183$ and 189 GeV will be presented in Sec. 5.2 and Sec. 5.3, respectively.

4.1.1 Particle Identification

The muon is identified as either a track in the muon detector (MUTK) or by its minimum ionizing particle (MIP) signature in the calorimeters. In the first case, at least two layers must be hit in order to make a momentum measurement possible, as described in Sec. 2.2.6. Some of the muons are passing through gaps in the muon detector or dead cells. These muons will not
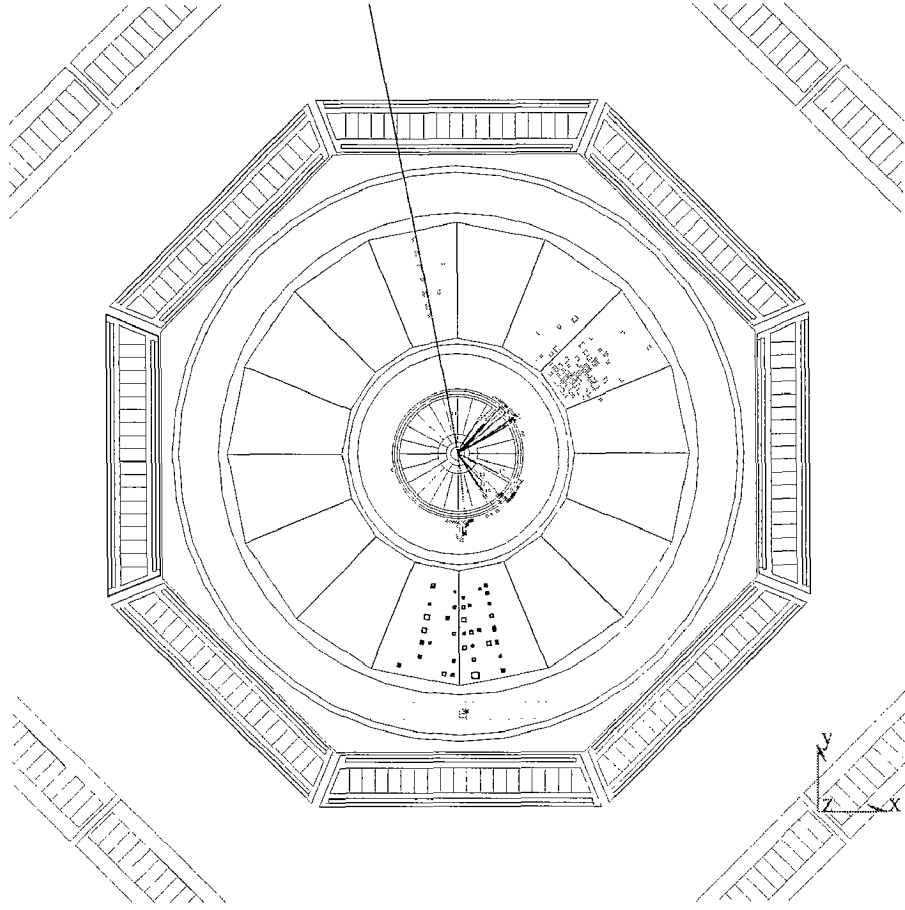
Figure 4.1: A selected $qq\mu\nu$ candidate event at $\sqrt{s} = 189$ GeV shown in $R - \phi$ view. From the centre outwards: tracks in the central tracker; small energy deposits in the electromagnetic calorimeter, energy clusters in the hadron calorimeter and a muon track going upwards, with the complete first layer and parts of the second layer of muon chambers shown. The size of the calorimetric clusters corresponds to the size of the energy deposit. Shown is also one plate of the muon filter, located between the hadron calorimeter and the muon spectrometer. One can clearly distinguish two hadronic jets and the muon. The event is not balanced in the transverse plane, indicating missing momentum.

Process	σ at $\sqrt{s} = 183$ GeV [pb]	σ at $\sqrt{s} = 189$ GeV [pb]
$e^+e^- \to WW \to f\bar{f}f\bar{f}$	15.5	16.6
$e^+e^- \to Z/\gamma \to q\bar{q}$	107.8	98.4
$e^+e^- \to ZZ \to ffff$	0.59	0.97
$e^+e^- \to e^+e^- + \text{hadrons}$	15360	15580

Table 4.1: Standard model cross sections of the signal and main background processes at $\sqrt{s} = 183$ and 189 GeV.

be detected by the muon spectrometer, but can be recovered by looking for energy deposits in the calorimeters which match values one would expect from a minimum ionizing particle. Such an algorithm was implemented in the L3 reconstruction software, and is described in detail in App. A.

After a muon has been identified, its constituents - notably the associated track as well as calorimetric clusters - are removed, and the event is forced to cluster into two jets. In the selection presented here, the DURHAM algorithm [43] was used for jet clustering. The resulting θ-angular resolution is 27.4 mrad in 59% of the cases, with a ϕ resolution of 30.6 mrad with 53% probability. The resolution plots are shown in Fig. 4.2, with a fitted double gaussian. The long tails of the distributions are due to particles hitting gaps between the calorimeter modules, dead or hot crystals, and also from the worse energy and angular resolution of the EGAP detector. Fig. 4.3 shows the jet energy resolution plot, with an average energy resolution of 11.1% for 72% of jets.
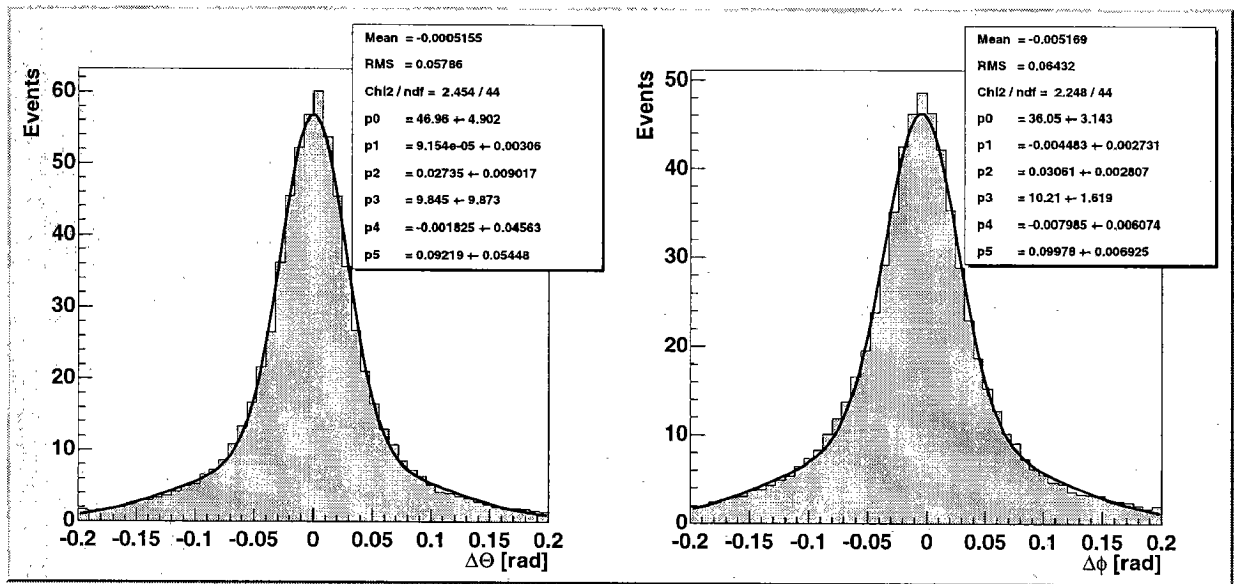
Figure 4.2: Angle between reconstructed jet and generated particle direction in a sample of simulated WW $\rightarrow$ qq$\mu\nu$ events at $\sqrt{s} = 189$ GeV. The histograms are normalized to $L = 200$ pb^{-1}.

4.1.2   Preselection

In order to shorten the processing time, some preselection cuts have been applied on the data and simulated events. First of all, a muon must be present in the qq$\mu\nu$ final state. Events with a highest energy muon of less than 5 GeV are rejected at preselection stage, in accordance with the muon energy distribution in this channel as shown in Fig. 4.6. The hadronic system of the qq$\mu\nu$ final state offers a good criterion for a preselection, namely the requirement of activity in the inner detector. At this stage, a minimum of 5 tracks in the TEC with DCA of less than 10 mm, as well as at least 10 calorimetric clusters with minimum energy of 100MeV in the calorimeters are required. These cuts are only used for faster processing time, since, as can be seen in the distributions shown in Fig. 5.2 and 5.10, they do not contribute to the selection purity when the other cuts are applied. Nevertheless, many noise and cosmic events can be
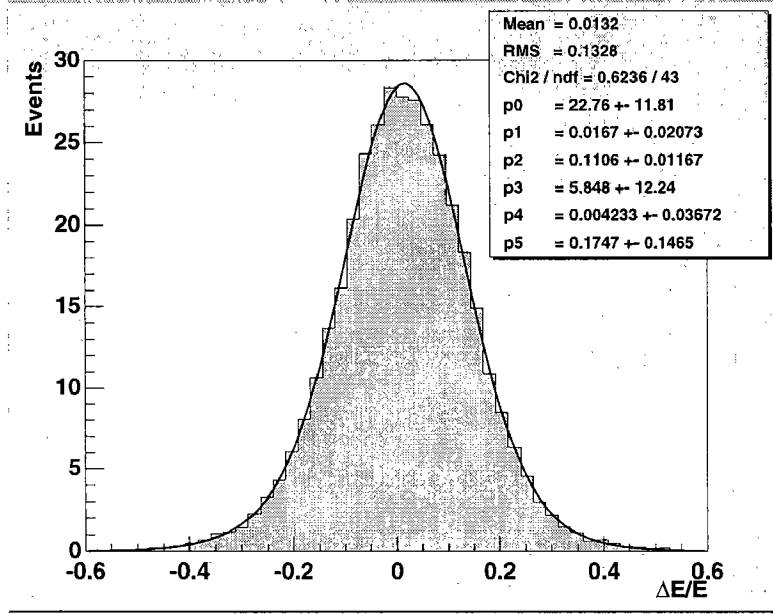
Figure 4.3: Difference between reconstructed and generated jet energy in a sample of simulated WW $\rightarrow$ qq$\mu\nu$ events at $\sqrt{s} = 189$ GeV. The histogram is normalized to $L = 200$ pb^{-1}.

rejected at an early stage of the selection. The behaviour of the detector and the accuracy of the simulation of detector response can be easily monitored in this way.

4.1.3 Selection Cuts

After the identification of the decay products of the two W bosons, the signal events need to be discriminated against background contributions.

Kinematic qq$\mu\nu$ Event Properties

Assuming that the two jets are products of hadronization of two quarks from the decay of one W boson, the mass of the hadronic system has to be consistent with the W mass. The same is true for the mass of the muon-neutrino system, where the momentum of the neutrino is calculated as the missing momentum vector:

$$\vec{p}_\nu = -(\vec{p}_\mu + \vec{p}_{jet1} + \vec{p}_{jet2}). \tag{4.1}$$

Fig. 4.4 shows the distributions of the reconstructed masses of the $\mu\nu$ and the hadronic systems. The gaussian distribution of the latter in the signal sample reflects the angular and energy resolution of the electromagnetic and hadron calorimeters. The mass of the $\mu\nu$ system depends on the resolution obtained in the muon spectrometer, and thus the different resolutions for triplets and doublets (c.f Sec. 2.2.6) results in a double gaussian distribution of the reconstructed mass. The $\mu\nu$ system mass for Z/γ tends to group at very low values, while the mass of the hadronic system is distributed at high values. The enhancement of events at $\sim$ 30 GeV in the $\mu\nu$ mass and at $\sim$ 70 GeV in the mass of the jets system comes from events with missing energy along the beam direction. This enhancement can be significantly reduced by rejecting events in which the direction of missing momentum points in the beam direction, as will be

discussed further below. Due to the peaking structure for the signal events, a window around the expected mass of the W boson can be set, and only events falling inside these regions are selected.
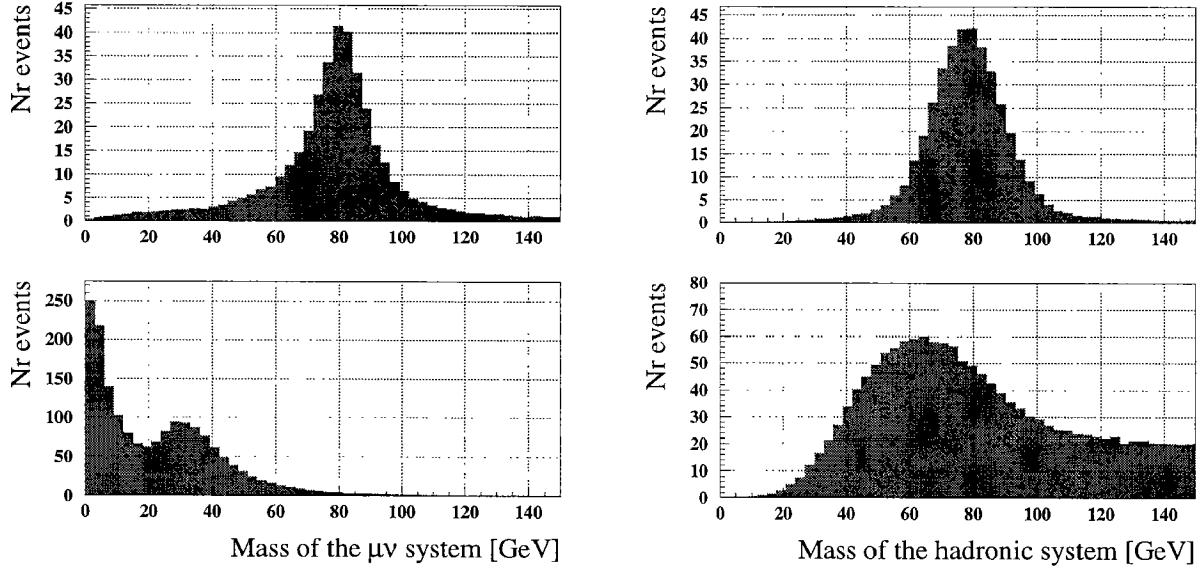
Figure 4.4: Reconstructed mass distributions of the muon-neutrino (left) and the hadronic system (right) in simulated WW $\rightarrow$ qq$\mu\nu$ events (top), and Z/γ events (bottom). Both samples were generated at $\sqrt{s} = 189$ GeV. Plots are normalized to an integrated luminosity of 200 pb^{-1}.

For the measurement of the W mass, the cuts should not be set too close to the expected W mass, in order not to bias the mass measurement.

Cosmic Radiation Rejection

Muons created in the atmosphere by cosmic radiation usually pass through the detector leaving a track in the muon detector and, if they pass close enough to the beam pipe, also in the central tracker. They leave an energy deposit in the calorimeters consistent with the MIP signature, c.f. App. A. In order to reject events with a cosmic muon, the distance of closest approach (DCA) of the muon track to the interaction point is required to be less than 80 mm in $R - \phi$, and less than 120 mm in Z (ZDCA). The distributions of these two variables for the signal events are shown in Fig. 4.5. The muons in signal events are generated at the interaction point, the non zero width of the distributions reflects the resolution of the muon chambers. To obtain the DCA and ZDCA of a muon, the position and angle measurement performed in the spectrometer needs to be extrapolated to the interaction point position using the measured momentum. Cosmic muons, on contrary, are not constrained to the beam spot position. A relatively loose cut on the DCA and ZDCA values reject most cosmic events.

Rejection of $e^+e^- \rightarrow Z/\gamma \rightarrow q\bar{q}$

This is the most significant non WW background for this analysis. The muons appearing in the final state of this process originate in the decay of a heavy quark. They have typically a low momentum and low momentum component transverse to the jet they originate from. The
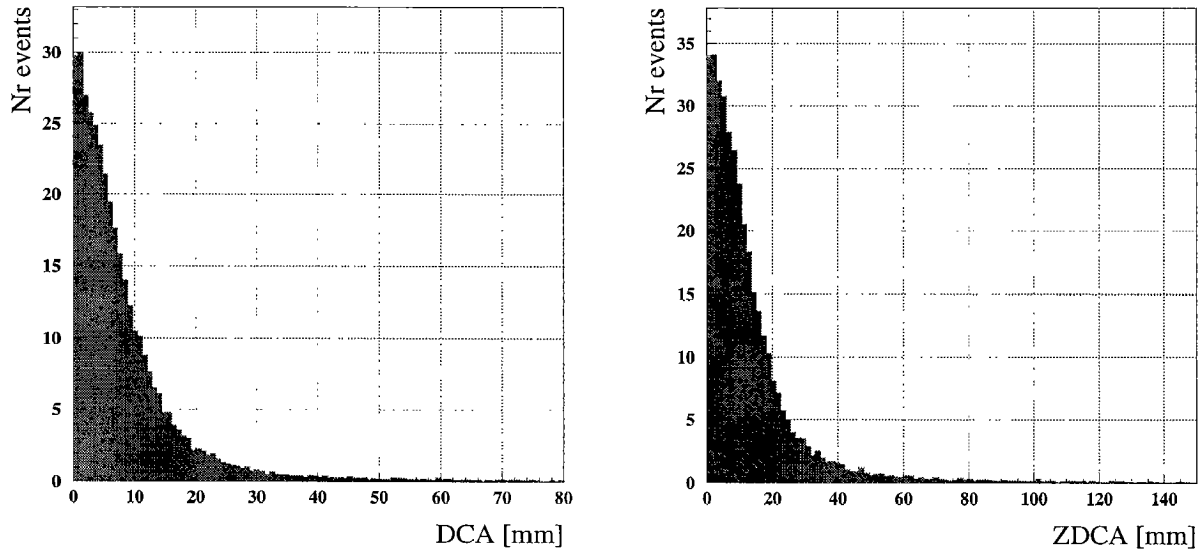
Figure 4.5: DCA and ZDCA parameters of the muon in simulated WW → qqμν events. Both samples were generated at $\sqrt{s} = 189$ GeV. Plots are normalized to an integrated luminosity of 200 pb^{-1}.

kinematics of WW signal events predict muon energy in a band between ∼ 25 − 65 GeV. The cuts imposed to reject events from this channel are therefore a minimum muon momentum and minimum angle of the muon to the next hadronic jet. The distributions of these variables are shown in Fig. 4.6 for the WW → qqμν and for Z/γ → q̄q events. As can be seen in these plots, the above cuts provide a very good separation of signal and background events.

Rejection of $e^+e^- \rightarrow ZZ \rightarrow f\bar{f}f\bar{f}$

Pair production of Z bosons results in a four fermion final state. Of particular interest here is the $q\bar{q}\mu^+\mu^-$ final state. Since a secondary muon can also appear from the decay in the hadronic system of a W-pair event, a simple requirement of having only one muon in the signature would significantly decrease the signal selection efficiency. The main difference used for discrimination is the very low missing energy in the final state mediated by Z-pair production. A minimum cut on the mass of the muon-neutrino system rejects the bulk of this background, as can be seen in Fig. 4.7. To further reduce the accepted ZZ background, an additional cut on the momentum of the second most energetic muon has been introduced. The distributions of the momentum of the second most energetic muon in the event for signal and ZZ background are also shown in Fig. 4.7. If a second muon is present in a WW → qqμν event, it's energy tends to be rather low, as expected from a muon in a hadron decay. The enhancement in events at ∼ 45 GeV in the ZZ distribution comes from ZZ → $q\bar{q}\mu^+\mu^-$ events, while the ZZ → $q\bar{q}\nu\nu$ with hadrons decaying into muons results in the peak at low energy. In the latter case, also the highest energy muon has a low momentum and these events are rejected by applying a cut on the energy of the primary muon, as described above.

Since the cross section of the ZZ process is one order of magnitude lower than the WW cross section, as can be seen in Tab. 4.1, the cross section measurement is not much affected by a possible ZZ contribution. The peaking structure in the mass distribution of the ZZ events
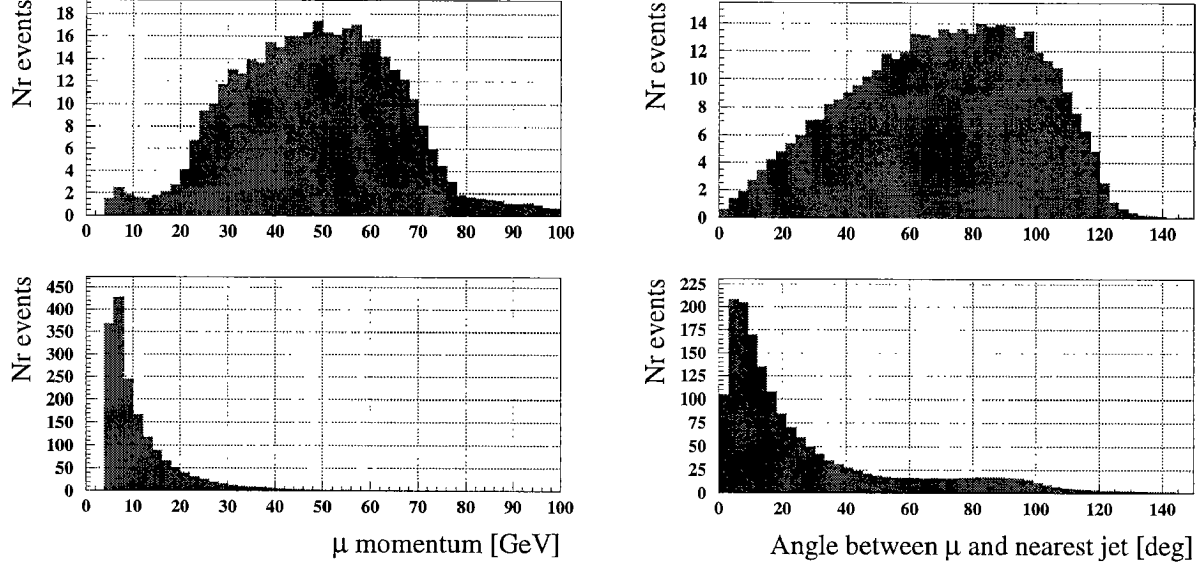
Figure 4.6: Reconstructed muon momentum (left) and angle between muon and the nearest jet (right) in the WW → qqμν decay (top), and for muons appearing in hadronic Z decays (bottom). All plots show events simulated at $\sqrt{s}$ = 189 GeV, after full detector simulation, and are normalized to an integrated luminosity of 200 pb^{-1}.
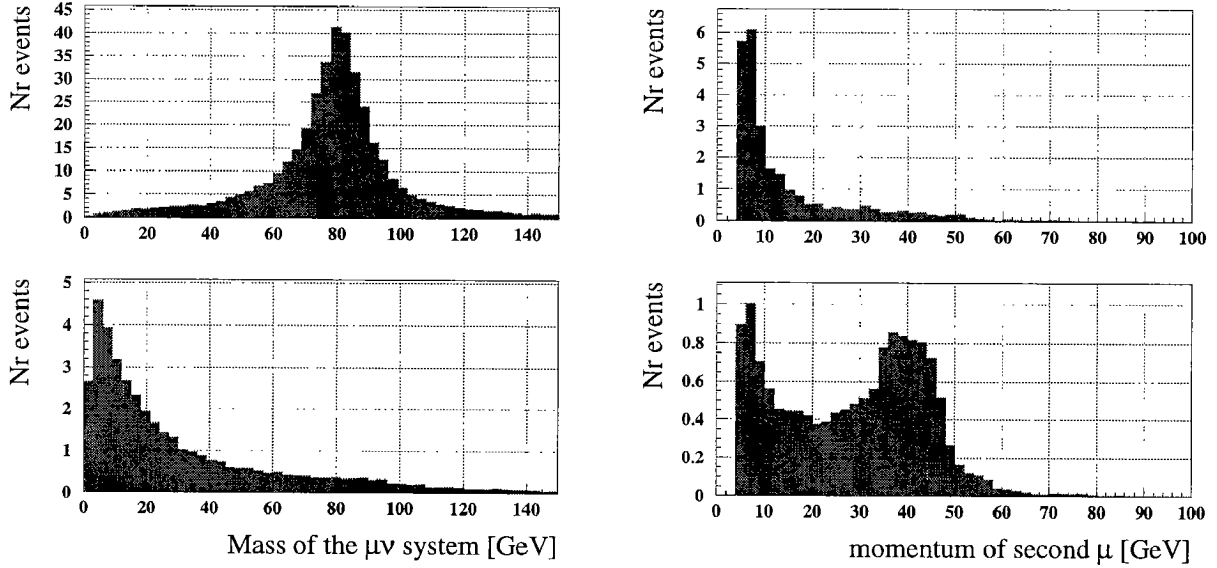
Figure 4.7: Distributions of mass of the μν system (left) and momentum of the second most energetic muon (right) in WW → qqμν events (top), and ZZ events (bottom). Events are generated at $\sqrt{s}$ = 189 GeV. Plots are normalized to an integrated luminosity of 200 pb^{-1}.

around the Z mass however, could bias the measurement of the mass of the W boson, and makes the rejection of this background more important than one could expect from the cross section estimate.

Rejection of $e^+e^- \rightarrow e^+e^-$ + hadrons

The two-photon process is characterized by a large amount of missing energy carried away by the electron and positron scattered at very low angle and thus escaping along the beam pipe. The very low polar angle of the missing momentum vector can be used to discriminate this channel from the $qq\mu\nu$ signal. The distribution of the cosine of the polar angle of missing momentum for WW and $\gamma\gamma$ is shown in Fig. 4.8. A cut at a high value of $\cos\theta_{miss}$ will reject most of the $\gamma\gamma$ background, but will be also effective in rejecting the Z/γ events, where a part of the hadrons in a jet is going undetected along the beam pipe. Also, in the presence of a
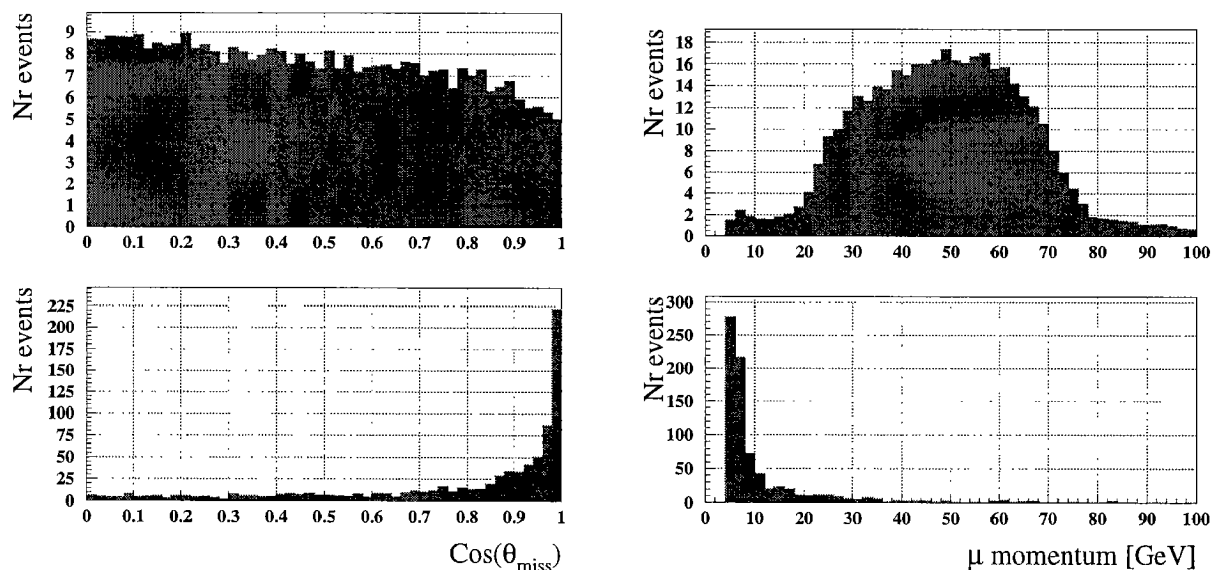
Figure 4.8: Cosine of the polar angle of the missing momentum vector (left), and muon momentum (right) in WW $\rightarrow$ $qq\mu\nu$ events (top), and in two-photon events (bottom). Both samples were generated at $\sqrt{s} = 189$ GeV. Plots are normalized to an integrated luminosity of 200 pb^{-1}.

muon, the muon momentum tends to be very low, as can be also seen in Fig. 4.8. Most of the $\gamma\gamma$ events are rejected due to more than one cut, and therefore this channel is rather simple to discriminate.

However, two photon events tend to have a low mass of the hadronic system, due to the low amount of energy scattered in the detector volume, and could bias the mass measurement to lower values. The huge two-photon cross cross section makes an efficient rejection of this background process important.

4.2 Other WW Decay Channels

In the Standard Model, the WW $\rightarrow$ $qq\mu\nu$ channel represents 14.6% of the final states of the WW process. The precise measurement of the total WW cross section requires therefore efficient

and pure selection of all the decay channels. In particular, the W mass measurement relies on the highest possible statistics, and thus on the selections of all the final states mediated by the W pair production. The different WW final states shall be described in the following, the detailed descriptions are given in [45, 46].

WW → qqeν

The WW → qqeν final state is very similar to WW → qq$\mu\nu$, with the obvious difference of the presence of a highly energetic electron in the final state in the place of the muon. The main difference comes from the contribution from single W production [47]. The signature of an electron in L3 was described in Sec. 2.5. Electrons arising from the decays of hadrons are rejected by requiring the electron to be isolated from the hadronic system, by setting a maximum on the energy deposit not associated with the electron, but being deposited in a narrow cone around the electron's direction. A minimum electron energy is required. As in the qq$\mu\nu$ case, after having removed the electron from the event, the remainder is grouped in two jets. Again, cuts on the invariant masses of the hadronic and the electron-neutrino systems are imposed, as well as on the cosine of the polar angle of the missing momentum vector.

The efficiencies obtained using this selection at $\sqrt{s}$ = 183 GeV and 189 GeV are listed in Tab. 4.2.

$\sqrt{s}$ [GeV]	$\epsilon_{qqe\nu}$ [%]	$\epsilon_{qq\mu\nu}$ [%]	$\epsilon_{qq\tau\nu}$ [%]	σ_{acc}^{non-WW} [pb]
183	85.4	0.2	2.1	0.12
189	82.9	0.3	1.7	0.08

Table 4.2: Selection efficiencies and accepted non-WW background in the qqeν selection at $\sqrt{s}$ = 183 and 189 GeV.

WW → qq$\tau\nu$

The selection of the qq$\tau\nu$ final state is based on the identification of the tau jet in a hadronic event with missing energy. WW → qq$\tau\nu$ events contain at least two neutrinos, therefore two cuts were introduced for event identification: a maximum value of the difference between the visible energy and the missing momentum, and a minimum value of the sum of missing momentum and the visible mass are required.

In the case of the τ decaying into electron or muon, a maximum cut on the invariant mass of the lepton-neutrino system is applied, in order to reject qqeν and qq$\mu\nu$ events.

Where no electron and muon is found, the event is clustered into at least three jets, and the hadronically decaying τ is identified using a neural network based on the following input variables: number of TEC tracks, number of calorimetric clusters associated with the jet, the opening angle of the jet, the jet's electromagnetic energy and it's mass. The probability of correctly identifying the τ jet using this approach is above 80%. Further, the identified τ jet has to have between one and three TEC tracks, and a cut on the polar angle of the missing momentum vector is applied.

After having removed the constituents of the identified tau lepton, the event is forced to cluster in two hadronic jets, and the mass of the jet-jet system is required to lie inside a broad window around the expected W mass. Also, on the mass of the tau-neutrino system a similar cut is imposed.

39

The efficiencies obtained using this selection at $\sqrt{s} = 183$ and 189 GeV are listed in Tab. 4.3. The τ decay including an additional neutrino results in a shift of the energy of the visible lepton towards lower values, which is more populated by background, as can be seen e.g. in Fig. 4.6. The hadronic decay of the τ results in a final state with three jets, with the typical background of $e^+e^- \rightarrow Z/\gamma \rightarrow q\bar{q}$ with gluon radiation. The less specific signature of the τ decay is thus reflected in the loss of efficiency as compared to the $qq\mu\nu$ and $qqe\nu$ final states.

$\sqrt{s}$ [GeV]	$\epsilon_{qq\tau\nu}$ [%]	$\epsilon_{qqe\nu}$ [%]	$\epsilon_{qq\mu\nu}$ [%]	σ_{acc}^{non-WW} [pb]
183	50.1	4.8	6.0	0.19
189	50.6	5.3	6.5	0.24

Table 4.3: Selection efficiencies and accepted non-WW background in the $qq\tau\nu$ selection at $\sqrt{s} = 183$ and 189 GeV.

WW $\rightarrow$ lνlν

This channel requires two charged leptons and missing energy due to the two undetected neutrinos. The selection requirements are based therefore on low multiplicity of tracks and calorimetric clusters. The visible energy is required to be between 2% and 80% of $\sqrt{s}$. Depending on whether the event contains zero, one or two identified electrons or muons, it is classified to belong to jet-jet, lepton-jet or lepton-lepton class. In all the classes, the missing transverse energy must be at least 10% of the visible energy, and a maximum cut on the cosine of the polar angle of the missing momentum vector is imposed. Cosmic rays are rejected by means of maximum distance of closest approach of the muon to the interaction point and maximum scintillator time.

In the lepton-lepton class, the energy of the two leptons must lie in an interval consistent with the momentum spectrum of a lepton from W decay. Due to lepton universality, this spectrum looks like in Fig. 4.6 also for the electron. At $\sqrt{s} = 183$ GeV, these cuts were set at a minimum of 20 GeV and 5 GeV for the two highest energetic leptons, respectively; while the maximum cut was set at 80 GeV. Rejection of $e^+e^- \rightarrow l^+l^-$ events is accomplished by requiring a minimum acoplanarity of 8°.

In the lepton-jet class, the energy of the electron or muon must again be compatible with the lepton energy from a W decay. In addition, a jet with at least 8 GeV (at $\sqrt{s} = 183$ GeV) is required. Also here, the acoplanarity between lepton and the jet, but also between the lepton and any TEC track must be at least 8°. A veto on identified photons of more than 10 GeV is imposed.

In the jet-jet class, two or three jets are required in the event. A minimum cut on the energy of the two most energetic jets is applied. Due to the decay of the two τ leptons, at least two tracks in the central tracker are required, with both jets matching at least one track each. The sum of the energies of reconstructed photons must not exceed 50 GeV.

The efficiencies obtained using this selection at $\sqrt{s} = 183$ and 189 GeV are listed in Tab. 4.4.

WW $\rightarrow$ qqqq

The fully hadronic final state is characterized by high multiplicity in the tracker and the calorimeters. The events must have a minimum visible energy of 70% of $\sqrt{s}$, and a longi-

Selection channel	$\sqrt{s}$[GeV]	Efficiency [%] in channel						σ_{acc}
		$e\nu e\nu$	$e\nu\mu\nu$	$e\nu\tau\nu$	$\mu\nu\mu\nu$	$\mu\nu\tau\nu$	$\tau\nu\tau\nu$	
$e^+e^- \to WW \to e\nu e\nu$	183	62.1	0.1	11.0			1.9	0.026
	189	60.9	0.1	10.3			0.9	0.026
$e^+e^- \to WW \to e\nu\mu\nu$	183		56.5	9.0	0.1	9.1	1.1	0.014
	189		57.4	10.1	0.2	9.4	2.3	0.014
$e^+e^- \to WW \to e\nu\tau\nu$	183	8.0	1.4	37.6		0.3	9.3	0.068
	189	9.4	1.2	39.0		0.2	10.3	0.068
$e^+e^- \to WW \to \mu\nu\mu\nu$	183				45.6	6.8	0.5	0.002
	189				49.1	8.7	1.0	0.002
$e^+e^- \to WW \to \mu\nu\tau\nu$	183		4.1	0.5	2.7	33.2	7.7	0.022
	189		4.9	0.5	2.3	33.9	8.2	0.022
$e^+e^- \to WW \to \tau\nu\tau\nu$	183	0.2	0.2	3.6		1.2	22.0	0.043
	189	0.4	0.2	2.8		1.0	23.6	0.043

Table 4.4: Selection efficiencies and accepted non-WW background in the lνlν selection at $\sqrt{s} = 183$ and 189 GeV.

tudinal energy imbalance of at most 25% of the visible energy. The events are forced to cluster in four jets, with the Durham parameter y_{34} of at least 0.0015. To suppress $e^+e^- \to q\bar{q}$ background with hard radiative photons in the detector, events are rejected if they contain an electromagnetic cluster with more than 40 GeV, or if more than 80% of the energy of any jet is attributed to the most energetic photon. A veto on the presence of a muon with more than 25 GeV is set. Two pairs of jets are formed in such a way that the mass difference of the two reconstructed W bosons is minimal. The correct pairing is found in ~ 75% of the cases.

The final selection is performed by means of a neural network. The input variables are the minimal and maximal jet energy, the minimal jet-jet opening angle, minimal jet cluster multiplicity, y_{34}, spherocity, difference of the two W masses and the average mass of two jets when the event is reconstructed as a two jet event.

For the determination of the WW cross section, the output distribution of the neural network for data events is fitted by a linear combination of neural network distributions derived from Monte Carlo simulations for signal and background. This cross section is the one quoted by L3 [44]. For event selection, as is needed for mass or couplings measurement, a cut is set on the output distribution at a value which minimizes the expected statistical error. The cross section measured in this way is in good agreement with the above method.

The efficiencies obtained using this selection at $\sqrt{s} = 183$ and 189 GeV are listed in Tab. 4.5.

$\sqrt{s}$ [GeV]	ϵ_{qqqq} [%]	$\epsilon_{qqe\nu}$ [%]	$\epsilon_{qq\tau\nu}$ [%]	σ_{acc}^{non-WW} [pb]
183	87.5	0.3	1.7	1.46
189	88.9	0.3	0.9	1.46

Table 4.5: Selection efficiencies and accepted non-WW background in the qqqq selection at $\sqrt{s} = 183$ and 189 GeV.

Seite Leer /
Blank leaf

42

Chapter 5

WW Cross Section Measurement

The cross section of a process relates the number of events N to the collected luminosity $L = \int \mathcal{L} dt$ by $N = \sigma L$. In the presence of N_{bkg} background events, with the signal selection efficiency of ϵ_{sig} and the total integrated luminosity L, the signal cross section for the $e^+e^- \to$ WW $\to$ qq$\mu\nu$ process is determined to be

$$\sigma_{\text{qq}\mu\nu} = \frac{N_{sel} - N_{bkg}}{\epsilon_{sig} L}, \tag{5.1}$$

where N_{sel} is the total number of data events which passed the qq$\mu\nu$ selection. N_{bkg} has to be estimated from the efficiency of the selection applied to a background channel i, ϵ^i_{bkg}, the Standard Model cross section of the background process σ^i_{bkg} and the luminosity. It is the sum over all contributing background processes:

$$N_{bkg} = \sum_i \epsilon^i_{bkg} \sigma^i_{bkg} L = \sum_i \sigma^i_{acc} L. \tag{5.2}$$

The signal as well as background efficiencies are determined using Monte Carlo event samples after full detector simulation. The trigger efficiency for the qq$\mu\nu$ events is taken to be 100%, due to the high redundancy given by the activity in the muon chambers, the inner tracker and the calorimeters. Nevertheless, the estimation of efficiency by using real detector simulation ensures also that possible trigger inefficiencies are properly taken into account.

The statistical error on the cross section is given by

$$\Delta\sigma^{stat}_{\text{qq}\mu\nu} = \frac{\sqrt{N_{sel}}}{\epsilon_{sig} L}, \tag{5.3}$$

while the uncertainty due to N_{bkg} is quoted in the systematic error, as shown in the next section.

5.1 Systematic Effects

The main systematic effects relevant for the cross section measurement arise from the uncertainty on the selection efficiencies for the signal and background, and from the choice of selection cut positions. The background cross sections are calculated using high statistics Monte Carlo samples and the errors on these quantities are determined to be on the permille level, and thus negligible.

43

Assuming binomial distribution of selected and rejected events, the statistical error on the signal efficiency reads

$$\Delta\epsilon_{sig} = \sqrt{\frac{\epsilon_{sig}(1 - \epsilon_{sig})}{N^{MC}_{qq\mu\nu}}}, \tag{5.4}$$

where $N^{MC}_{qq\mu\nu}$ is the total amount of $qq\mu\nu$ events in the WW Monte Carlo sample. The errors on background efficiencies, $\Delta\epsilon^i_{bkg}$ are calculated in the same way. The uncertainties on the calculation of the efficiencies propagate in the measurement of the cross section, and are quoted as systematic errors[1]:

$$\Delta\sigma^{sig.effi}_{qq\mu\nu} = \sigma_{qq\mu\nu}\frac{\Delta\epsilon_{sig}}{\epsilon_{sig}}, \tag{5.5}$$

$$\Delta\sigma^{bkg.effi}_{qq\mu\nu} = \sqrt{\sum_i(\frac{\sigma^i_{bkg}}{\epsilon_{sig}}\Delta\epsilon^i_{bkg})^2}. \tag{5.6}$$

The systematic uncertainties given by the selection cuts, $\Delta\sigma^{cut}_{qq\mu\nu}$ were determined by varying the cut positions within a small range around the actual value, and calculating the change in differential cross section.

Since all the above errors are basically statistical iin nature, they are added up in quadrature to obtain the total systematic error on the $e^+e^- \to WW \to qq\mu\nu$ cross section measurement:

$$\Delta\sigma^{syst}_{qq\mu\nu} = \sqrt{(\Delta\sigma^{sig.effi}_{qq\mu\nu})^2 + (\Delta\sigma^{bkg.effi}_{qq\mu\nu})^2 + (\Delta\sigma^{cut}_{qq\mu\nu})^2}. \tag{5.7}$$

5.2   WW $\to$ qq$\mu\nu$ Cross Section at $\sqrt{s} = 183$ GeV

The data sample collected at $\sqrt{s} = 183$ GeV corresponds to an integrated luminosity of $L = 55.464 \pm 0.062$ pb^{-1}.

To optimize the selection cuts, a signal Monte Carlo was used with 252000 WW events generated with the KORALW [48] event generator, which corresponds to more than 200 times higher statistics than the expected number of data events. The non-WW background was studied using high statistics Monte Carlo samples as given in Tab. 5.3.

The cut positions were determined by plotting the distribution of the cut variable for selected signal and background MC events, with all cuts applied but the one in question ('N-1' distributions). The position was chosen for each variable, such that it optimized separation of signal from background while keeping high signal efficiency. Only Monte Carlo events were used to determine cut values.

The cuts applied at this energy are summarized in Tab. 5.1. Two samples of cuts were used, depending on whether the muon was identified in the muon chambers (MUTK) or as a MIP. Since the MIP finding algorithm applies more stringent criteria on the DCA and ZDCA of the track, than can be required from the muon spectrometer measurement, there was no explicit cut set on this values in the MIP selection. The N-1 distributions with data points are shown in Figs 5.1-5.3 for the MUTK selection. There is overall a very good agreement between data and

---

[1]The formulae are explained in App. B

Cut variable	Muon Detector	MIP
Muon DCA	< 80 mm	
Muon ZDCA	< 120 mm	
Nr of clusters	> 10	> 10
Nr of tracks	> 5	> 8
Muon momentum	> 20 GeV	> 20 GeV
Angle(muon,jet)	> 10°	> 20°
Mass of jet system	> 45 GeV	> 50 GeV
	< 120 GeV	< 110 GeV
Mass of $\mu\nu$ system	> 45 GeV	> 30 GeV
|Cos(polar angle of missing momentum)|	< 0.98	< 0.91
Secondary muon momentum	< 30 GeV	< 30 GeV

Table 5.1: Cut positions used for $e^+e^- \to WW \to qq\mu\nu$ selection at $\sqrt{s} = 183$ GeV.

Monte Carlo simulation. Figs 5.4-5.6 show the N-1 distributions in the MIP selection. Plots of DCA and ZDCA distributions are displayed as well, though no expicit cut was applied on these values, as explained above. Taking limited statistics into account, also the MIP distributions show a good agreement of data and simulation.

The signal efficiency as well as the cross efficiencies for W-pair mediated background processes are listed in Tab. 5.2, while the accepted cross section of non-WW processes is shown in Tab. 5.3. The resulting purity of the selected $qq\mu\nu$ sample is 93%.

Applying this selection to the $\sqrt{s} = 183$ GeV data, 94 events were selected, 10 of these as MIP, while the expected number of events is 102. The 10 MIP events are in good agreement with the estimated 7% due to muon detector geometry.

The measured $e^+e^- \to WW \to qq\mu\nu$ cross section is

$$\sigma_{WW \to qq\mu\nu}(\sqrt{s} = 183 \text{ GeV}) = 2.087 \pm 0.234(stat.) \pm 0.047(syst.) \text{ pb}$$

with the first error being statistical, and the second systematic.

The systematic error is 0.23% due to the uncertainty in signal efficiency, and 0.18% due to background subtraction. The cut variation, the plots of which are shown in Fig. 5.7 (MUTK) and in Fig. 5.8 (MIP), amounts to 2.23% systematic error. The cuts have been varied in the range corresponding to the visible range of the plots. Table 5.4 gives the systematic error assigned for every cut variable.

Channel	Efficiency [%]
$e^+e^- \rightarrow WW \rightarrow qq\mu\nu$	**74.57**
$e^+e^- \rightarrow WW \rightarrow qqe\nu$	0.13
$e^+e^- \rightarrow WW \rightarrow qq\tau\nu$	3.71
$e^+e^- \rightarrow WW \rightarrow qqqq$	0.01

Table 5.2: Efficiency and cross efficiencies of the $qq\mu\nu$ selection at $\sqrt{s} = 183$ GeV.

Process	σ_{SM}[pb]	Nr of events	σ_{acc}[fb]
$e^+e^- \rightarrow Z/\gamma \rightarrow q\bar{q}$	107.8	800000	42.8
$e^+e^- \rightarrow ZZ \rightarrow f\bar{f}f\bar{f}$	0.59	30000	7.5
$e^+e^- \rightarrow e^+e^- +$ hadrons	15360	1800000	0.0

Table 5.3: MC sample parameters and accepted cross section of non-WW background processes at $\sqrt{s} = 183$ GeV.

Figure 5.1: Distributions of event parameters on which cuts were imposed at $\sqrt{s} = 183$ GeV in the MUTK selection. Dots represent data events. For every histogramm, all other cuts apart from the one displayed are applied. Values at which the cuts were set are indicated by arrows.

Figure 5.2: Distributions of event parameters on which cuts were imposed at $\sqrt{s} = 183$ GeV in the MUTK selection. Dots represent data events. For every histogramm, all other cuts apart from the one displayed are applied. Values at which the cuts were set are indicated by arrows.
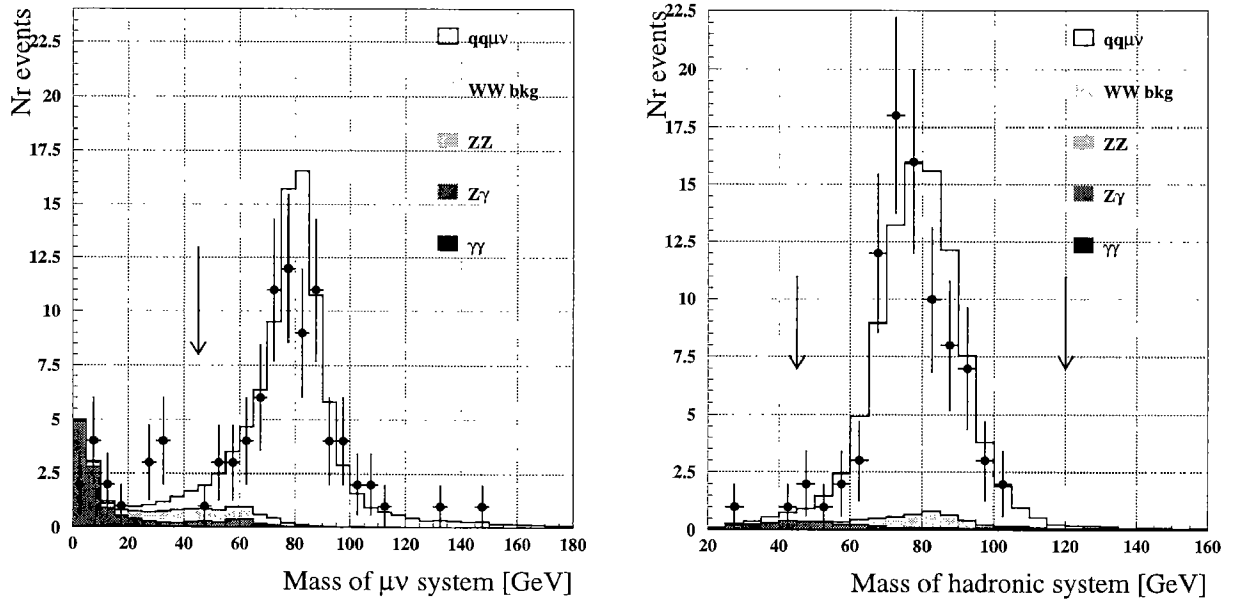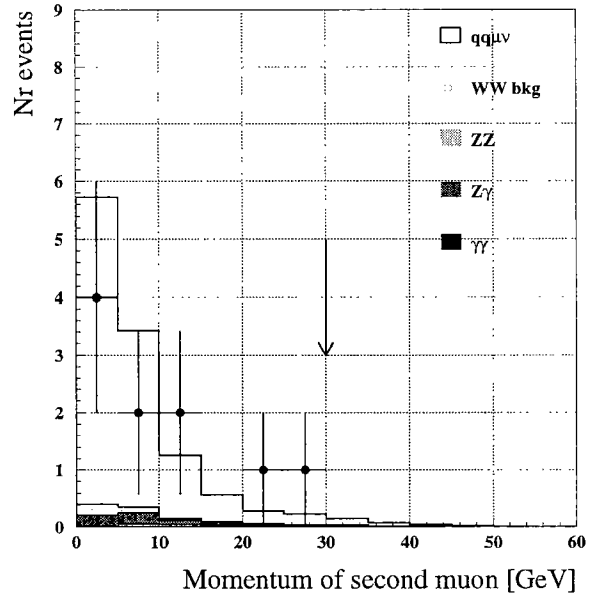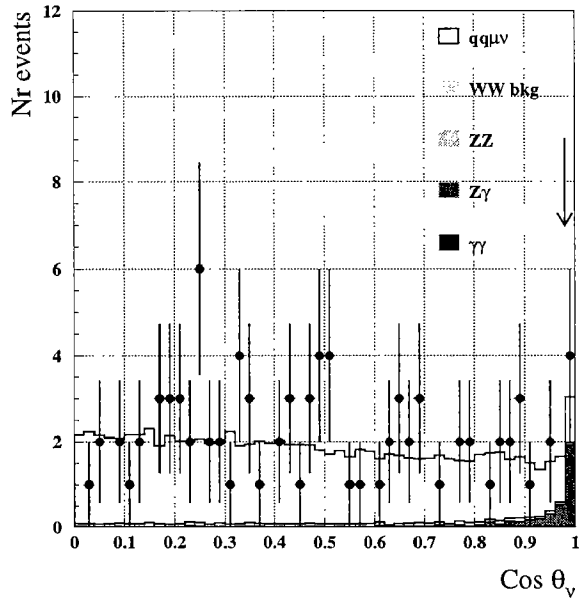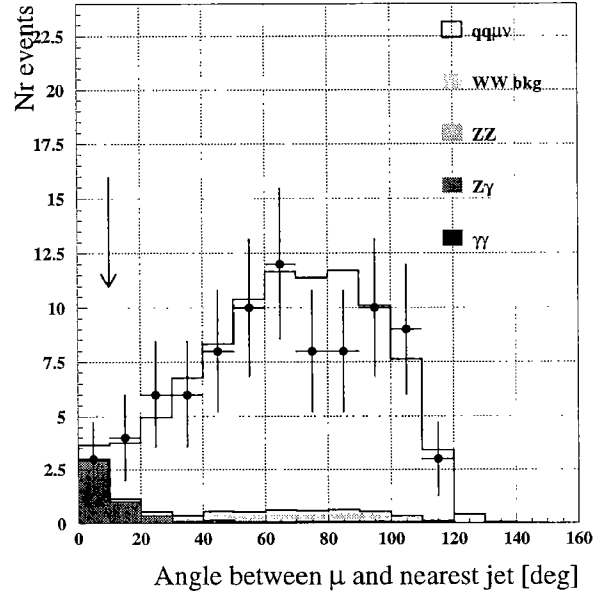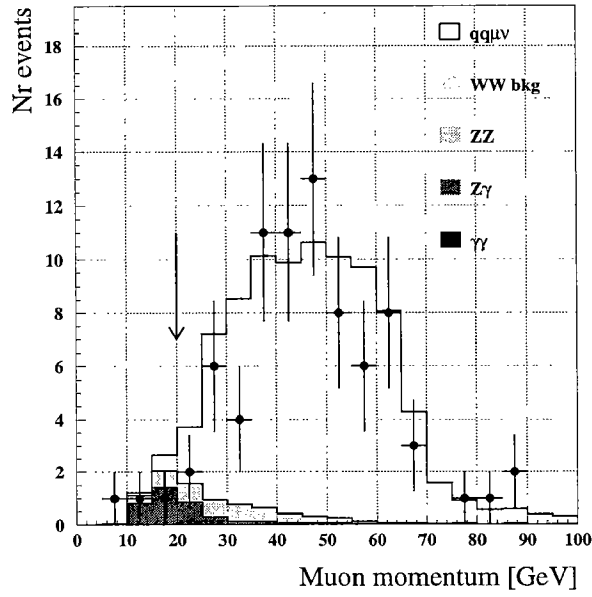
Figure 5.3: Distributions of event parameters on which cuts were imposed at $\sqrt{s} = 183$ GeV in the MUTK selection. Dots represent data events. For every histogramm, all other cuts apart from the one displayed are applied. Values at which the cuts were set are indicated by arrows.
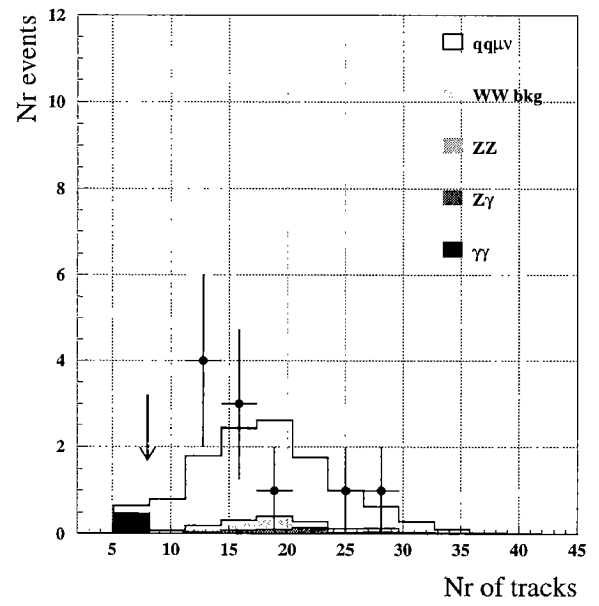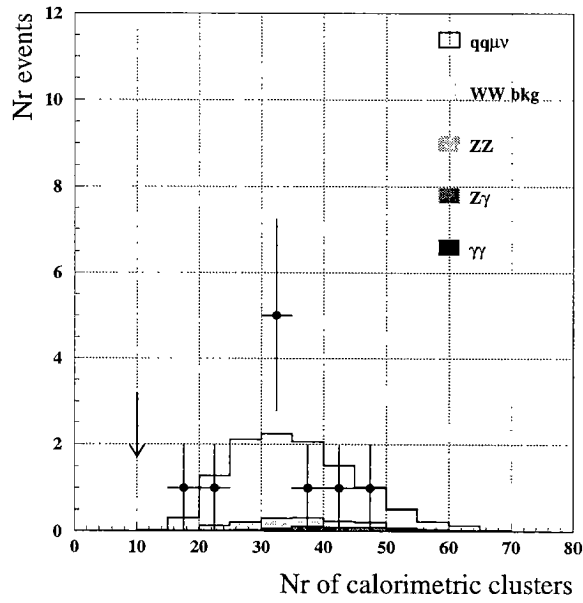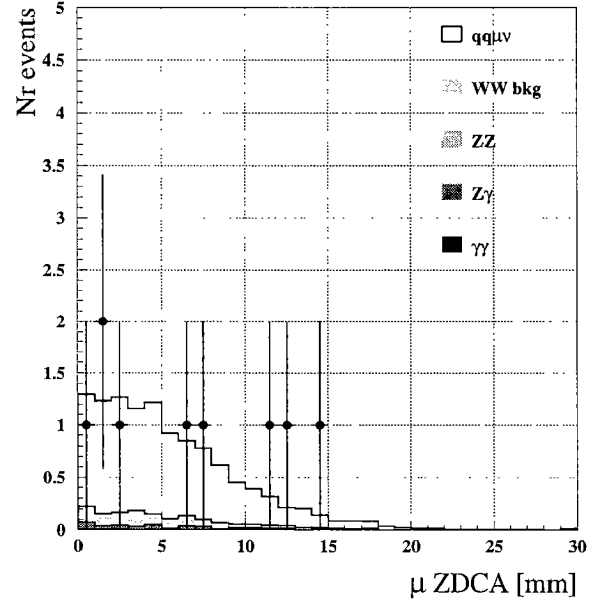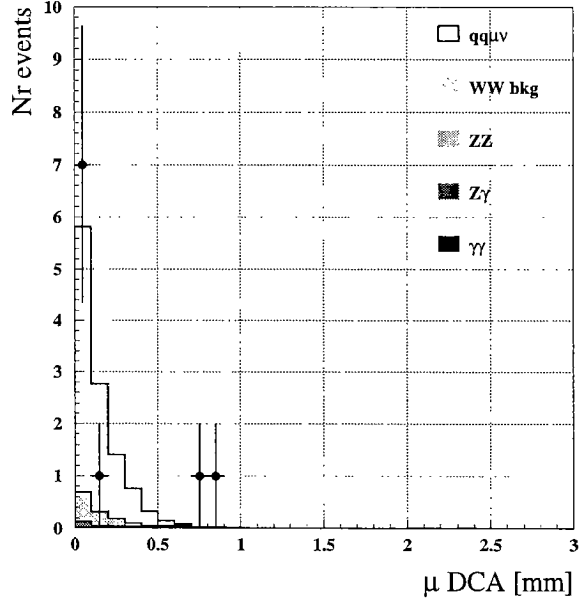
Figure 5.4: Distributions of event parameters on which cuts were imposed at $\sqrt{s} = 183$ GeV in the MIP selection. Dots represent data events. For every histogramm, all other cuts apart from the one displayed are applied. Valu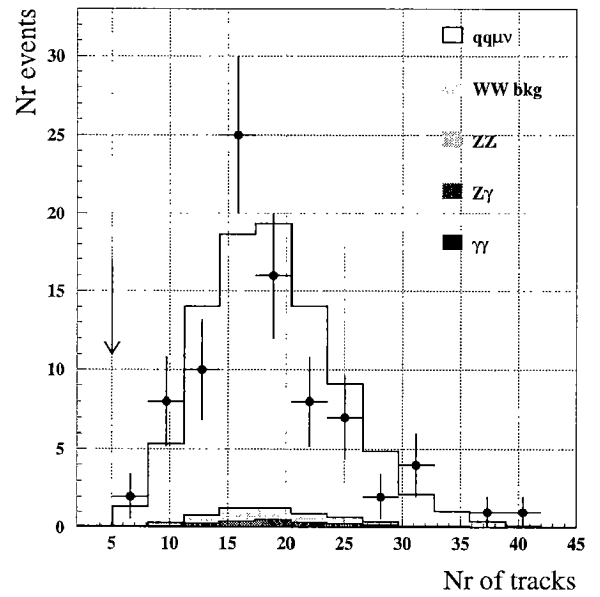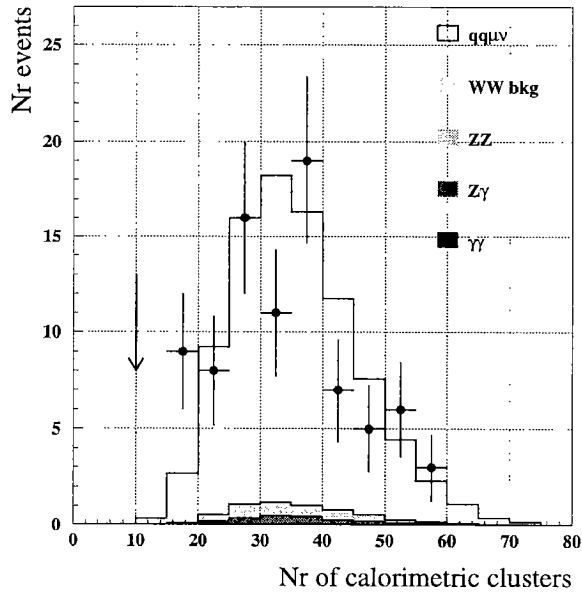es at which the cuts were set are indicated by arrows. No implicit cuts were applied in the selection on the DCA ans ZDCA of the MIPs.
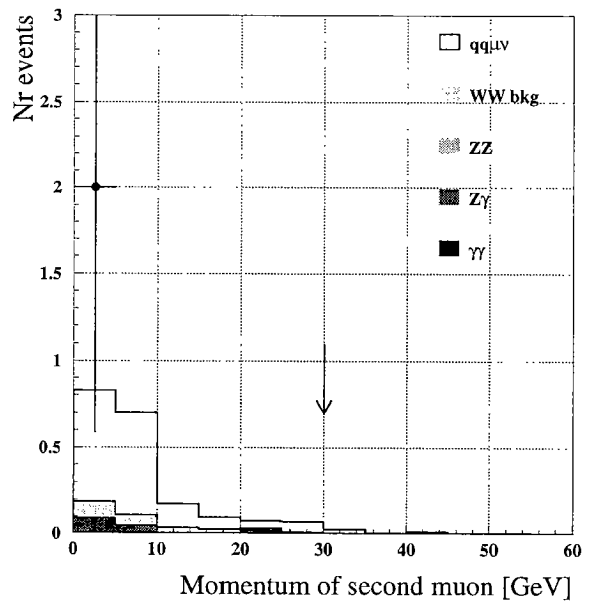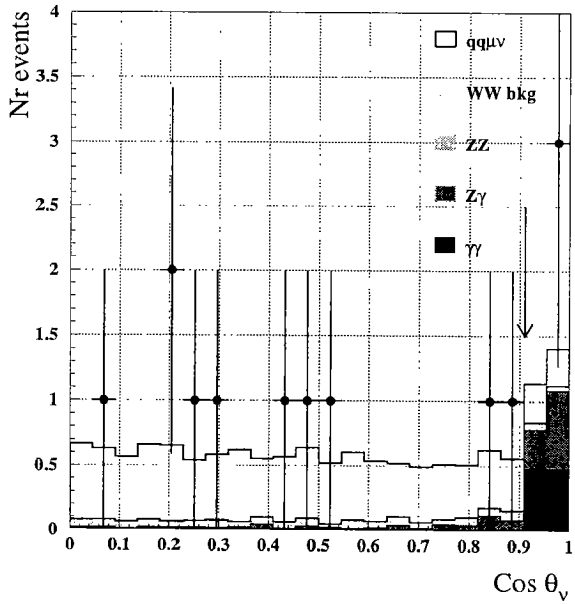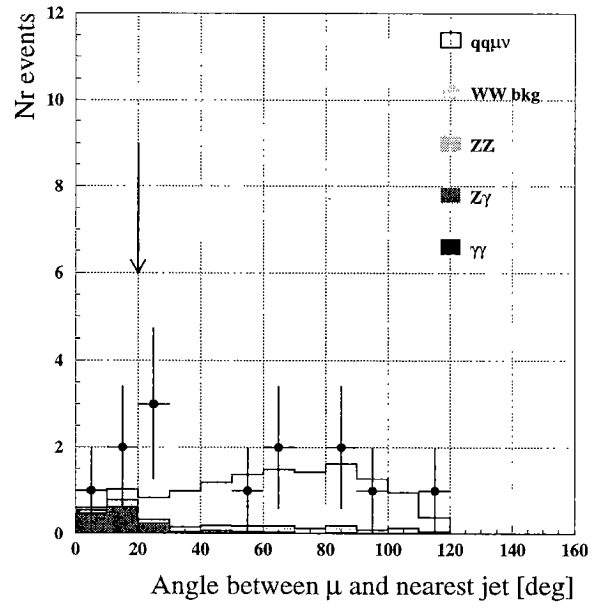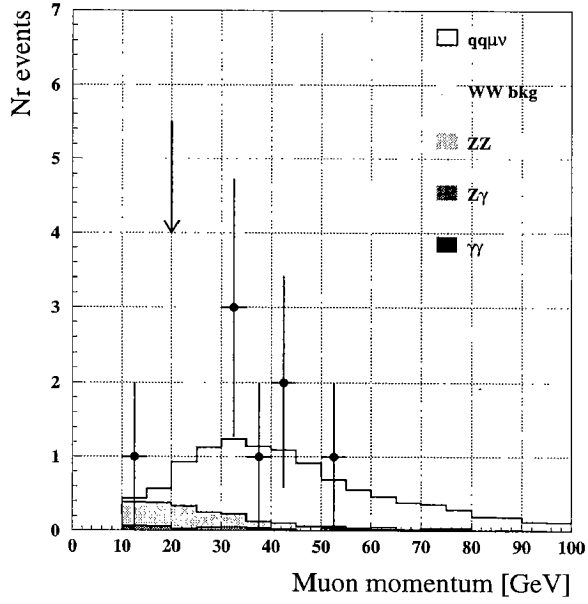
Figure 5.5: Distributions of event parameters on which cuts were imposed at $\sqrt{s} = 183$ GeV in the MIP selection. Dots represent data events. For every histogramm, all other cuts apart from the one displayed are applied. Values at which the cuts were set are indicated by arrows.
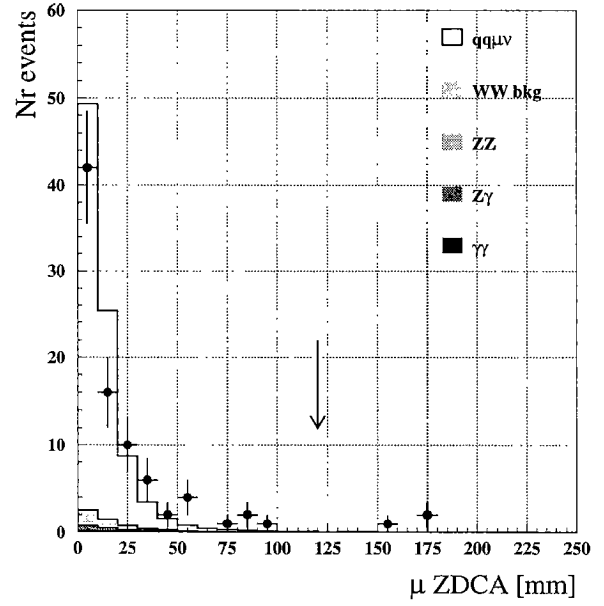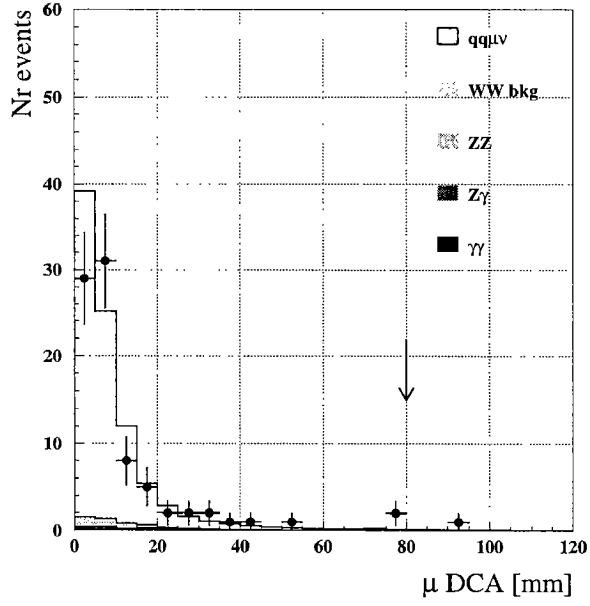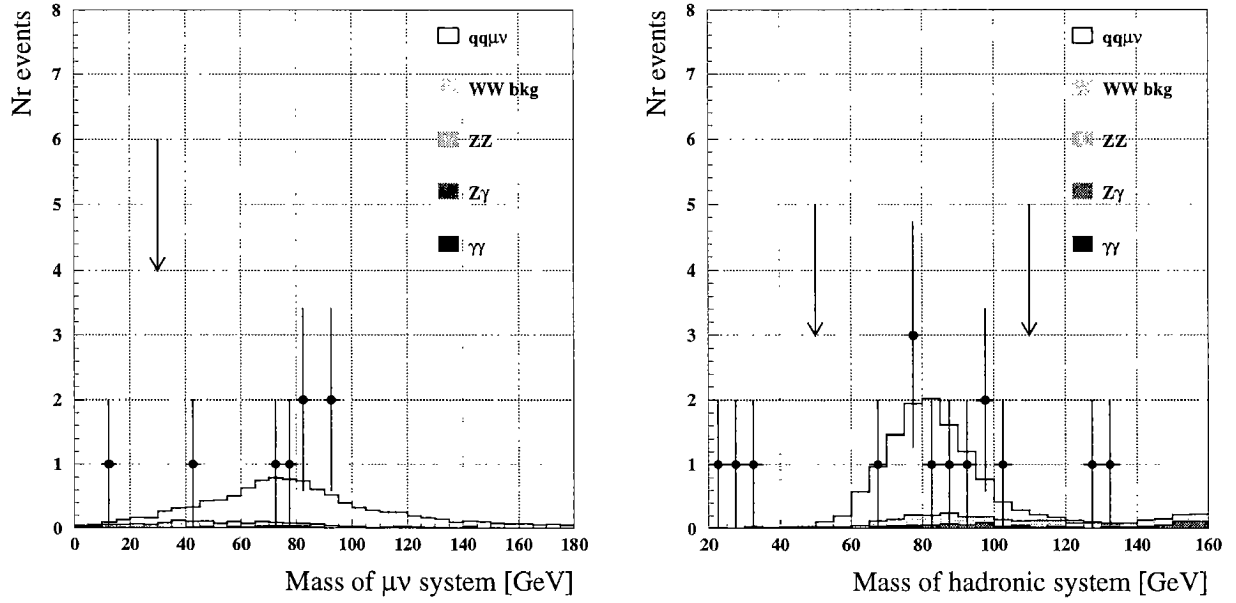
Figure 5.6: Distributions of event parameters on which cuts were imposed at $\sqrt{s} = 183$ GeV in the MIP selection. Dots represent data events. For every histogramm, all other cuts apart from the one displayed are applied. Values at which the cuts were set are indicated by arrows.

Cut variable	Muon Detector	MIP
Muon DCA	1.0%	0.0%
Muon ZDCA	0.0%	0.0%
Nr of clusters	0.0%	0%
Nr of tracks	0.1%	4.0%
Muon momentum	0.5%	2.0%
Angle(muon,jet)	0.5%	1.0%
Mass of jet system, lower cut	0.5%	0.2%
Mass of jet system, upper cut	0.1%	0.8%
Mass of $\mu\nu$ system	1.0%	0.5%
|Cos(polar angle of missing momentum)|	0.8%	4.0%
Secondary muon momentum	0.1%	0.5%
Total	**1.57%**	**6.18%**
Total for combined selection	**2.23%**	

Table 5.4: Systematic error from cut variation at $\sqrt{s} = 183$ GeV.
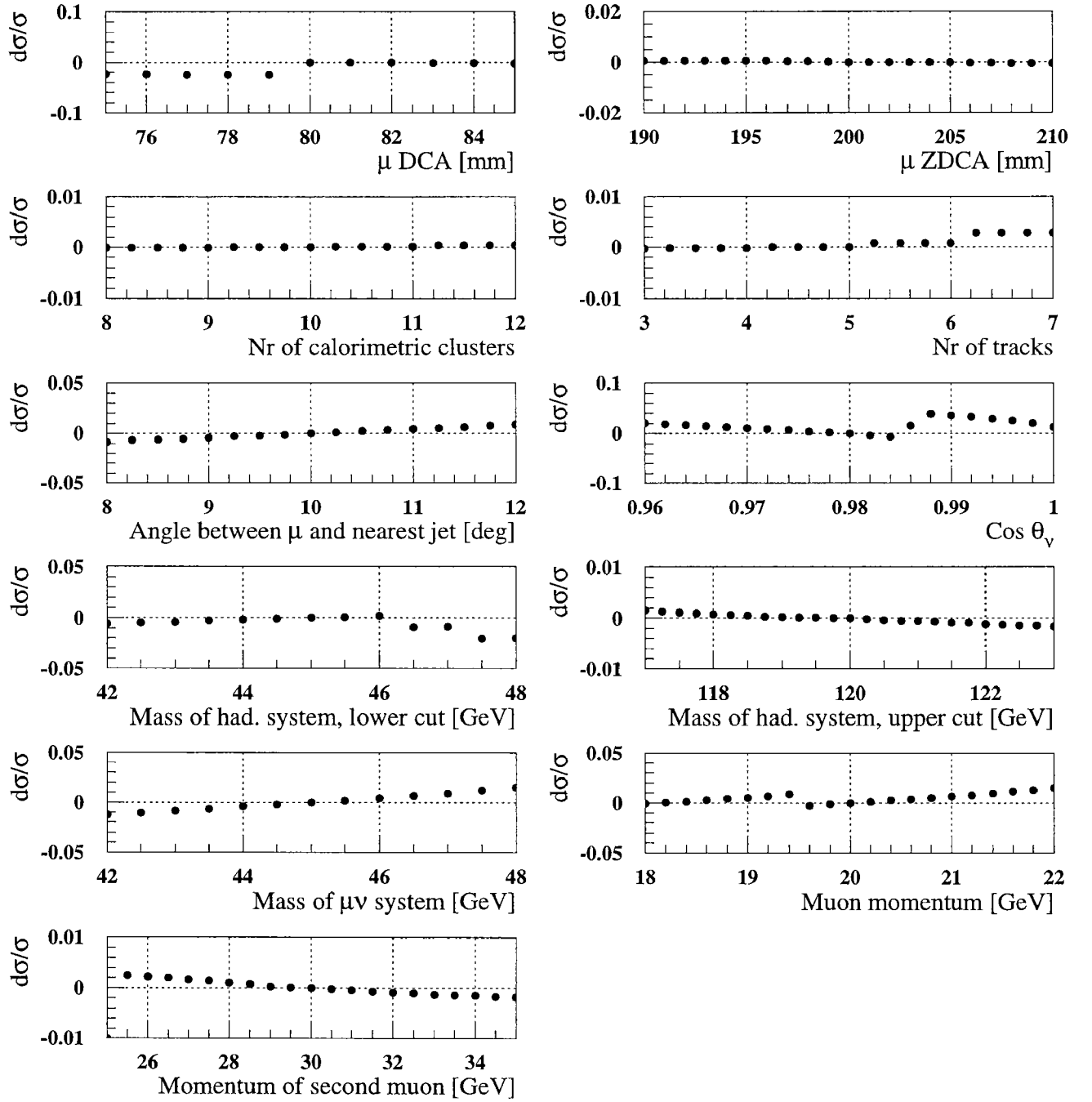
Figure 5.7: Relative change in measured cross section due to variation of cut position, for the cuts imposed at $\sqrt{s}$ = 183 GeV for muons identified due to their signature in the muon chambers.
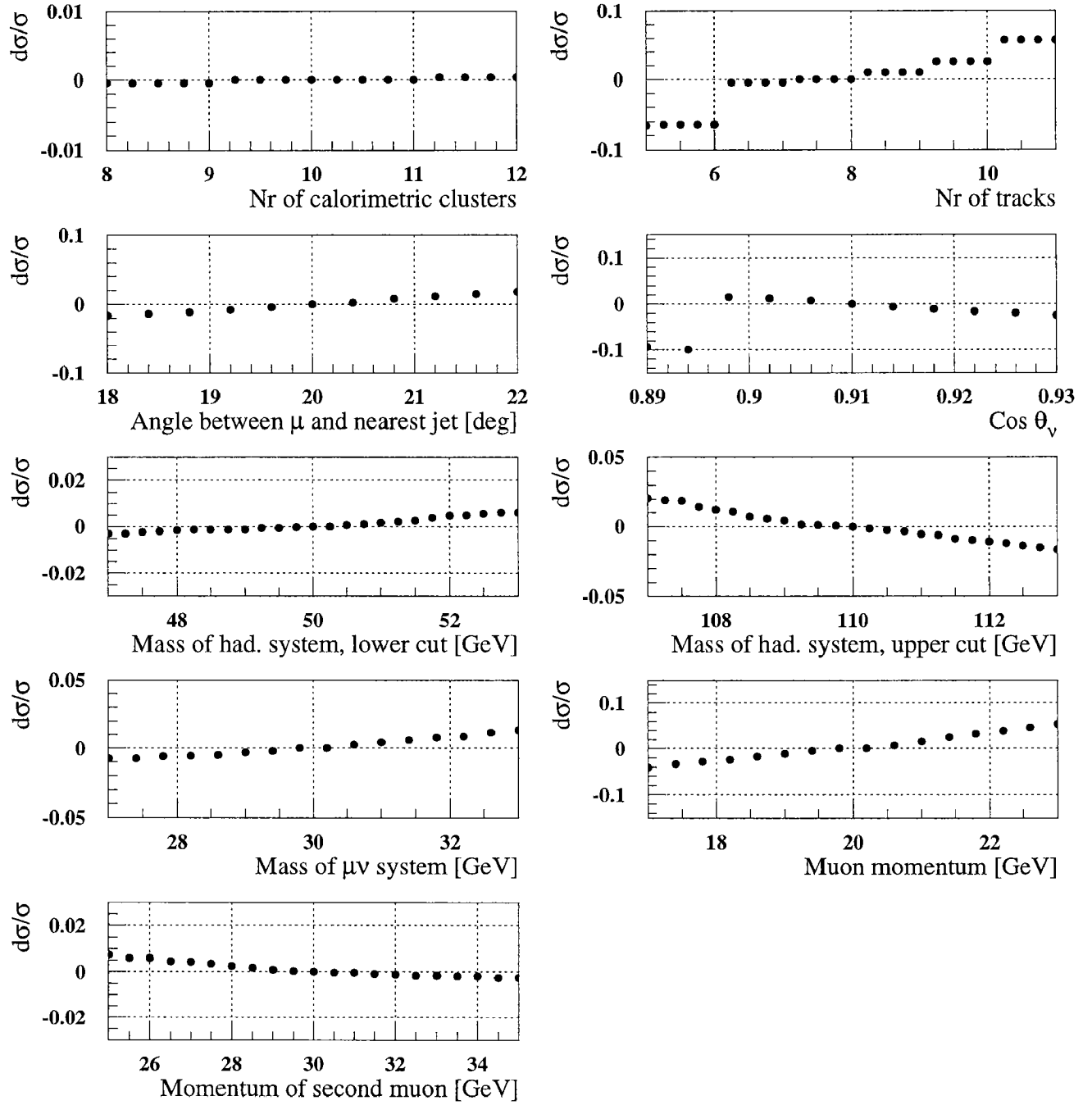
Figure 5.8: Relative change in measured cross section due to variation of cut position, for the cuts imposed at $\sqrt{s} = 183$ GeV for muons identified as MIP.

5.3 WW → qqμν Cross Section at $\sqrt{s} = 189$ GeV

The integrated luminosity at $\sqrt{s} = 189$ GeV amounts to $L = 176.773 \pm 0.115$ pb^{-1}. Since both energies, $\sqrt{s} = 183$ and 189 GeV, are well above the W pair production threshold, and the relative change in energy is small, the kinematics of the WW events doesn't change significantly. Therefore, the same selection was applied at both energies, the only change being the optimization of the cut positions.

For the $\sqrt{s} = 189$ GeV sample, 290000 simulated W pair events were used (KORALW [48]). The non-WW background sample parameters are listed in Tab. 5.7. The cuts applied are shown in Tab. 5.5. Again, no explicit cuts were set on the DCA and ZDCA values in the MIP selection. The N-1 distributions are shown in Figs 5.9-5.11 for the MUTK selection, and Figs 5.12-5.14 for the MIP selection. The selection efficiencies are listed in Tab. 5.6, and accepted non-WW cross section in Tab. 5.7.

The number of selected data events at $\sqrt{s} = 189$ GeV is 332, with 354 expected events. 22 of these events were selected as MIP, again in perfect agreement with the expectation of 7%.

The measured $e^+e^- \to$ WW $\to$ qqμν cross section is

$$\sigma_{\text{WW} \to \text{qq}\mu\nu}(\sqrt{s} = 189 \text{ GeV}) = 2.264 \pm 0.138(stat.) \pm 0.033(syst.) \text{ pb}$$

with the first error being statistical, and the second systematic.

The systematic error is 0.21% due to the uncertainty in signal efficiency, and 0.19% due to background subtraction. The cut variation, the plots of which are shown in Fig. 5.7 (MUTK) and in Fig. 5.8 (MIP), amounts to 1.44% systematic error. The cuts have been varied in the range corresponding to the visible range of the plots. Table 5.8 gives the systematic error assigned for every cut variable.

Cut variable	Muon Detector	MIP
Muon DCA	< 80 mm	
Muon ZDCA	< 200 mm	
Nr of clusters	> 10	> 10
Nr of tracks	> 5	> 5
Muon momentum	> 20 GeV	> 20 GeV
Angle(muon,jet)	> 10°	> 20°
Mass of jet system	> 40 GeV	> 40 GeV
	< 120 GeV	< 110 GeV
Mass of μν system	> 30 GeV	> 5 GeV
|Cos(polar angle of missing momentum)|	< 0.98	< 0.97
Secondary muon momentum	< 30 GeV	< 40 GeV

Table 5.5: Cut positions used for $e^+e^- \to$ WW $\to$ qqμν selection at $\sqrt{s} = 189$ GeV.

Channel	Efficiency [%]
$e^+e^- \to WW \to qq\mu\nu$	**74.90**
$e^+e^- \to WW \to qqe\nu$	0.09
$e^+e^- \to WW \to qq\tau\nu$	4.65
$e^+e^- \to WW \to qqqq$	0.01

Table 5.6: Efficiency and cross efficiencies of the $qq\mu\nu$ selection at $\sqrt{s} = 189$ GeV.

Process	$\sigma_{SM}[\mathrm{pb}]$	MC statistics	$\sigma_{acc}[\mathrm{fb}]$
$e^+e^- \to Z/\gamma \to q\bar{q}$	98.4	2900000	51.16
$e^+e^- \to ZZ \to f\bar{f}f\bar{f}$	0.97	200000	18.43
$e^+e^- \to e^+e^- + \mathrm{hadrons}$	15580.3	5900000	2.62

Table 5.7: MC sample parameters and accepted cross section of non-WW background processes at $\sqrt{s} = 189$ GeV.

Figure 5.9: Distributions of event parameters on which cuts were imposed at $\sqrt{s} = 189$ GeV in the MUTK selection. For every histogramm, all other cuts apart from the one displayed are applied. Values at which the cuts were set are indicated by arrows.
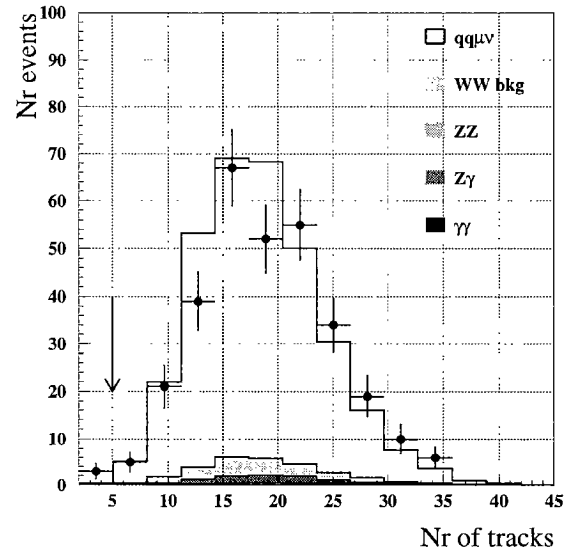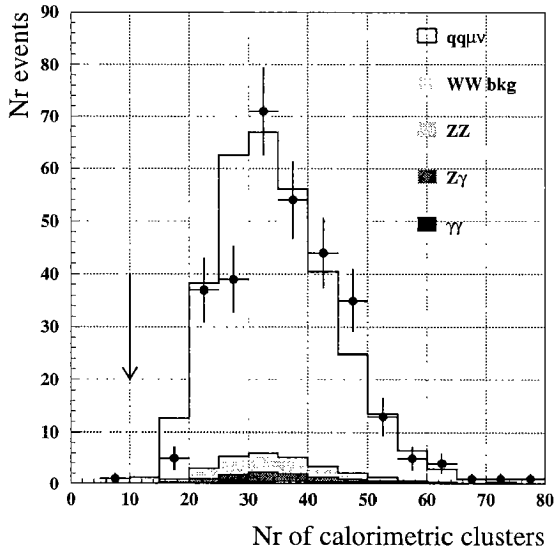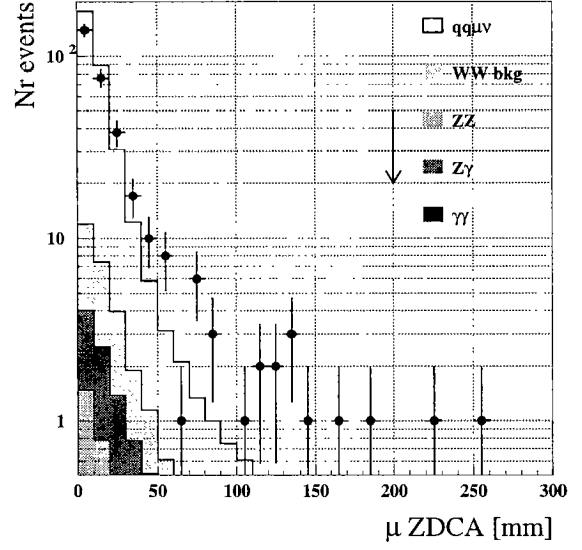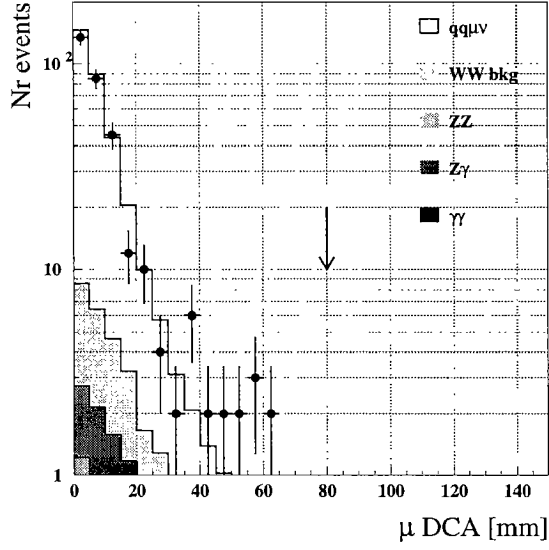
Figure 5.10: Distributions of event parameters on which cuts were imposed at $\sqrt{s} = 189$ GeV in the MUTK selection. Dots represent data events. For every histogramm, all other cuts apart from the one displayed are applied. Values at which the cuts were set are indicated by arrows.
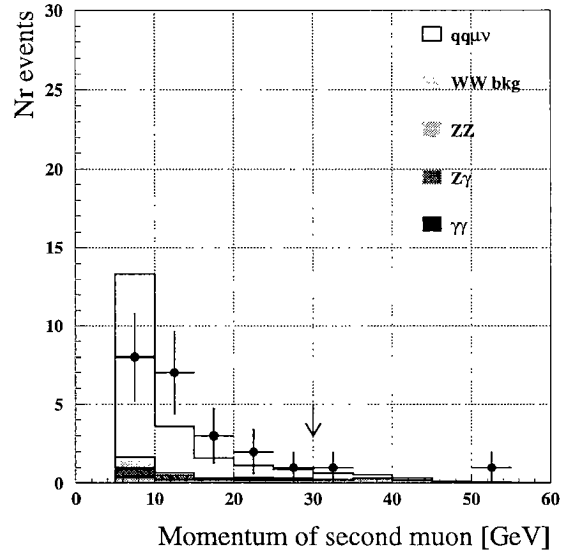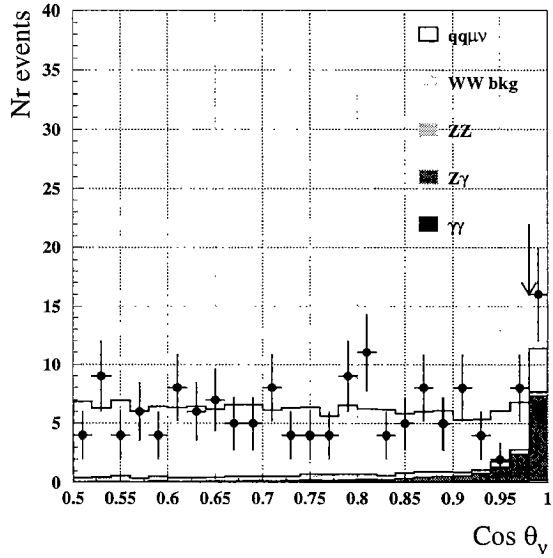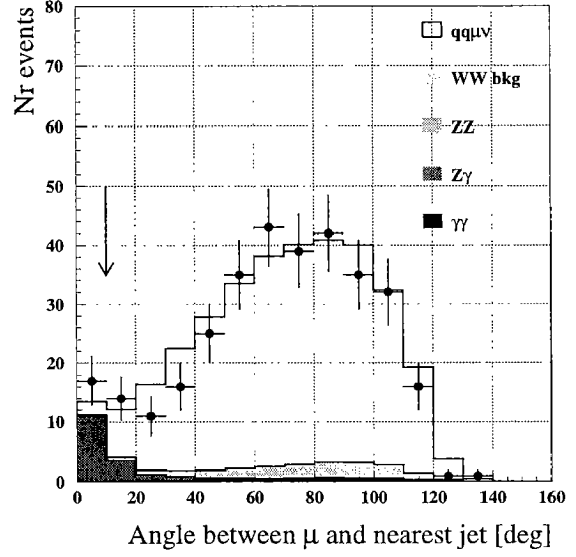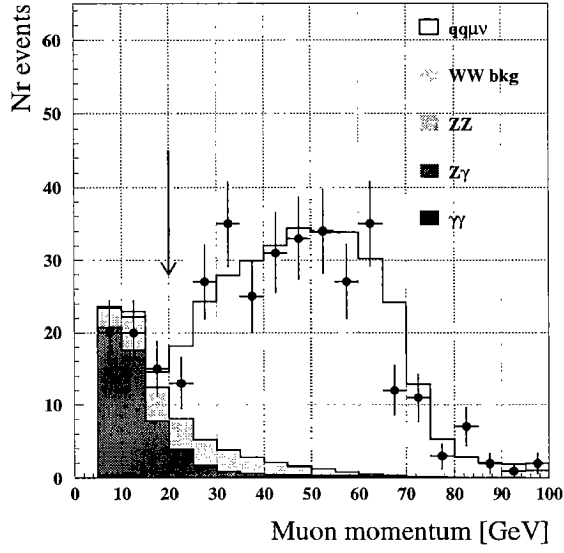
Figure 5.11: Distributions of event parameters on which cuts were imposed at $\sqrt{s} = 189$ GeV in the MUTK selection. Dots represent data events. For every histogramm, all other cuts apart from the one displayed are applied. Values at which the cuts were set are indicated by arrows.
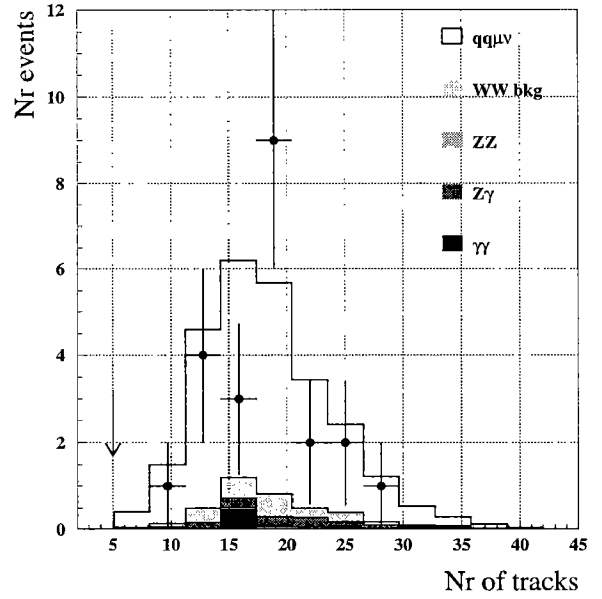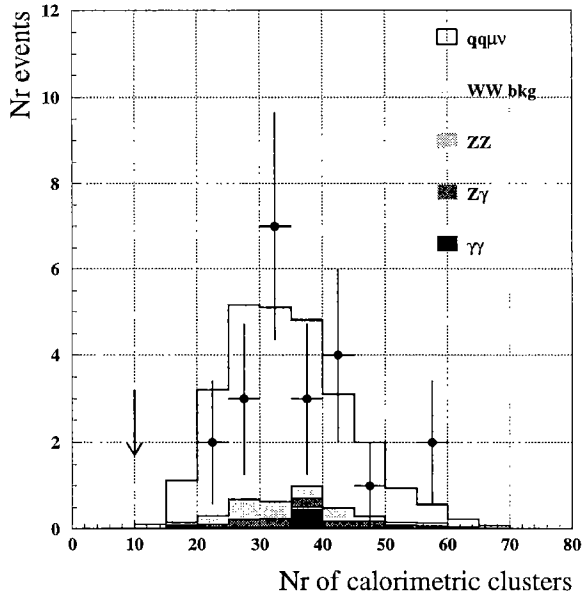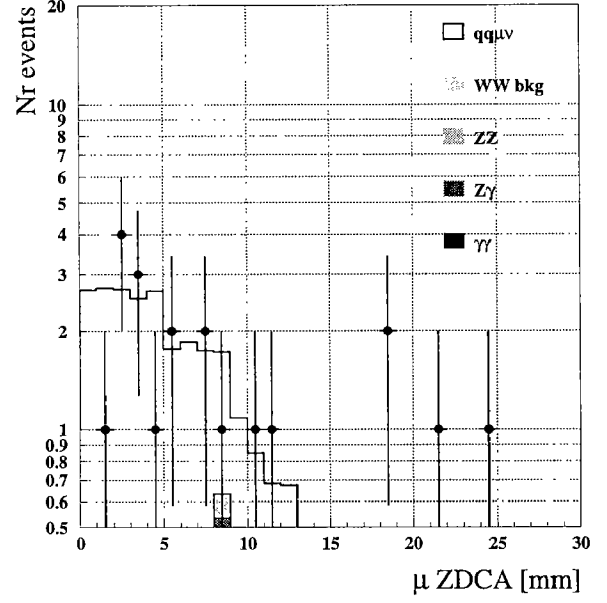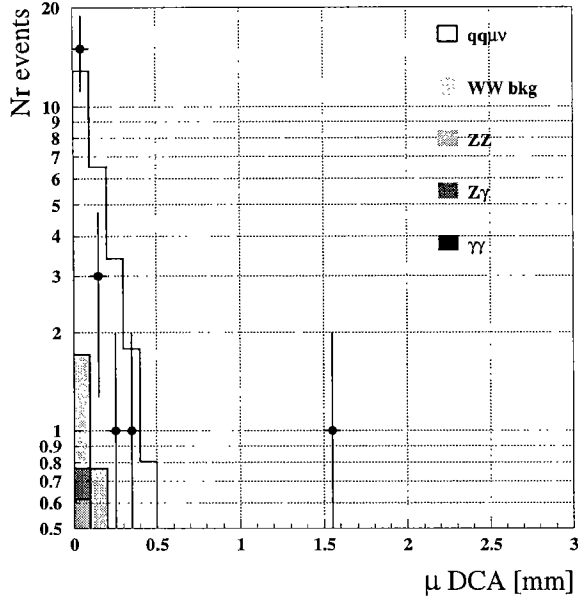
Figure 5.12: Distributions of event parameters on which cuts were imposed at $\sqrt{s} = 189$ GeV in the MIP selection. Dots represent data events. For every histogramm, all other cuts apart from the one displayed are applied. Values at which the cuts were set are indicated by arrows. No implicit cuts were applied in the selection on the DCA ans ZDCA of the MIPs.
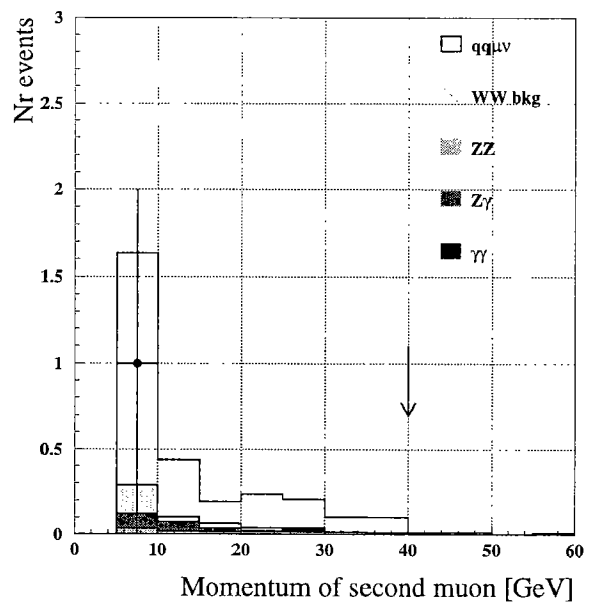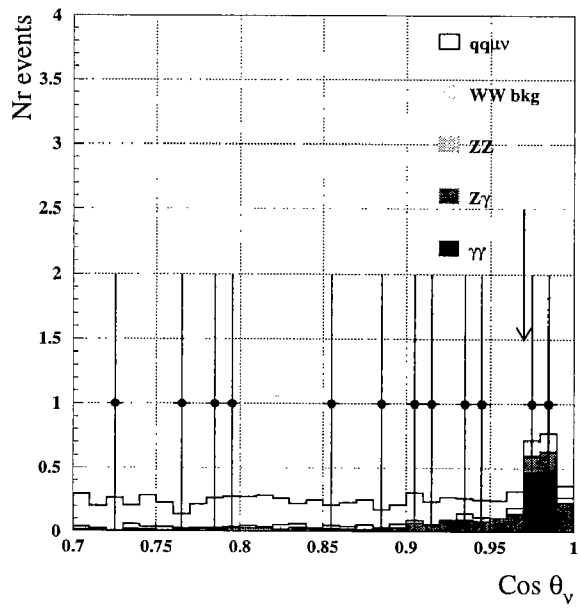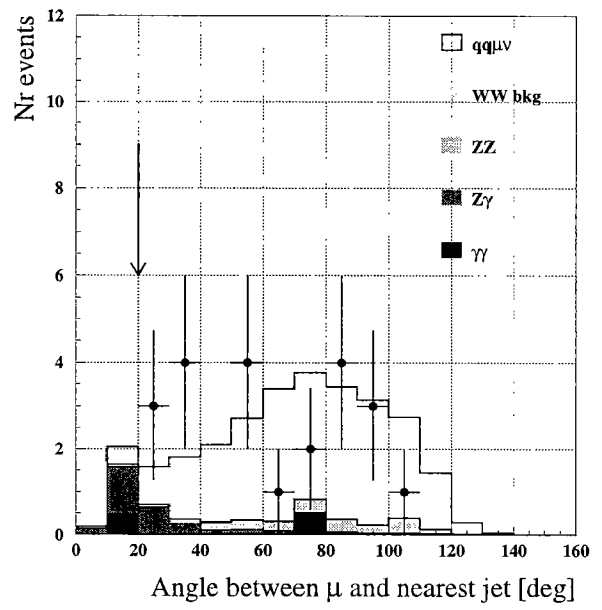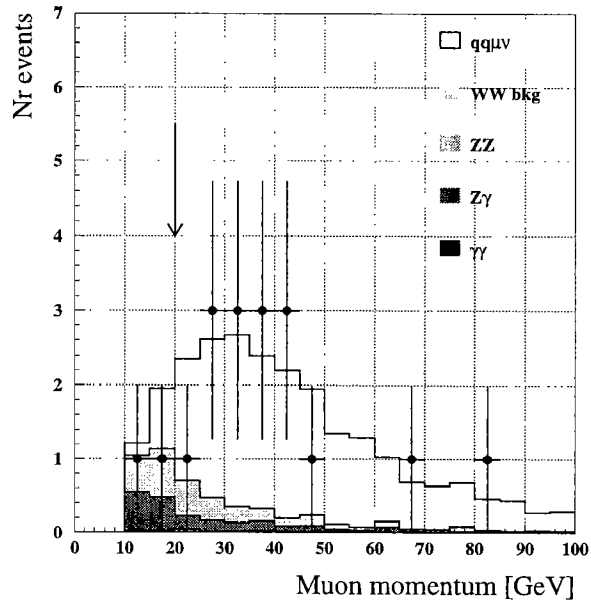
Figure 5.13: Distributions of event parameters on which cuts were imposed at $\sqrt{s} = 189$ GeV in the MIP selection. Dots represent data events. For every histogramm, all other cuts apart from the one displayed are applied. Values at which the cuts were set are indicated by arrows.
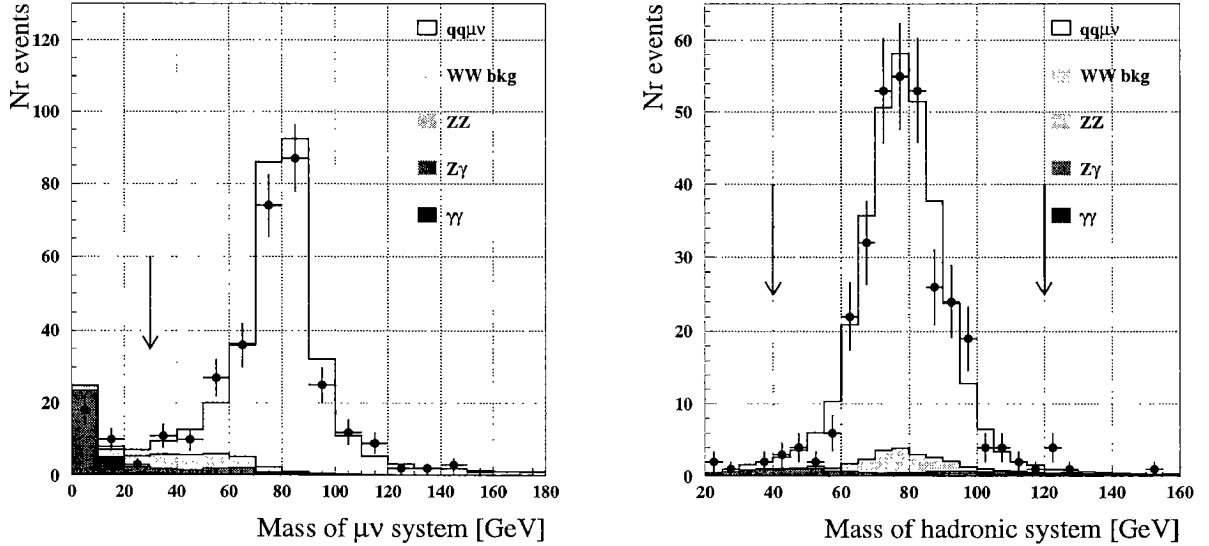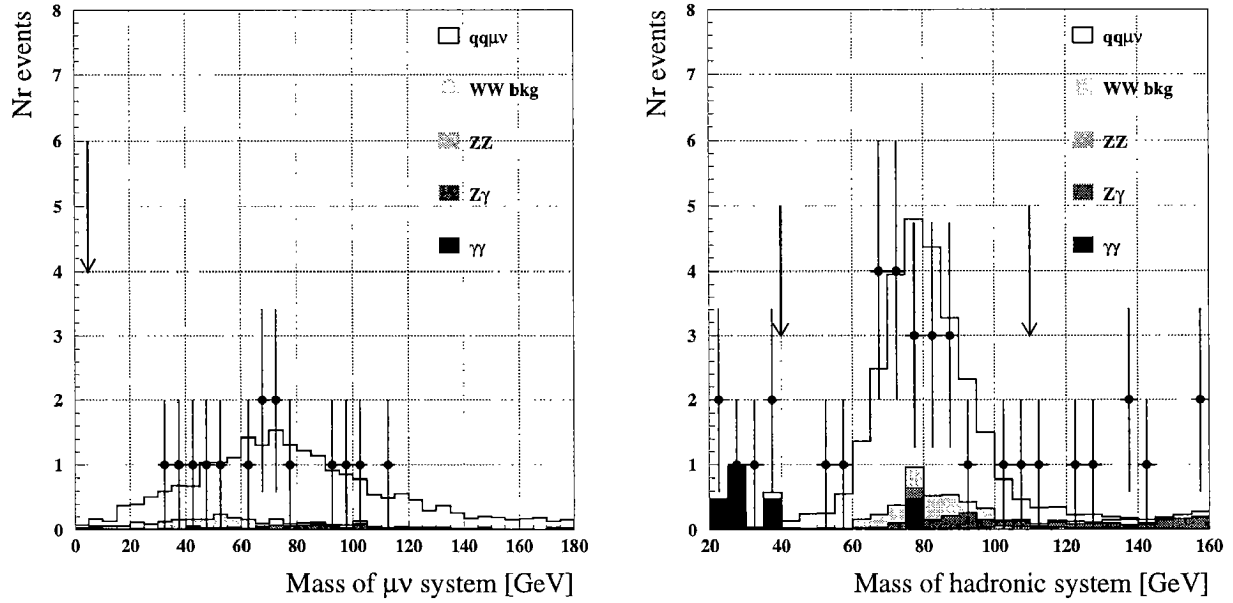
Figure 5.14: Distributions of event parameters on which cuts were imposed at $\sqrt{s} = 189$ GeV in the MIP selection. Dots represent data events. For every histogramm, all other cuts apart from the one displayed are applied. Values at which the cuts were set are indicated by arrows.

Cut variable	Muon Detector	MIP
Muon DCA	0.05%	0.0%
Muon ZDCA	0.0%	0.0%
Nr of clusters	0.2%	0.0%
Nr of tracks	0.5%	0.1%
Muon momentum	0.4%	2.0%
Angle(muon,jet)	0.5%	1.0%
Mass of jet system, lower cut	0.2%	1.0%
Mass of jet system, upper cut	0.2%	0.5%
Mass of $\mu\nu$ system	0.2%	0.5%
|Cos(polar angle of missing momentum)|	0.7%	2.0%
Secondary muon momentum	0.1%	0.5%
Total	**1.15%**	**3.28%**
Total for combined selection	**1.41%**	

Table 5.8: Systematic error from cut variation at $\sqrt{s} = 189$ GeV.
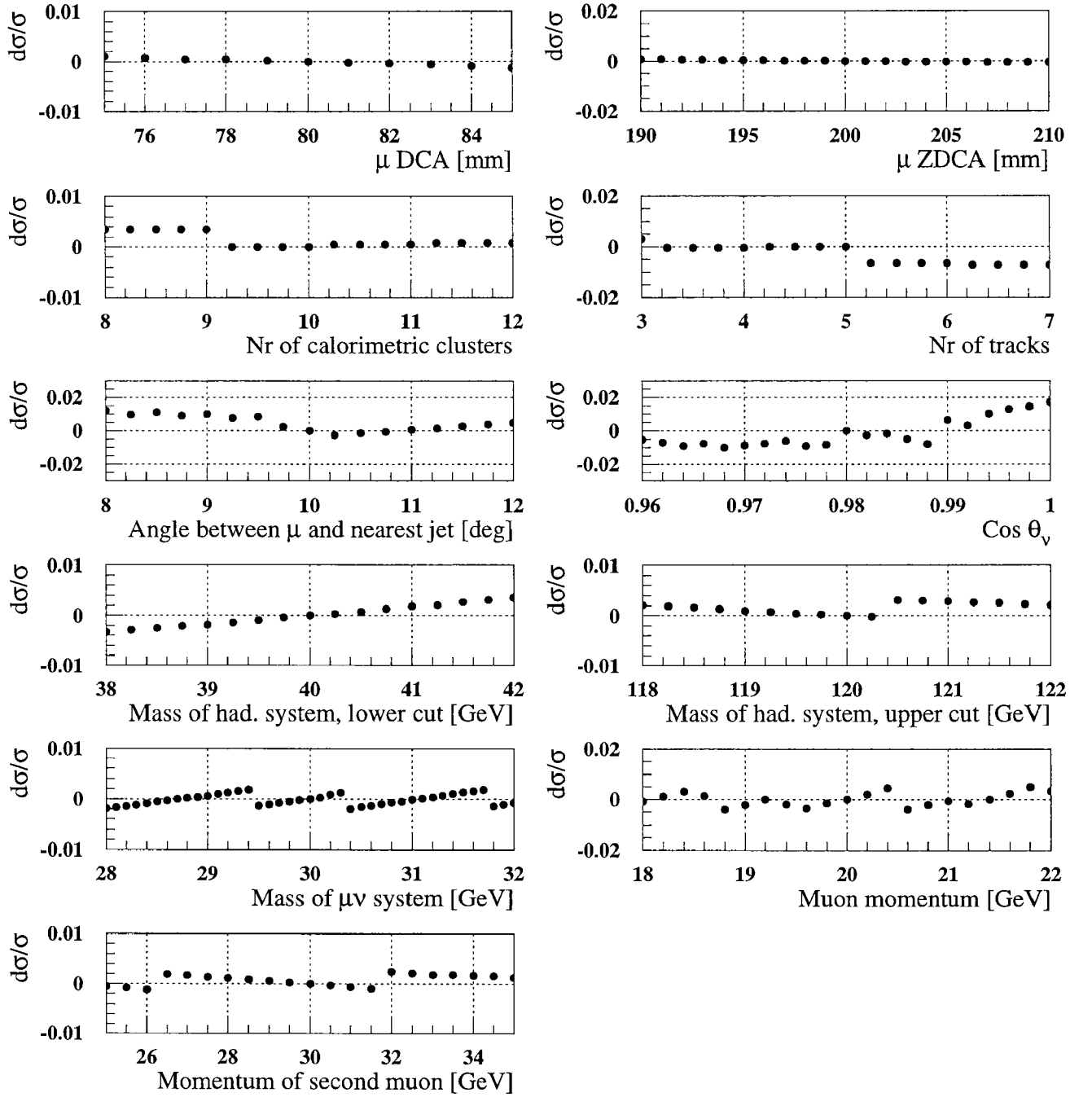
Figure 5.15: Relative change in measured cross section due to variation of cut position, for the cuts imposed at $\sqrt{s}$ = 189 GeV for muons identified due to their signature in the muon chambers.
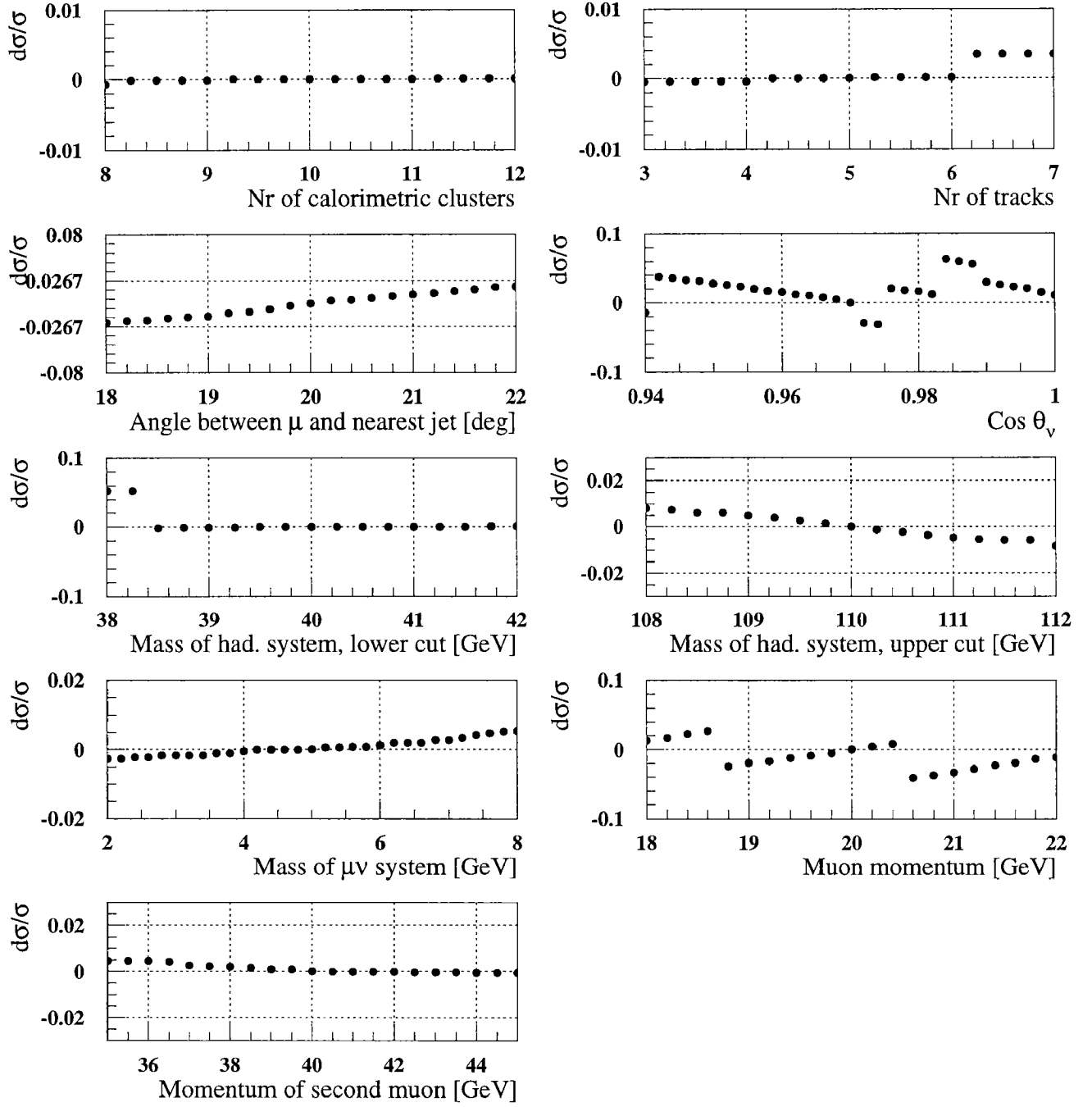
Figure 5.16: Relative change in measured cross section due to variation of cut position, for the cuts imposed at $\sqrt{s} = 189$ GeV for muons identified as MIP.

Chapter 6

W Mass Measurement

Three methods have been proposed for a measurement of the W boson mass using W pair events at LEP2 [49]:

- Near the W pair production threshold, the WW cross section depends strongly on the W mass. By measuring σ_{WW} in the threshold region, M_W can be extracted. This indirect method relies of course on the Standard Model calculation of the WW cross section. The optimal centre-of-mass energy was evaluated to be $\sqrt{s} \approx 2M_W + 0.5\text{GeV}$. With the then world average value of $M_W = 80.26 \pm 0.16\text{GeV}$, the first LEP2 energy in 1996 was therefore chosen to be $\sqrt{s} = 161\text{GeV}$, where 11 pb^{-1} was collected by L3. The W boson mass was measured to be $80.80^{+0.48}_{-0.42}$ GeV [50].

- Above the threshold energy, the end-points of the lepton energy spectrum from W decay can be used to measure the W mass. For on-shell W bosons the energy W decay products is in the range $E_- \leq E_l \leq E_+$, with

$$E_\pm = \frac{\sqrt{s}}{4}(1 \pm \sqrt{1 - 4M_W^2/s}),$$

and from the measurement of $E_\pm$, the W boson mass can be extracted. The end-points get smeared, however, by finite W width, initial state radiation and detector effects. In this way, the method looses much of it's statistical power, and was therefore used only for cross-checks and M_W measurement in the fully leptonic channel [51].

- The most effective method for M_W determination above the W pair production threshold, where most of the LEP2 data was collected, relies on a fit to the distribution of the invariant W mass calculated from its decay products. Detector and selection effects, as well as physics related effects such as initial state radiation, Bose-Einstein correlations and Colour Reconnection can be taken into account by means of various techniques such as Monte Carlo calibration, convolution or the reweighting method. This direct reconstruction method was described in much detail in Ref. [49].

6.1 The Method of Best Measured Kinematic Variables

Most of the methods described above are using quantities which are not directly measured in the detector, but rather deduced from other event parameters. A method using measured variables with the best resolution given by the experimental device was proposed by

Berends et al. [53], [54]. The set of variables, $\{\Psi\}$ will vary depending on the considered final state, and can also depend on detector parameters. For a particular final state j, the probability $\mathcal{P}$ of observing the set of values $\{\Psi_i\}$ is first calculated on an event-by-event basis as function of M_W:

$$\mathcal{P}_j(\{\Psi_i\}, M_W) = \frac{1}{\sigma_j^{tot}} \frac{d\sigma_j(\{\Psi_i\}, M_W)}{d\{\Psi_i\}}, \tag{6.1}$$

with σ_j^{tot} being the total cross section for the channel under consideration. The log likelihood function for this channel, with N_j selected events, is then

$$\log\mathcal{L} = \sum_{i=1}^{N_j} \log\left(\frac{d\sigma_j}{d\{\Psi_i\}}\right) - N_j \log\sigma_j^{tot}. \tag{6.2}$$

In order to determine the mass of the W using all selected WW events, the total log likelihood function is calculated to be the sum of the likelihood functions in all the decay channels. A fit to minimize $-\log\mathcal{L}$ gives then an estimator for M_W, with the one standard deviation error calculated from the interval limits

$$\log\mathcal{L} = \log\mathcal{L}_{\min} + \frac{1}{2}. \tag{6.3}$$

The calculation of the differential cross section proceeds in two steps: first the energy fraction (x_1, x_2) left to $e^{\pm}$ after initial state radiation is generated and the kernel (non-radiative) cross section $\frac{d\bar{\sigma}_j(x_1,x_2)}{d\{\Psi\}}$ is calculated as function of the invariant amplitude $|\mathcal{M}|^2$. This kernel cross section has to be convoluted with the ISR structure functions $\Phi(x)$

$$\frac{d\tilde{\sigma}_j}{d\{\Psi\}} = \int_0^1 \int_0^1 \frac{d\bar{\sigma}_j(x_1, x_2)}{d\{\Psi\}} \Phi(x_1)\Phi(x_2) dx_1 dx_2 \tag{6.4}$$

in order to obtain the differential cross section after ISR. Analytical expressions for $\frac{d\bar{\sigma}_j(x_1,x_2)}{d\{\Psi\}}$ were calculated by the authors of the method in Ref. [54]. To obtain the results shown here, the calculations of $|\mathcal{M}|^2$ was performed using the core code of EXCALIBUR [55].

The calculations are based on the following choice of parameters:

- **fully hadronic case:** $\{\Psi\} = \{\theta_1^{jet}, \phi_1^{jet}, \theta_2^{jet}, \phi_2^{jet}, \theta_3^{jet}, \phi_3^{jet}, \theta_4^{jet}, \phi_4^{jet}\}$

- **semileptonic case:** $\{\Psi\} = \{E_l, \theta_l, \phi_l, \theta_1^{jet}, \phi_1^{jet}, \theta_2^{jet}, \phi_2^{jet}, E_{hadrons}^{tot}\}$

- **fully leptonic case:** $\{\Psi\} = \{E_1^l, \theta_1^l, \phi_1^l, E_2^l, \theta_2^l, \phi_2^l\}$. Here, since without ISR eight parameters are needed to completely determine the kinematics of an event, an integration over the two neutrino energies has to be performed.

Due to missing assignment of jets to a particular quark flavour, summing over all possible quark combinations is performed in the channels with jets in the final state.

The feasibility of the method was demonstrated in Ref. [53]. The log likelihood distribution with a fitted quadratic function is shown in Fig. 6.1 for a sample of 17000 qqqq events generated using KORALW event generator with an input W mass of 80.75GeV. The log likelihood function is very well described by the second order polynomial, as is expected from the central limit theorem. In the work presented here, also the linearity with respect to the W mass
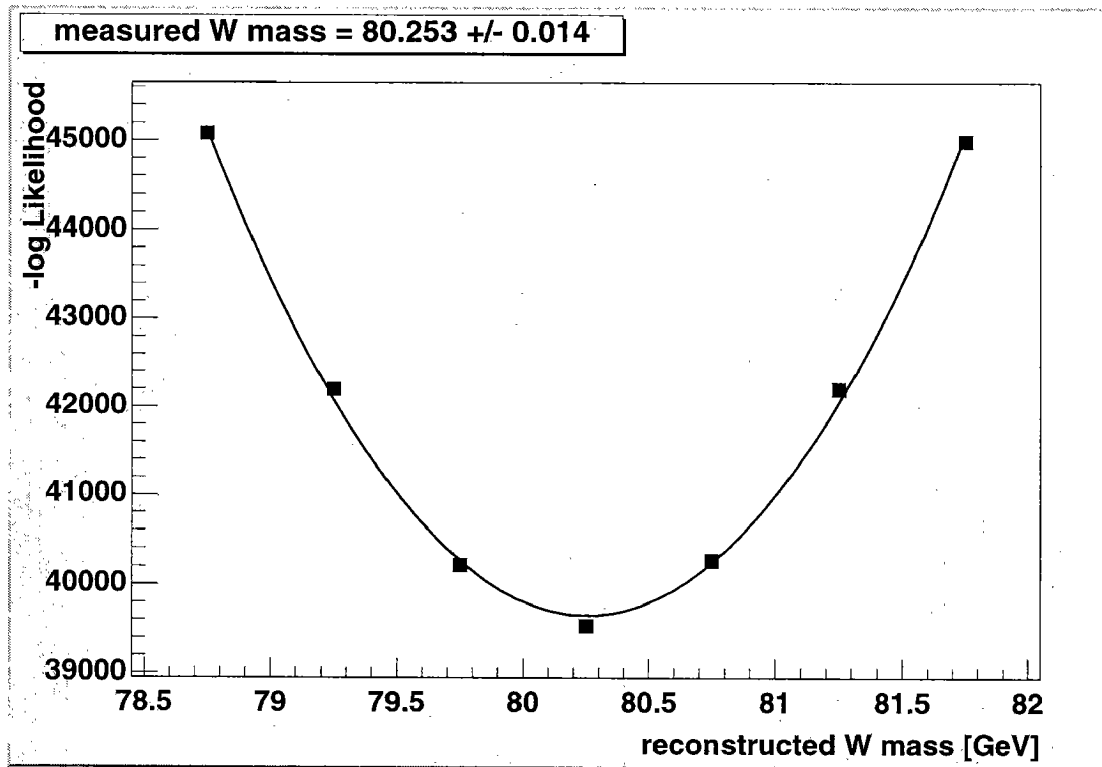
Figure 6.1: Log likelihood function fit for a large sample of qqqq events generated with a W mass of 80.25GeV. The minimum of $-\log \mathcal{L}$ is found for $M_W = 80.253$ GeV, with a statistical accuracy of ± 0.014 GeV.

M_W^{gen}	qqeν	qq$\mu\nu$	qq$\tau\nu$	qqqq
80.0	79.99 ± 0.02	80.03 ± 0.02	80.01 ± 0.02	80.01 ± 0.01
80.25	80.23 ± 0.02	80.27 ± 0.02	80.26 ± 0.02	80.25 ± 0.01
80.5	80.48 ± 0.02	80.51 ± 0.02	80.50 ± 0.02	80.50 ± 0.01
80.75	80.69 ± 0.02	80.75 ± 0.02	80.75 ± 0.02	80.74 ± 0.02
81.0	80.96 ± 0.02	81.02 ± 0.02	81.01 ± 0.02	81.00 ± 0.02

Table 6.1: Reconstructed W mass for different generated W masses at generator level. Calculations for charge conjugate states are combined for semileptonic final states. 6600 events in each semileptonic channel and 17000 qqqq events were used in the calculation.

was studied. Table 6.1 summarizes all the numerical results for calculations performed at generator level with Monte Carlo samples generated with KORALW with five different W masses: $M_W = \{80.0, 80.25, 80.5, 80.75, 81.0\}$. CC03 diagrams were used for all final states but qqeν, where a CC20 calculation was performed. The method is clearly linear and bias free within errors in all channels at generator level.

It should be noted here that while KORALW is generating initial state radiation photons emitted with a component transverse to the beam direction, EXCALIBUR calculations are carried out with ISR radiation only along the incoming (beam) particles. The very good agreement between reconstructed and generated W mass demonstrates also the validity of this approximation in the framework of this study.

6.2 Detector Effects

The effects of the detector are included by convolution. Given $\frac{d\tilde{\sigma}}{d\{\Psi\}}$ on generator level, the differential cross section at detector level reads

$$\frac{d\sigma(\{\Psi_j\})}{d\{\Psi\}} = \int d\{\Psi'_j\} \mathcal{R}(\{\Psi'_j\}, \{\Psi_j\}) \frac{d\tilde{\sigma}(\{\Psi'_j\})}{d\{\Psi\}}. \tag{6.5}$$

The resolution function $\mathcal{R}$ can be interpreted as the probability of reconstructing the parameter set $\{\Psi_j\}$, given that the true event parameters are $\{\Psi'_j\}$. As a first approximation, one can assume that the measurement of the variables in the parameter sets given in Sec. 6.1 is uncorrelated, and therefore the N-dimensional resolution function (with N=6 for fully leptonic final state, and N=8 for all other channels) factorizes into N one-dimensional resoluton functions. In order to obtain these resolution functions, a large Monte Carlo sample was used, where events are reconstructed with full detector simulation using the same calibration parameters as used in data reconstruction. This so called real detector simulation (c.f. Sec. 2.4) also takes time dependent effects into account, like e.g. muon chamber cells that had to be disconnected during the run period. The relative difference between the reconstructed and generated values was then fitted with a Gaussian, or where necessary with a double Gaussian function. All used resolution plots are shown in App. E.1.

In the qq$\mu\nu$ channel, six classes of muons have been considered, according to the different precision of measurement of their parameters: triplets, doublets, doublets with forward/backward chamber hit, singlet with forward/backward chamber hit, muons with only forward/backward chamber hits and MIPs. In the qqeν channel, the electron resolution differs for electrons detected in the calorimeters and in the EGAP detector, the latter one not being

used in this analysis due to poor energy and angular resolution. The qqτν channel has been clasified according to the τ decay mode: $τ \to μ$, $τ \to e$, and $τ \to$ hadrons. This channel poses more difficulties, since the measured phase space angles of the visible decay products are not the true τ parameters, due to missing energy carried away by the neutrinos. The net effect on the azimutal and polar angles is just a loss in resolution, while the energy is always lower for the visible decay products than the τ energy. In order to account for this effect, a constrained fit was applied, assuming the measured polar and azimutal angles to be the true τ production angles, and using the τ mass as well as a zero mass constraint on the neutrinos [56]. This results in unbiased measurement of τ energy, as can be seen in Fig. E.7, but still, as will be shown further below, a loss in sensitivity on the M_W can be seen.

Turning to the possible correlations between the measured quantities, one would expect, if any, the strongest ones to be between the muon momentum and its polar angle, as well as between the polar and azimutal angles of the two jets. However, the estimated correlation matrix in the qqμν channel given in Tab. 6.2 shows that all correlations are well below 10% and demonstrates the validity of the approximation of uncorrelated errors. The small correlation

	$E_μ$	$θ_μ$	$φ_μ$	$θ_{jet}$	$φ_{jet}$	E_{had}
$E_μ$	1.0	0.013	0.003	-0.006	-0.026	-0.008
$θ_μ$	0.013	1.0	-0.013	0.059	-0.028	-0.001
$φ_μ$	0.003	-0.013	1.0	0.007	-0.001	-0.002
$θ_{jet}$	-0.006	0.059	0.007	1.0	0.002	-0.009
$φ_{jet}$	-0.026	-0.028	-0.001	0.002	1.0	0.003
E_{had}	-0.008	-0.001	-0.002	-0.009	0.003	1.0

Table 6.2: Correlation matrix of the errors on variables used in the W mass calculation in the qqμν channel determined on a large Monte Carlo sample. The matrix is reduced to 6 variables by combining the space angles of the two jets.

coefficients show also that indeed the variables used in the calculation are chosen in an optimal way, as far as the experimental measurement is concerned.

The distibutions of the kinematical variables used in the mass calculation was checked between data and the MC sample with full detector simulation. The very good agreement, as shown in the plots in App. E.2, can be accepted as a confirmation of the correctness of the real detector simulation, and demonstrates the validity of the predictions obtained with the Monte Carlo studies.

The convolution is performed using a Monte Carlo integration technique, which is described in App. C. In the semileptonic and fully hadronic final states, the integration must be performed over the 8 kinematical variables measured, plus the integration over the initial state radiation spectrum, giving additional two integrations. In the fully leptonic channels, one has only 6 measured parameters - the momenta and the azimutal and polar angles of the two leptons. This makes two additional integrations over the energy spectra of the two unmeasured neutrinos necessary. Therefore, in all the final states, the resulting convolution integral is 10-dimensional.

6.3 Calibration and Expected Errors

Five different real detector Monte Carlo samples generated with $M_W = \{80.0, 80.25, 80.5, 80.75, 81.0\}$ were used to determine the linearity of the calculation with convolution of detector effects. The

resulting linearity plots for the semileptonic and fully hadronic channels are shown in Fig. 6.2, together with a fitted first order polynomial. In all three cases, the reconstructed mass is linear with respect to the generated mass; in the $qqe\nu$ and $qq\mu\nu$ channels, the slope is consistent with unity, while in the $qq\tau\nu$ channel, the loss of sensitivity due to the presence of unmeasured neutrinos in τ decay results in a flatter curve.
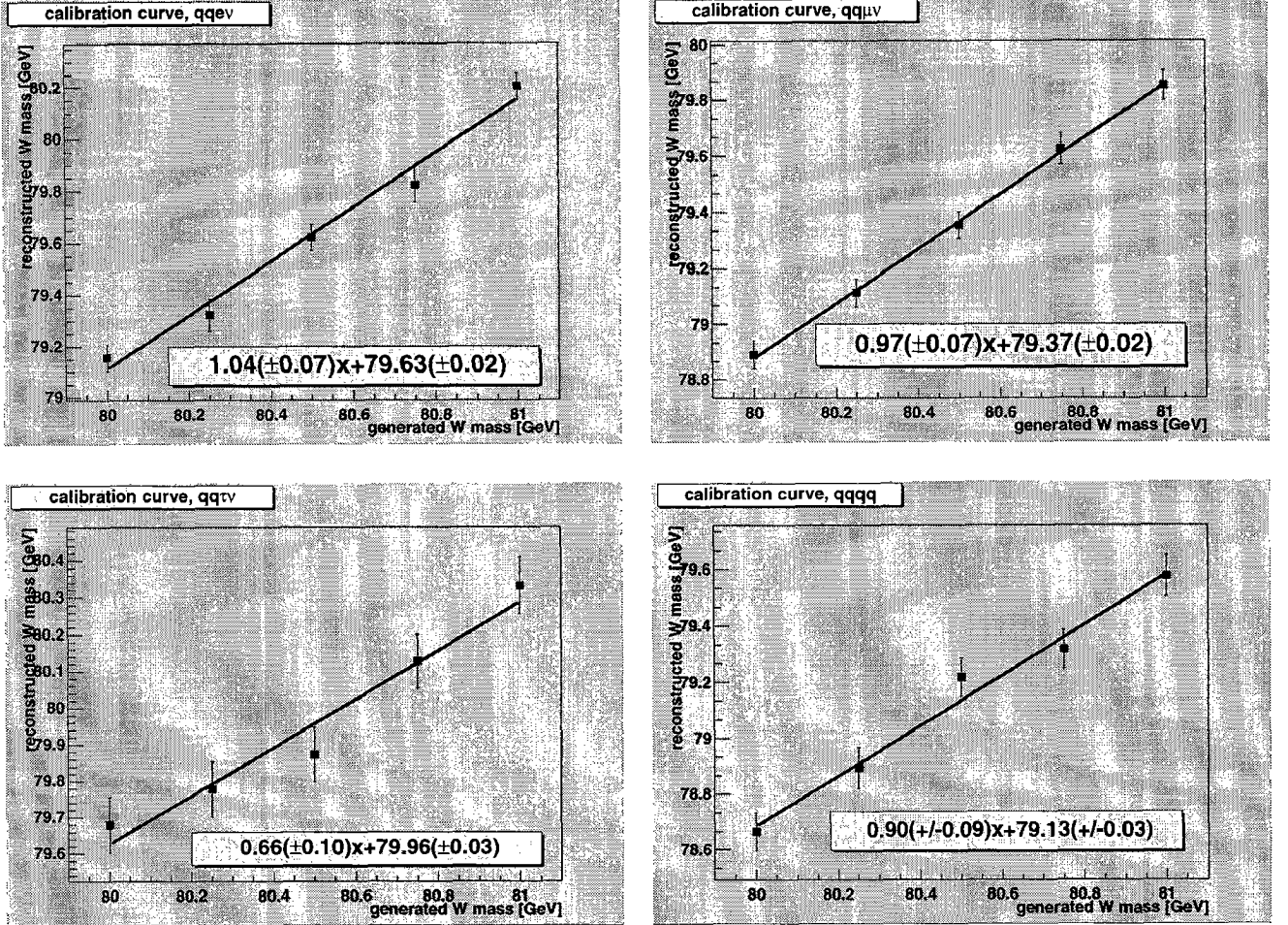
Figure 6.2: Calibration curve for the $qqe\nu$ (top-left), $qq\mu\nu$ (top-right) $qq\tau\nu$ (bottom-left) and $qqqq$ (bottom-right) channels. In the semileptonic channels, charge conjugate states are combined. The points represent the reconstructed mass for five different generated masses. All detector effects have been taken into account.

The reference point of the fitted function was moved to $M_W = 80.5$ GeV. The observed shift of $\sim 0.5 - 1$ GeV is a result of the missing information about the masses of the particles forming the jets. The jet clustering algorithm assumes the particles to be massless, which results in the jets appearing to be closer together than the generated quarks. In Fig. 6.3, the angle between the jets is plotted at generator level, i.e. the angle in the laboratory frame between the two quarks, as well as the angle at detector level. The mean of the distribution is shifted towards lower angles, meaning higher boost of the W boson, corresponding to a shift of the W mass to a lower value. The data distribution follows the Monte Carlo distribution at detector level. Since data and simulation agree very well, the fitted calibration curve can be used to correct for this effect. This is a simple and working correction method, which is necessary, since no quark
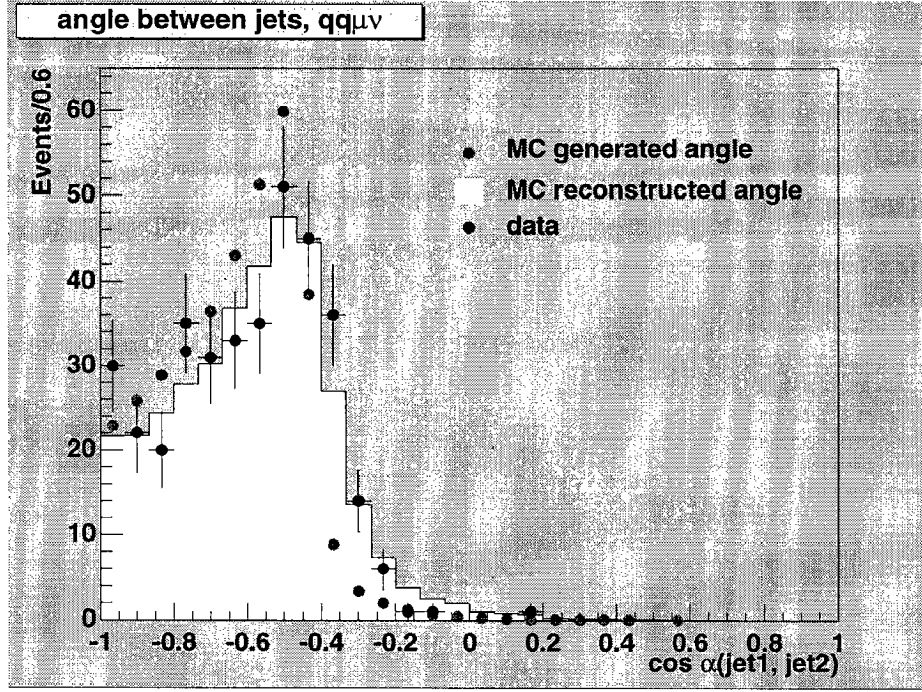
Figure 6.3: The cosine of the angle between the jets, for Monte Carlo events and data collected at $\sqrt{s} = 189$ GeV. The Monte Carlo distributions are scaled to the corresponding data luminosity.
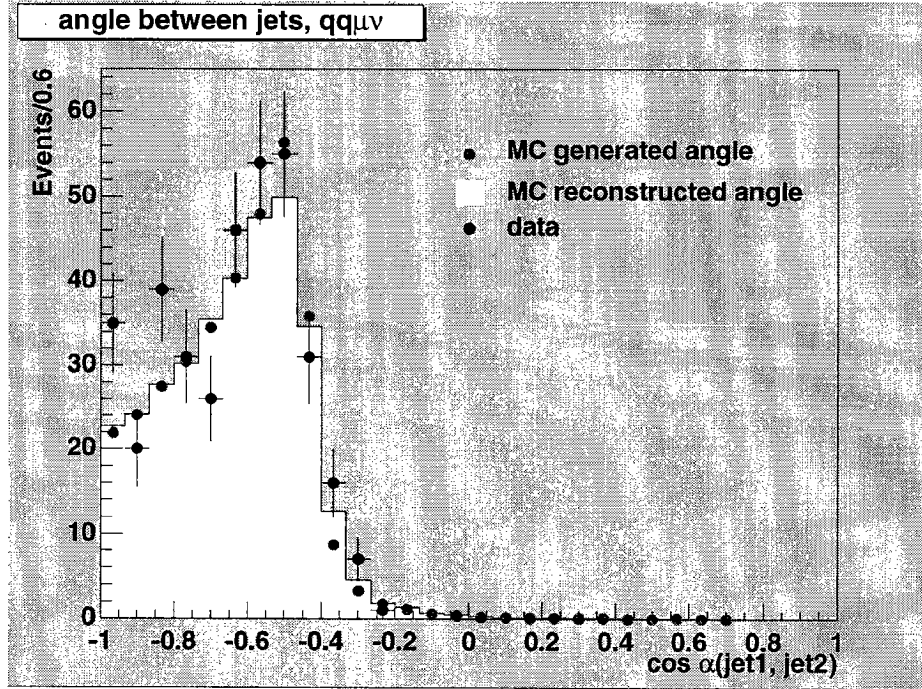
Figure 6.4: The cosine of the angle between the jets, for Monte Carlo events and data collected at $\sqrt{s} = 189$ GeV, after applying the quark mass correction. The Monte Carlo distributions are scaled to the corresponding data luminosity.

flavour determination is performed for the jets, and therefore the proper mass of the generated particle is not known.

A way of taking this effect into account is to boost the jets to the W reference frame, set the masses of the jets to the identified quark masses, and boost them back to the laboratory frame. This method restores the original angle between the quarks from W decay, as can be seen in Fig. 6.4. In this plot, the data distribution was obtained by assuming the quarks to be massless. Indeed, a test performed in the $qq\mu\nu$ channel has shown that the bias has disappeared. This method of correction cannot be applied to the fully hadronic final state, since the parent W boson is not known for the jets. Unfortunately, calibration has still to be performed in this channel, as well as in the $qq\tau\nu$ final state, where the loss of sensitivity needs to be accounted for.

The expected statistical error was evaluated using simulated samples corresponding to the number of selected events in each channel. For this purpose a Monte Carlo simulation with generated $M_W = 80.5$ GeV, and independent of the calibration samples, was used. The mass and calculated statistical error distributions are shown in Fig. 6.5. After applying the corrections discussed above, no bias is observed, and, most important, the mean calculated error of each sample corresponds to the width of the mass distribution. The error is thus correctly estimated.

6.4 W Mass Measurement at $\sqrt{s} = 189$ GeV

The method was applied to the data collected by L3 at $\sqrt{s} = 189$ GeV. Using the selection procedure as described in Chapter 4, the data sample consisted of 352 $qqe\nu$, 364 $qq\mu\nu$, 313 $qq\tau\nu$ and 2674 $qqqq$ events.

The log likelihood functions calculated for the selected data events are shown in Fig. 6.6, together with the fitted minimum and the calculated W mass after calibration. The first error shown is the statistical uncertainty, while the second one is the systematic error arising from the uncertainty on the parameters of the calibration function. No other sources of systematic uncertainty were taken into account in this calculation.

The errors obtained agree very well with the expected statistical errors in all channels. The results are combined for all semileptonic and fully hadronic decay channels, resulting in a measured W mass of

$$M_W = 80.45 \pm 0.10(stat.) \text{ GeV}$$

and are summarized in Tab. 6.3.

The results quoted above agree very well with the results obtained using the standard L3 measurement of M_W (convolution method using event counting technique [57] [58]). Comparing only statistical errors, the same sensitivity is obtained in the fully hadronic final state, while in the semileptonic channels the errors are larger by $\sim 20\%$ using the method of best measured kinematical variables. Since the $qqqq$ channel represents by far the highest statistics, the combined result in all final states shows nearly the same sensitivity as the standard L3 method, with the preliminary statistical error from the $\sqrt{s} = 189$ GeV data [59].

The method presented here can be further improved:

70
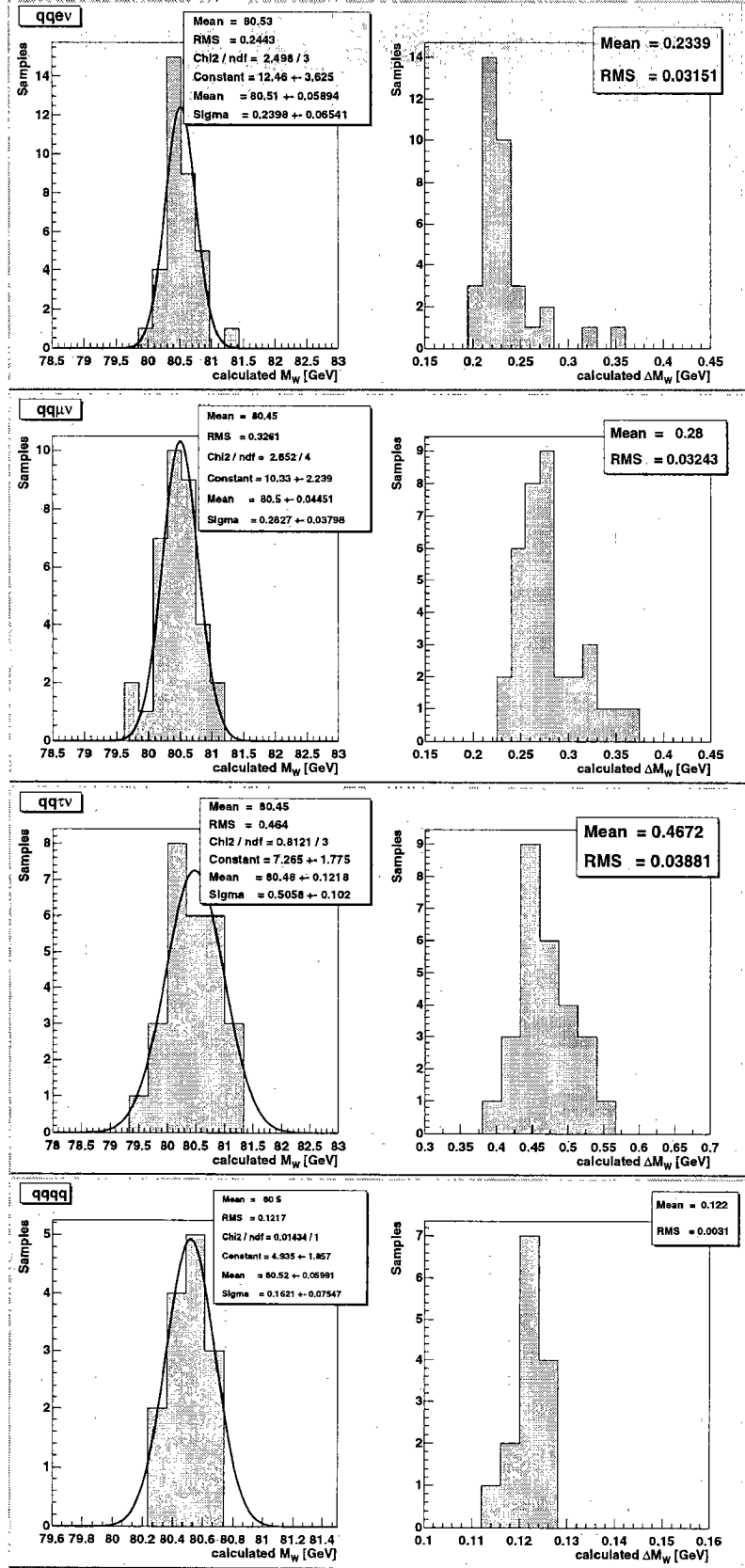
Figure 6.5: Expected error of the calculation in qqeν, qq$\mu\nu$, qq$\tau\nu$ and in qqqq channel (top to bottom). For each channel, the calculated mass for each sample is ploted on the left, with the estimated error on the right. All samples were generated at $M_W = 80.5$ GeV.
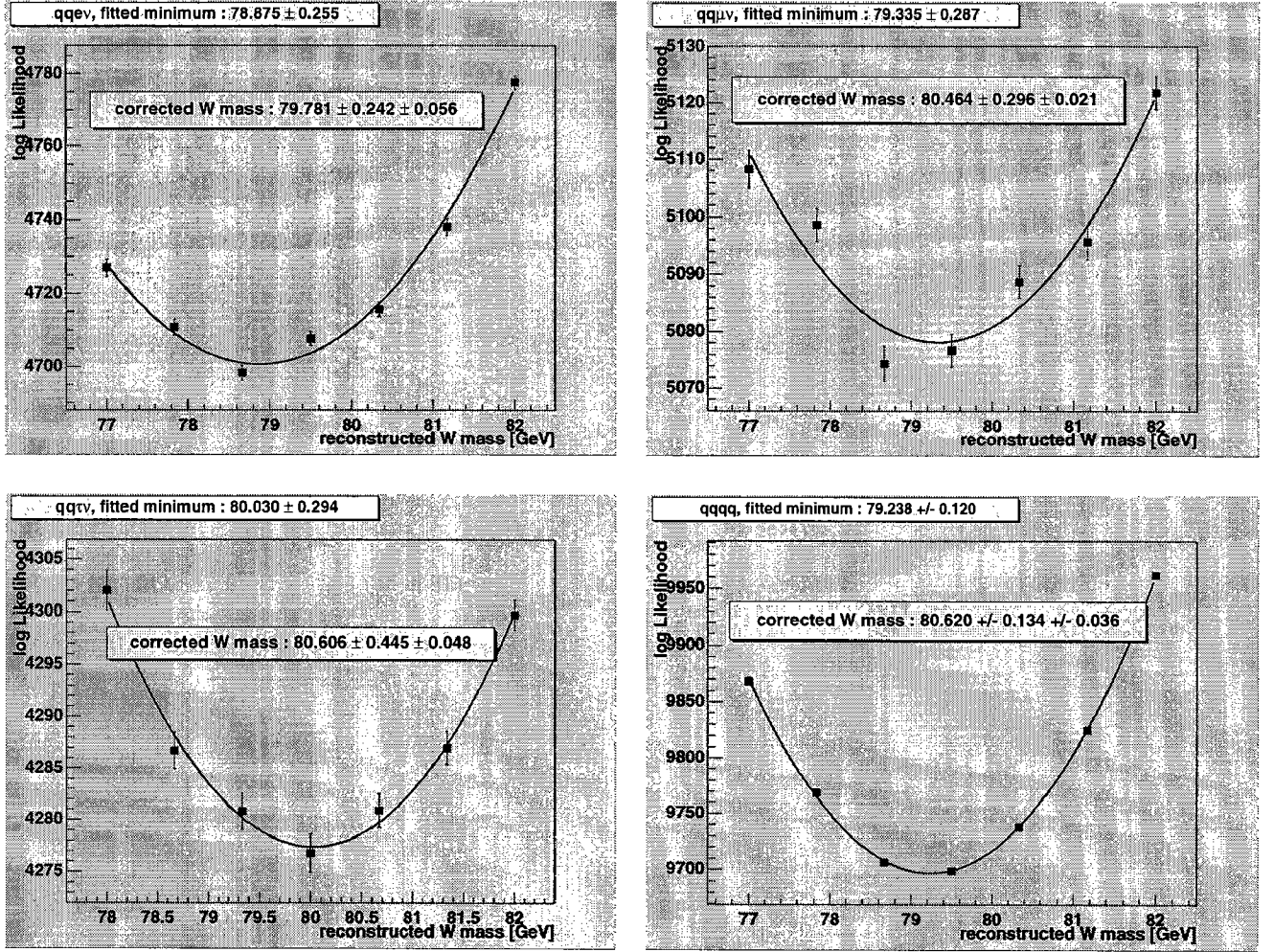
Figure 6.6: Log likelihood distribution for selected data events at $\sqrt{s} = 189$ GeV. Shown are the qqeν (top-left), qq$\mu\nu$ (top-right), qq$\tau\nu$ (bottom-left) and qqqq channel (bottom-right). Charge conjugate final states are combined in the semileptonic channels. The second error given is the systematic error arising from the uncertainty on the parameters of the calibration function.

- In the qq$\tau\nu$ channel, the slope of the calibration curve being very different from one, the corrected error becomes much larger than just the error on the fitted value. This could be avoided by additional integration over the spectrum of the ν_τ.

- For the convolution with ISR and detector effects, 25000 iterations were used in the semileptonic final states, and 20000 in the hadronic case. A higher number of iterations could possibly result in a better fit, but the price to pay will of course be higher CPU time consumption.

- The $|\mathcal{M}|^2$ calculation taken from EXCALIBUR ignores fermion masses. The ISR photons are taken to be strictly collinear with incoming beam particles. A new code from same authors, NEXTCALIBUR [60], includes fermion masses, as well as non-vanishing p_t spectrum of radiated photons. These two features could lead to improved W mass measurement.

72

WW decay channel	measured M_W [GeV]
WW $\rightarrow$ qqeν	79.78 $\pm$ 0.24
WW $\rightarrow$ qq$\mu\nu$	80.46 $\pm$ 0.30
WW $\rightarrow$ qq$\tau\nu$	80.61 $\pm$ 0.45
WW $\rightarrow$ qqlν	80.13 $\pm$ 0.17
WW $\rightarrow$ qqqq	80.62 $\pm$ 0.13
WW $\rightarrow$ ffff	80.44 $\pm$ 0.10

Table 6.3: W boson mass obtained in each channel, combined measurement in semileptonic channels, as well as all final states combined. The error quoted is statistical only. Data collected at $\sqrt{s} = 189$ GeV was used.

- In rare cases, the ISR photons have enough p_t to be registered in the detector. Taking an identified photon into account could also lead to small improvement.

- The lνlν final state was not considered so far. Even if not statistically significant, the addition of this channel would of course result in a decrease of statistical error on the W mass measurement.

The method presented here, although simple in nature, proved very powerful. The implementation in experimental environment was very straight forward, with encouraging first results. Nevertheless, two problems could be singled out: the differential cross section, calculated on event by event basis, shows quite unstable behaviour, with the weight of the event varying sometimes very strongly within a small change of parameters. This is also the case on generator level. Obviously, since the method is of statistical nature, the problem arises due to limited number of events - the log likehood curve in the qqqq channel is clearly free of instabilities which can be seen in the much less populated semileptonic final states.

Here, unfortunately, the second problem prevents us from the obvious improvement: were the measurements in the sub-channels bias free, one could simply combine the likelihood functions to one, and perform a single maximum likelihood fit for all data. A flavour tagging of the jets would be necessary and sufficent in order to correct for this effect in the semileptonic channels. For fully hadronic events, one would still need to know the proper combination of jets and the parent Ws.

6.5 Systematic Effects

The application of the calibration corrections introduces additional uncertainty on the measurement. The statistical error on the fitted parameters of the calibration curve propagate into the results obtained in the fit to the likelihood function. These errors, however, depend only on the statistics of the Monte Carlo samples used to obtain the calibration curve, and not on the data statistics itself. It is therefore sensible to quote these errors as a contribution to the systematic error on the W mass measurement. The calculation of these errors is given in App. B.

Table 6.5 summarizes the main sources of systematic uncertainty. Evidently, the highest contributions arise in the fully hadronic channel, where interconnection effects between quarks originating from different Ws can occur.

Two quarks originating from the same W boson form a colour singlet, and can be expected to hadronize independently from the hadronization process of the quarks from the other W.

Source	$\Delta M_W^{syst}(\mathrm{qql}\nu)$ [MeV]	$\Delta M_W^{syst}(\mathrm{qqqq})$ [MeV]
Fitting Method	40	35
Resolution Parameters	20	20
LEP Energy	20	20
Fragmentation	15	54
Bose-Einstein	-	38
Colour Reconnection	-	37
Total	51	88

Table 6.4: Main sources of systematic uncertainty on the M_W measurement, with their contribution to the error on the measurement in the semileptonic and fully hadronic final states.

Nevertheless, two quarks from different Ws can also form a colour singlet with a probablity of $1/N_c^2 = 1/9$. Due to the short lifetime of the W boson, and therefore short space-time distance between the decay points, gluon exchange may take place between quarks from different Ws. This effect, called Colour Reconnection [61, 62], may influence the jet shapes and therefore also the measurement of the W mass. Two models have been studied, in order to estimate the impact of Colour Reconnection on M_W: superconductor model type I and type II, as implemented in PYTHIA 5.7 [63].

Also Bose-Einstein [64, 65] effects can influence the mass reconstruction. A recent study performed by L3 [66] shows evidence for correlations between particles of a single W, with good agreement with results obtained investigating light quark decays of the Z boson. It disfavours strongly the existence of Bose-Einstein correlations between particles from different Ws. Two algorightms, as implemented in KORALW: BE_{32} and BE_0 [67] were also compared with data. The much better agreement of BE_{32} with the data sample is used as an argument for a bias correction on the measured W boson mass. The base line Monte Carlo samples, used for the calculation of the calibration curve are all generated using the disfavoured BE_0 algorithm. Comparison of two large statistics Monte Carlo samples generated with the two algorithms gives a shift of -126 ± 38 MeV on the measurement in the hadronic channel. This bias is added to the measured mass in this final state, with the error included in the systematic error on the mass measurement.

Fragmentation and decay models are studied by comparing signal events simulated using string fragmentation as implemented in PYTHIA [68] and cluster fragmentation as implemented in the HERWIG [69] Monte Carlo.

The systematic uncertainties for semi-leptonic and hadronic final states are summarized in Tab. 6.5. Applying the correction due to the Bose-Einstein Correlation, including all the systematic effects, and combining all channels, the W boson mass measured at $\sqrt{s} = 189$ GeV is found to be

$$M_W = 80.33 \pm 0.10(stat.) \pm 0.07(syst.) \text{ GeV}$$

The first quoted error is statistical, while the second is due to systematic uncertainties. This measurement is in very good agreement with the preliminary L3 measurement obtained with the box method, where the measured W boson mass is $80.35 \pm 0.09(stat.) \pm 0.08(syst.)$ GeV [59].

74

Chapter 7

Conclusions

Two aspects in W boson physics were touched in the work presented here: the measurement of the W pair production cross section in electron-positron collisions, and the measurement of the mass of the W boson.

For the determination of the cross section, the semileptonic channel with two jets and a muon in the final state was considered. Using the developped event selection procedure, the data collected by the L3 experiment at the centre-of-mass energies of $\sqrt{s} = 183$ and 189 GeV was analyzed to evaluate the cross section of the process $e^+e^- \rightarrow WW \rightarrow qq\mu\nu$. The results are

$\sqrt{s}$ [GeV]	$\sigma_{qq\mu\nu}$ [pb]	$\sigma_{qq\mu\nu}^{SM}$ [pb]
183	$2.087 \pm 0.234 \pm 0.047$	2.29
189	$2.264 \pm 0.138 \pm 0.033$	2.36

where the first error is the statistical, and the second the systematic one. Both measurements agree very well within errors with the Standard Model prediction.

The selected events at $\sqrt{s} = 189$ GeV were used for a measurement of the W boson mass. A method based on maximum likelihood fit was implemented, using only the best and directly measured event parameters. The measurement was extended to make use also of other WW final states, in particular all the semileptonic channels and the fully hadronic final state. The mass of the W boson was determined to be

$$M_W = 80.33 \pm 0.10(stat.) \pm 0.07(syst.) \text{ GeV}$$

with the first error statistical, and the second due to systematic uncertainties.

Seite Leer /
Blank leaf

Appendix A

MIP Finder

Due to the geometrical arrangement of the muon chambers, the region in which a muon track can be reconstructed and it's momentum measured covers about $\sim 85\%$ of the solid angle. Muons passing through the detection gaps at $|\cos\theta| < 0.07$ and at $\phi = n\frac{2\pi}{16}, n = 0\ldots 15$ can be potentially recovered through their minimum ionizing particle signature. The coverage for muon detection raises to $\sim 93\%$ of the full solid angle. The region $|\cos\theta| > 0.91$ remains inaccessible, due to missing muon chambers' and TEC tracks in this region.

A.1 MIP Signal in L3

The signature of a muon traversing the L3 detector consists of a track in the central tracking chamber, usually with up to 2 hits in the SMD. It loses about 250MeV in the electromagnetic calorimeter, as can be seen in Fig. A.1. After hitting the scintillator counter, it traverses the hadron calorimeter with an average energy deposition of ~ 2 GeV, shown also in Fig. A.1. Passing though the muon spectrometer, it hits a maximum of three layers of muon chambers in the barrel, or four in the forward/backward region (c.f. Fig. 2.6). A minimum of two hits is required for a measurement of the muon's momentum. An example of a muon with signature in all subdetectors is shown in Fig A.2.

Throughout this document, a MIP is defined to be a particle matching the above signature, but having no reconstructed muon track (i.e. a maximum of one hit in the muon detector).

A.2 The Algorithm

The goal of the algorithm is to find particle signatures in the detector which are consistent with the signature of a minimum ionizing particle, with the best efficiency and highest muon purity possible. In this perspective, a technical definition of MIP was set to be an object in the detector, fulfilling the following criteria:

i. **Components:** the MIP must have a TEC track, in connection with a combination of

- energy deposit in the electromagnetic calorimeter,
- hits in the hadron calorimeter,
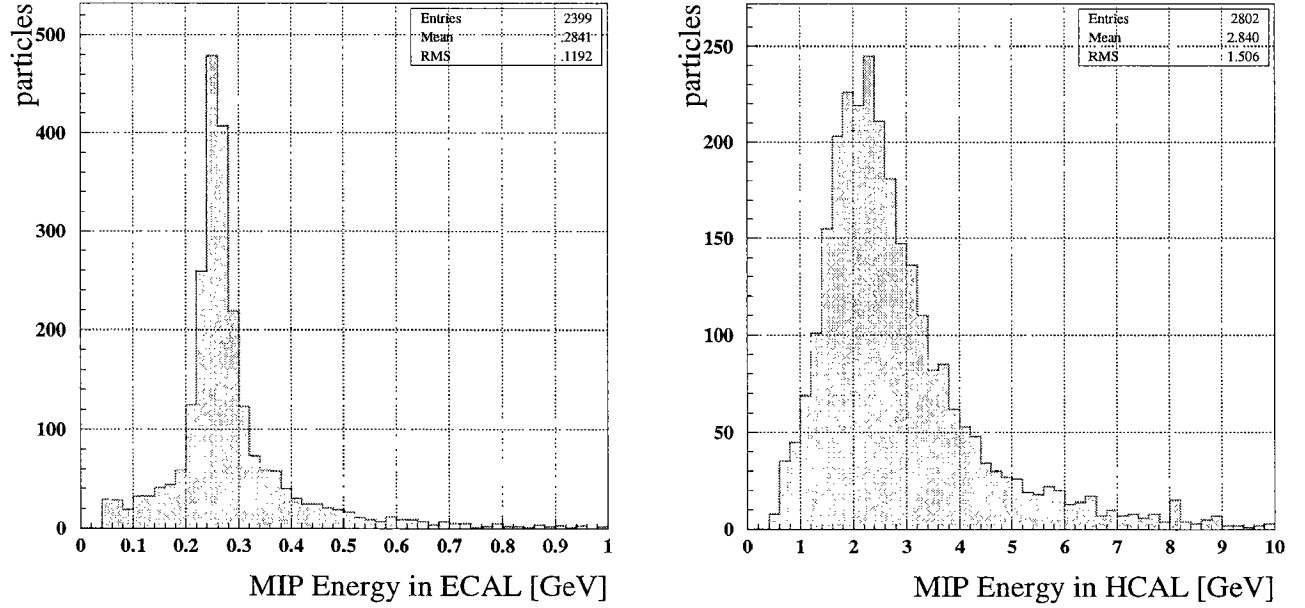- hits in the muon chambers.

Figure A.1: Energy loss of a minimum ionizing particle traversing the electromagnetic (left) and hadron (right) calorimeter.

ii. **Spatial Matching:** the calorimetric clusters must belong to the same particle that generated the TEC track.

iii. **Isolation:** in a jet, many low energetic particles can be created. A high momentum track in a jet might easily point towards calorimetric clusters belonging to low energetic particles. To avoid this, the MIP components are required to be isolated from other activity in the detector.

iv. **Kinematics:** since the muon is expected to loose about 2.5 GeV in the calorimeters, a minimum momentum of the TEC track is required.

All the components must be compatible with MIP signature. The conditions to be met are

Track:	DCA	$<$	1.0 mm
	ZDCA	$<$	30.0 mm
	# TEC hits	$\geq$	10
	span	$\geq$	16
ECAL Bump:	0.2 GeV	$<$ Energy $<$	0.4 GeV
	$\frac{E_9}{E_{25}}$	$>$	0.9
	# crystals	$\leq$	5
HCAL Hits:	1.0 GeV	$<$ Energy $<$	5.0 GeV
	10	$\leq$ # hits $\leq$	35

where the span of a TEC track is defined as the difference of the wire number of the last and first hit in the TEC, and E_9 and E_{25} denote the energy deposit in a 3×3 and 5×5 matrix of
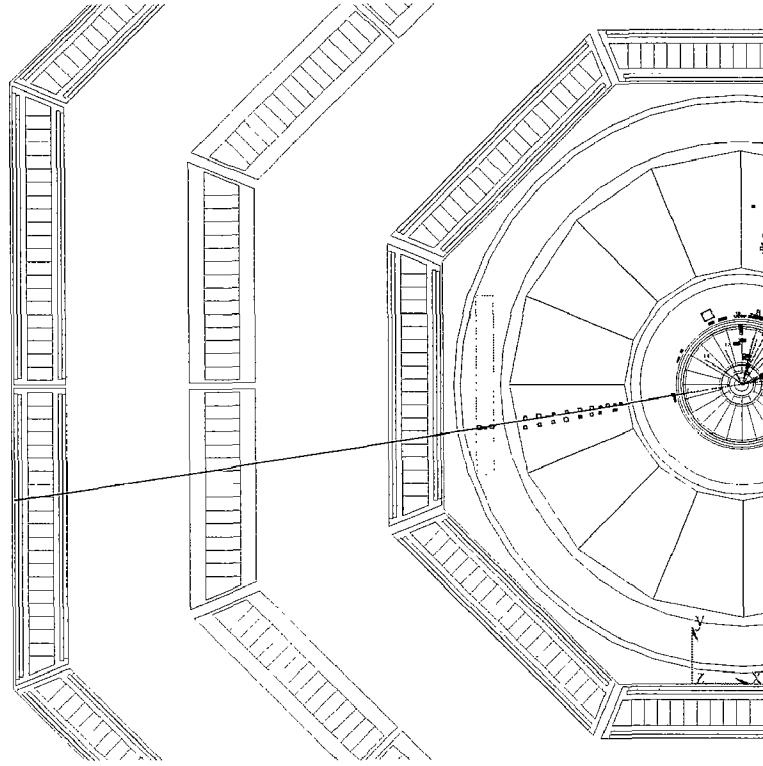
Figure A.2: A muon traversing the L3 detector. Visible are, from the interaction point outwards, the TEC track, a small energy cluster in the electromagnetic calorimeter shown just at the inner edge of the calorimeter, a clear track in the hadron calorimeter (together with its mirror track), hits in the muon filter and the track in the muon spectrometer. Not shown is the hit in the scintillator detector.

crystals, resp., centered at the crystal with the highest energy. The ratio of E_9/E_{25} represents a measure of the shape of the energy deposit in the ECAL.

In addition, if the TEC track is pointing into an active muon detector region, a matching cell hit, not associated to an already reconstructed muon track, is required as part of MIP signature.

The bump in the electromagnetic calorimeter and the hadron calorimeter cluster are required to match the TEC track within $6.8°$. The angle between the track and the hit in the muon detector has to be les than $5°$.

Isolation criteria were imposed on all the components. For the ECAL bumps, the difference of the energy within a $10°$ cone around the track direction and the energy of the candidate bump, $|E_{10°} - E_{matched}|$, has to be less than 0.8 GeV. No second high energetic track is allowed to match this energy deposit. In the case of a cluster in the HCAL, also the energy difference $|E_{10°} - E_{matched}|$ has to be less than 1.0 GeV. The number of hits in the candidate HCAL cluster must be in the range $10 - 35$. Also here, a veto on a second matching track is set. For the candidate muon chambers cell, it is required that it doesn't belong to an already reconstructed muon triplet or doublet. No second TEC track is allowed to point in it's direction, and the angle to the next reconstructed muon has to be at least $5°$.

The search is performed for all reconstructed TEC tracks with at least 10 GeV transverse momentum. The MIP candidate is then classified according to the components satisfing the matching and isolation criteria, into TEC+ECAL, TEC+HCAL, TEC+ECAL+HCAL, and

TEC+ECAL+HCAL+MUCH classes. A special flag (the 'golden MIP' flag) is set in the last class, and in the TEC+ECAL+HCAL class, if the track is pointing into detection gap region. It should be noted here, that the muon chamber information is only used here for identification, and the momentum measurement is performed by the TEC, in which case the momentum resolution is about 40%.

A summary of the parameters used in the MIP finder is shown in Tab. A.1.

A.3 Efficiency

With the definition of the MIP signal used, an efficient algorithm was implemented, yielding a pure sample of muons not detected by the muon spactrometer. The algorithm is simple and flexible, since it's implementation in the REL3 code enables a reconfiguration in terms of different parameter settings. The default values, set in REL3 reconstruction are the ones given in Tab A.1. For efficiency study, a dimuon Monte Carlo was used with a centre-of-mass energy of $\sqrt{s} = 91$ GeV. The probability of identifying a muon as a minimum ionizing particle was estimated to be $86.3 \pm 0.3\%$. The purity was studied on a W-pair Monte Carlo sample, where many hadrons are produced in the semi-leptonic and hadronic final states, with the resulting contamination of hadrons identified as MIP being $0.2 \pm 0.06\%$.

Using the MIP finder algorithm for the W cross section analysis in the WW $\rightarrow$ qq$\mu\nu$ channel, increased the efficiency of qq$\mu\nu$ selection by $\sim 6\%$, with a purity loss of less than 1%.

Parameter	Value
min. number of TEC hits	10
min. TEC track span	16
max. DCA	1.0 mm
max. ZDCA	30.0 mm
min. ECAL bump energy	0.2 GeV
max. ECAL bump energy	0.4 GeV
min. E_9/E_{25}	0.9
max. number crystals in ECAL bump	5
half cone angle ECAL	0.12 rad
min. HCAL cluster energy	1.0 GeV
max. HCAL cluster energy	5.0 GeV
min. hits in HCAL cluster	10
max. hits in HCAL cluster	35
half cone angle HCAL	0.12 rad
max. $\Delta\phi$ in ϕ fit	0.9°
max. ECAL energy in 10° cone	0.8 GeV
max. HCAL energy in 10° cone	1.0 GeV
min. p_T	10.0 GeV
max. angle to MUCH hit	5.0°
max. angle between track and ECAL bump	2.0°
min. angle to next reconstructed MUCH track	5.0°

Table A.1: Parameters in the MIP finder. The parameter values correspond to the default setting in the REL3 reconstruction code. The units given are the units in which the value has to be passed in the data cards. The half cone angle in ECAL/HCAL specifies the maximum angle between the TEC track and the calorimeter deposit.

Appendix B

Formulae

Error on $\sigma_{qq\mu\nu}$ from MC efficiency

With the $qq\mu\nu$ cross section given by Eq. 5.1,

$$\Delta\sigma_{qq\mu\nu}^{sig.effi} = \frac{\partial\sigma_{qq\mu\nu}}{\partial\epsilon_{sig}}\Delta\epsilon_{sig} = \frac{N_{sel} - N_{bkg}}{\epsilon_{sig}^2 L}\Delta\epsilon_{sig} = \sigma_{qq\mu\nu}\frac{\Delta\epsilon_{sig}}{\epsilon_{sig}}. \tag{B.1}$$

Error on $\sigma_{qq\mu\nu}$ from background subtraction

From the error on the number of background events of the process i, $N_{bkg}^i = \epsilon_{bkg}^i\sigma_{bkg}^i L$,

$$\Delta N_{bkg}^i = \sigma_{bkg}^i L\Delta\epsilon_{bkg}^i \tag{B.2}$$

the error on the $qq\mu\nu$ cross section given by Eq. 5.1 is calculated to be

$$\Delta\sigma_{qq\mu\nu}^{bkg.i} = \frac{\partial\sigma_{qq\mu\nu}}{\partial N_{bkg}^i}\Delta N_{bkg}^i = \frac{\sigma_{bkg}^i}{\epsilon_{sig}}\Delta\epsilon_{bkg}^i. \tag{B.3}$$

Systematic error on M_W from calibration curve parameters

The linear fit to the calibration curve gives the reconstructed W boson mass as function of the true mass:

$$M_W^{rec} = p_1(M_W^{true} - 80.5) + p_0 \text{ GeV}, \tag{B.4}$$

with the reference point of the true mass shifted to 80.5 GeV. The parameters p_1 and p_0 are determined, together with their errors and correlation parameter, in a linear fit to the M_W^{rec} vs. M_W^{gen} distribution, as described in Sec. 6.3.

Applying the calibration corrections on the reconstructed mass, the true W mass is then obtained to be

$$M_{\mathrm{W}}^{true} = \frac{1}{p_1} M_{\mathrm{W}}^{rec} - \frac{p_0}{p1} + 80.5 \text{ GeV}. \tag{B.5}$$

The systematic error due to the uncertainties on p_1 and p_0 is then

$$(\Delta M_W^{syst})^2 = \left(\frac{\partial M_{\mathrm{W}}^{true}}{\partial p_1}, \quad \frac{\partial M_{\mathrm{W}}^{true}}{\partial p_0} \right) \begin{pmatrix} \sigma_{p1}^2 & cov_{p1,p0} \\ cov_{p1,p0} & \sigma_{p0}^2 \end{pmatrix} \begin{pmatrix} \partial M_{\mathrm{W}}^{true}/\partial p_1 \\ \partial M_{\mathrm{W}}^{true}/\partial p_0 \end{pmatrix}$$

$$= \sigma_{p1}^2 \left(\frac{\partial M_{\mathrm{W}}^{true}}{\partial p_1} \right)^2 + \sigma_{p0}^2 \left(\frac{\partial M_{\mathrm{W}}^{true}}{\partial p_0} \right)^2 + 2cov_{p1,p0} \frac{\partial M_{\mathrm{W}}^{true}}{\partial p_1} \frac{\partial M_{\mathrm{W}}^{true}}{\partial p_0} \tag{B.6}$$

$$= \sigma_{p1}^2 \left(\frac{M_{\mathrm{W}}^{rec} - p_0}{p_1^2} \right)^2 + \sigma_{p0}^2 \frac{1}{p_1} + 2cov_{p1,p0} \frac{M_{\mathrm{W}}^{rec} - p_0}{p_1^3}$$

Appendix C

Monte Carlo Integration

The technique of Monte Carlo integration is based on the mean value theorem known from calculus:

$$I = \int_a^b dx f(x) = (b - a)\langle f \rangle, \tag{C.1}$$

where $\langle f \rangle$ denotes the mean of the function f taken over the interval $[a, b]$. It is this mean value which is determined by Monte Carlo techniques: the mean of f is taken to be the average of $f(x_i)$ with the x_i being uniform random numbers in the interval $[a, b]$:

$$\langle f \rangle \approx \frac{1}{N} \sum_{i=1}^N f(x_i). \tag{C.2}$$

If the calculations are performed with an accuracy of σ_f, then, assuming normal distribution, the statistical error on I using N samples is given by

$$\sigma_I \approx \frac{1}{\sqrt{N}} \sigma_f. \tag{C.3}$$

This means that the error on the calculated value decreases as $1/\sqrt{N}$, and most important, it is independent of the dimensionality of the parameter space. While the convergence of numerical quadrature methods depends strongly on the dimension, the error being $1/N^{k/D}$, with k depending on the method [70], the Monte Carlo integration shows better performance in the case above $D = 3 - 4$ dimensions. In our case, with $D = 10$, this method is by far the most powerful integration technique. The D-dimensional integral is calculated as

$$I = \int_{a_1}^{b_1} dx^1 \int_{a_2}^{b_2} dx^2 \ldots \int_{a_D}^{b_D} dx^D f(x^1, \ldots, x^D) \approx \left(\prod_{i=1}^D (b_i - a_i) \right) \langle f \rangle$$
$$\approx \left(\prod_{i=1}^D (b_i - a_i) \right) \frac{1}{N} \sum_{i=1}^N f(x^1, \ldots, x^D). \tag{C.4}$$

C.1   Importance Sampling

A problem for every integration technique is the integration of a rapidly varying function. In the case of Monte Carlo integration, this usually means that very large sample size N is required to

obtain reasonable accuracy. One method to improve the integration is the so called importance sampling. The integral is rewritten to be

$$I = \int_a^b dx f(x) = \int_a^b dx \; w(x)\frac{f(x)}{w(x)}. \tag{C.5}$$

Using $w(x)$ as the weighting function or probability distribution for the random numbers x_i, the integral is approximated as

$$I = \left\langle \frac{f}{w} \right\rangle \approx \frac{1}{N}\sum_{i=1}^N \frac{f(x_i)}{w(x_i)}. \tag{C.6}$$

With a smart choice of the weighting function $w(x)$, the integrand $\frac{f(x)}{w(x)}$ can be made "flatter", i.e. easier to integrate.

In particular, in our case the integrand in Eq. 6.5 is a product of a function with D-dim. Gaussian. Taking the latter to be the weighting function, the performance of the integration can be improved twofold: a) the rapid falloff of the Gaussian is avoided, and b) the integrand is just the differential cross section itself:

$$f(\Psi') = \mathcal{R}(\Psi', \Psi)\frac{d\tilde{\sigma}(\Psi')}{d\Psi}, \tag{C.7}$$

so that

$$I = \left\langle \frac{f(\Psi')}{\mathcal{R}(\Psi', \Psi)} \right\rangle = \frac{1}{N}\sum_{i=1}^N \frac{d\tilde{\sigma}(\Psi')}{d\Psi}. \tag{C.8}$$

Appendix D

Parallel Code Implementation

In order to speed up the development time of the mass fit code, which needed many test runs with relatively high number of steps in the Monte Carlo integration, the code was written such as to enable parallel computation of the likelihood function at different mass points. For this purpose, the PVM package [72] was used, and the parallel tasks were run on several HP workstations in the L3 offline cluster [73]. Later on, the Beowulf cluster Asgard [74], of the ETH, comprising of 192 nodes of dual Pentium III machines, was used for processing of vaste amounts of simulation data, in order to estimate the systematic uncertainties of the mass calculation. The processing of the complete data sample collected at $\sqrt{s} = 189$ GeV takes about 8 hours on Asgard, when run in parallel in all channels.

The calculation of the likelihood function is performed at N different mass values of the W boson, with $N = 7$ here. This can be regarded as a calculation on a one dimensional grid, and the obvious choice for parallelization is to perform the calculation at each grid point on one processing node. Since the calculations are independent of each other, i.e. no communication is required between the computing nodes, a master/slave approach was chosen. The structure is depicted in Fig. D.1. The master task is coordinating the calculations on the slave nodes. It
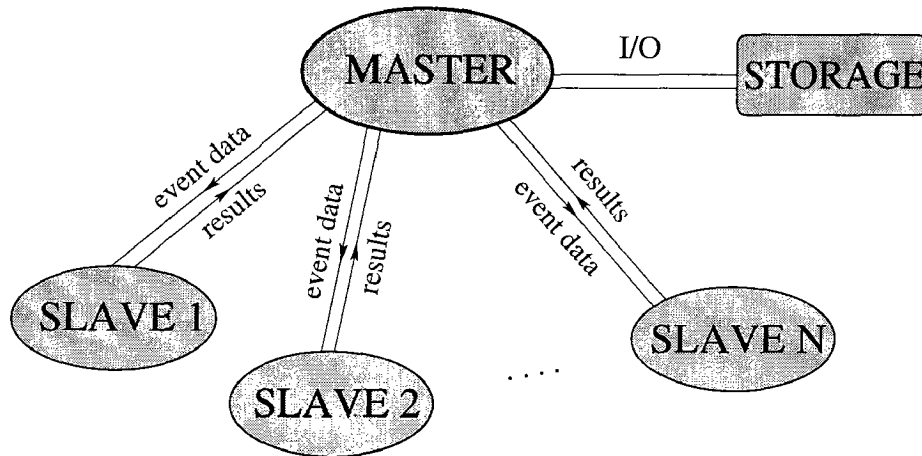

Figure D.1: Structure of the parallel implementation of the mass calculation algorithm.

is the only task performing I/O operations, and distributing the input data to the slaves. It collects the results from slave nodes, arranges it according to the input mass, and stores the results in an output file. Input data is transferred as a whole to the node executing the master task, thus reducing the I/O operations to the outside world. The only data transfer occurs

therefore just between the computing nodes and the master node. According to the Beowulf principle, the Ethernet (100Mbit/s in the case of Asgard) connection between the nodes can be regarded as an internal bus of a multi-processor machine. The computing nodes themselves can only be reached through a service node, which limits the traffic on the 'bus' to the necessary minimum.

In the current implementation, a blocking *receive* is issued by the master task, while it's waiting for the return of the data from the slave nodes. Only when all nodes have finished calculation, and delivered results without error status, the returned values are stored. This synchronous calculation could be circumvented by means of the non-blocking *receive* function call of PVM. The idle time of the computing nodes could be reduced in this manner, since the calculation of the next event could be started, before the processing of the last event is finished. However, refined bookkeeping and a good error recovery mechanism would be mandatory, in order to guarantee data integrity and avoid significant data (and computing time) losses in case of failure on one of the nodes.

As mentioned above, the algorithm can be regarded as a calculation on a one dimensional grid. The measurement can be extended to obtain the width of the W boson simultanously with the W mass. The implementation of the code is rather straight forward, with the mass and width forming a two dimensional grid for the likelihood function calculation. The increase in computing time needed for a calculation performed on 7×7 grid points (wrt. to the one dimensional case of 7 grid points) is expected to be marginal, and caused only by increased data traffic between the master and the slave nodes.

Appendix E

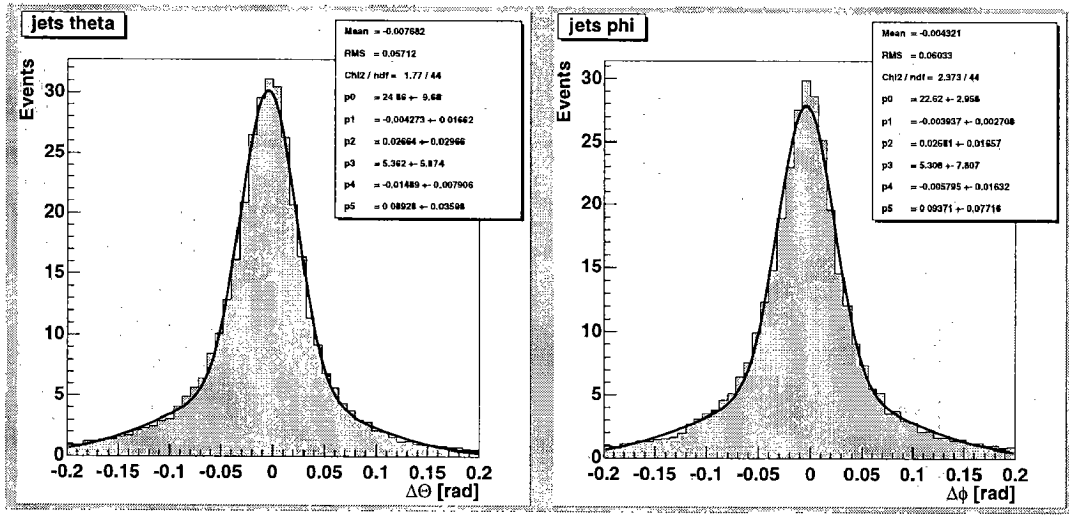# Additional Plots

E.1 Resolution Plots

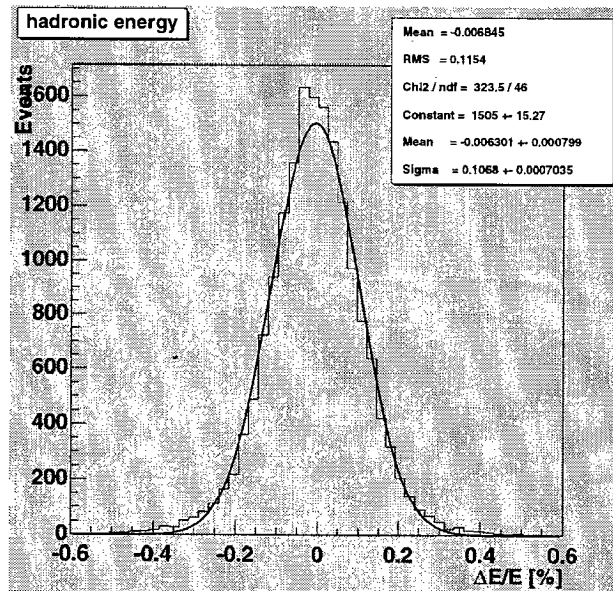Figure E.1: Resolution plots for the jet angles.
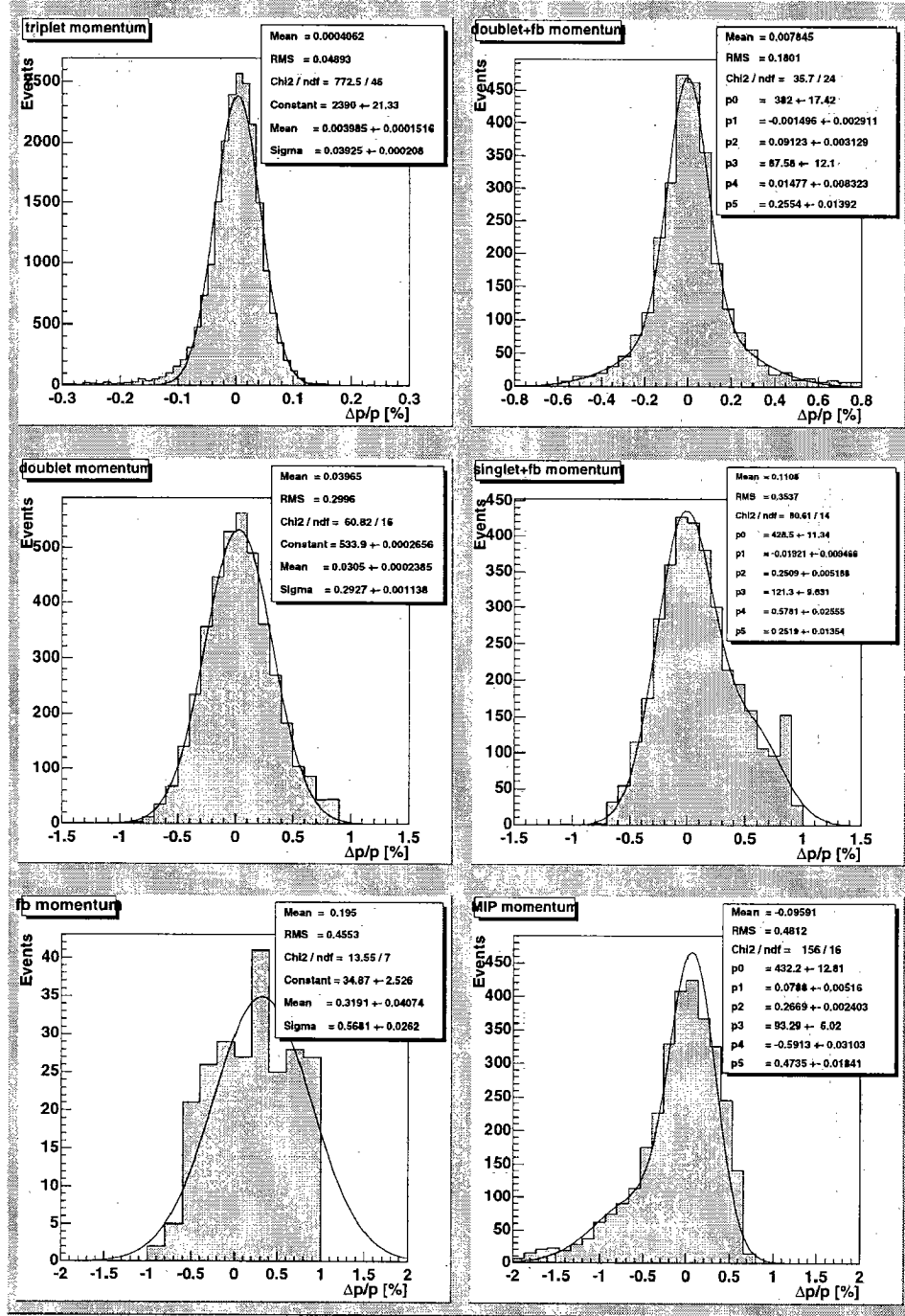

Figure E.2: Hadronic energy resolution.
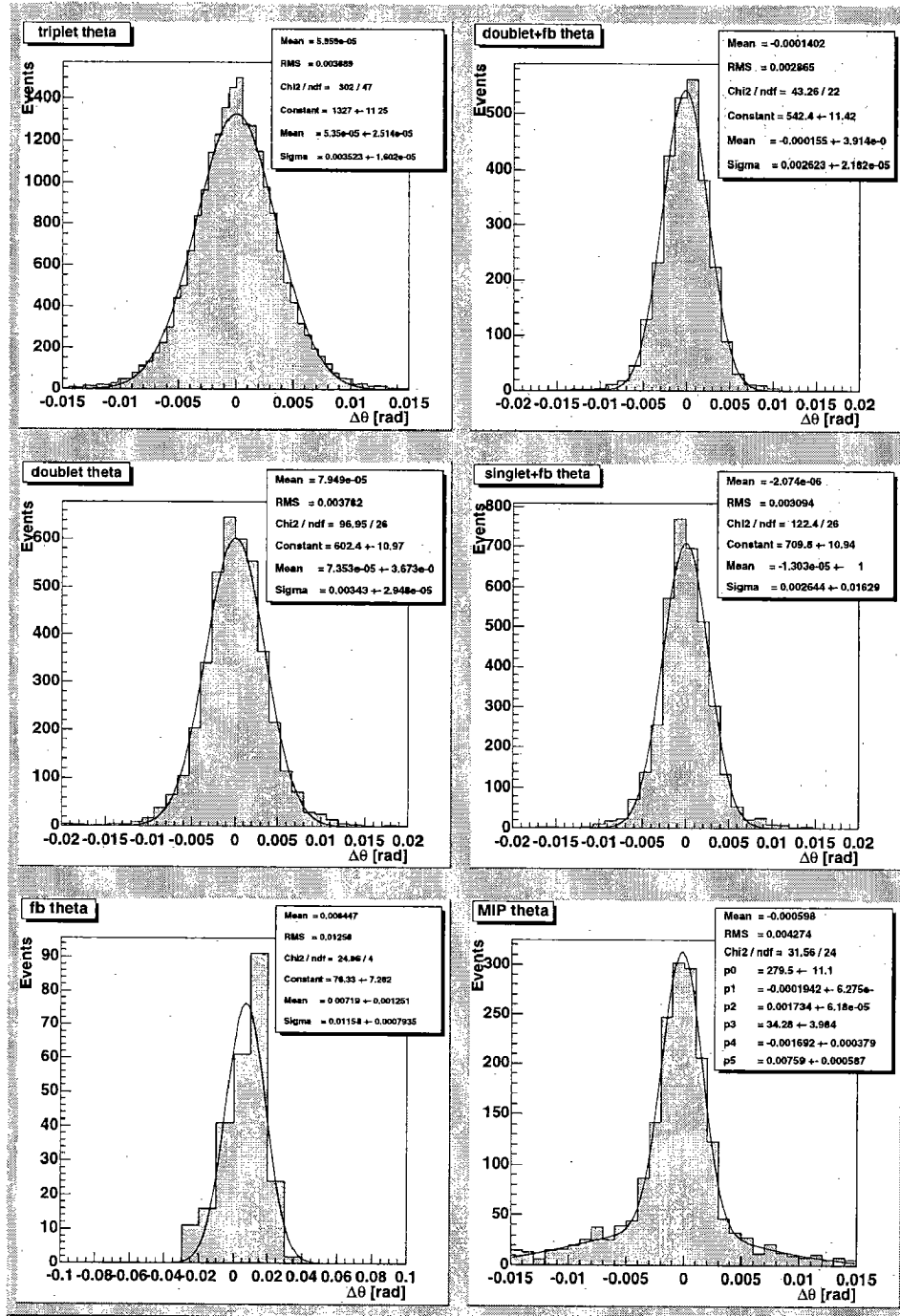
Figure E.3: Muon energy resolution plots.
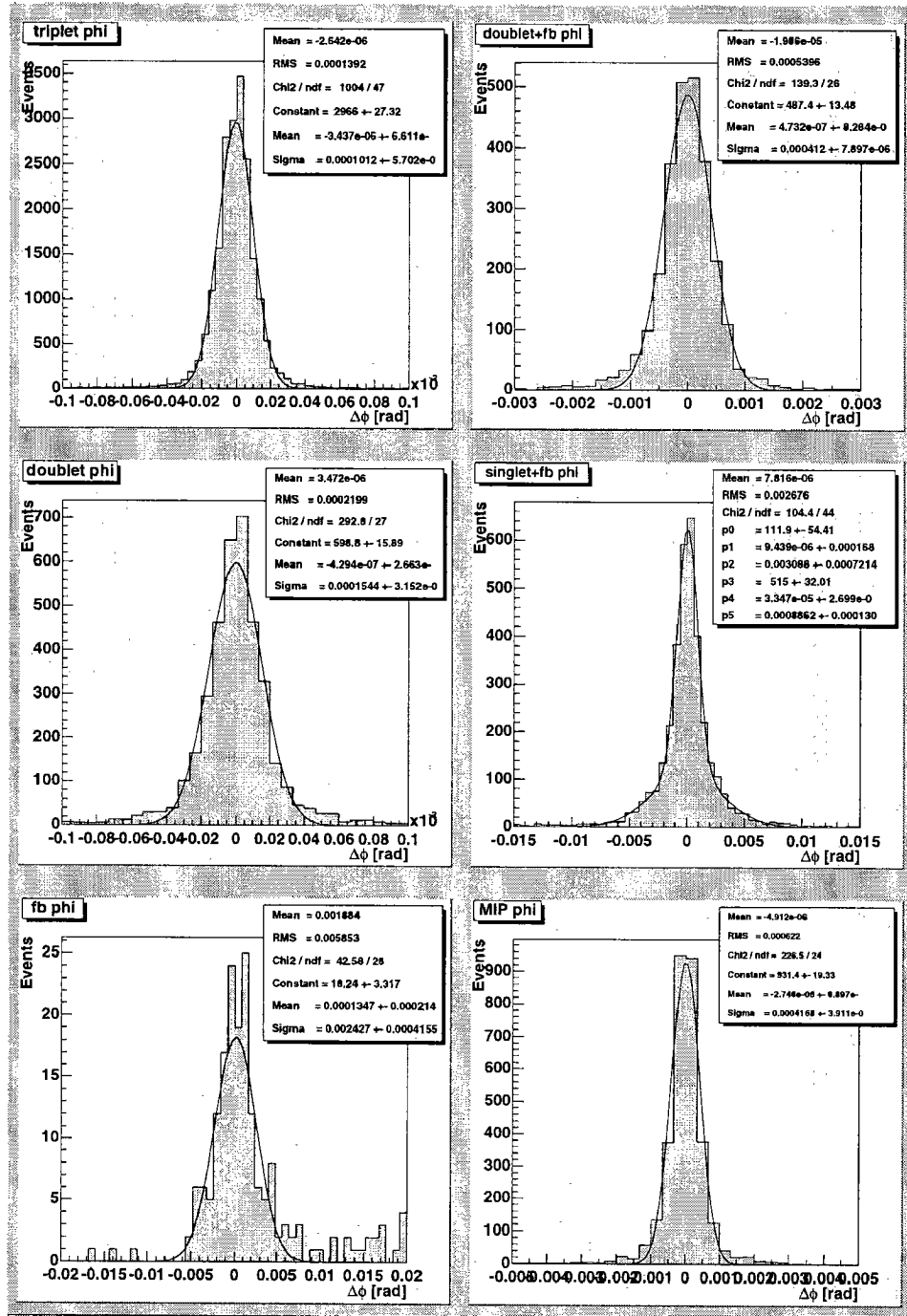
Figure E.4: Muon polar angle resolution plots.

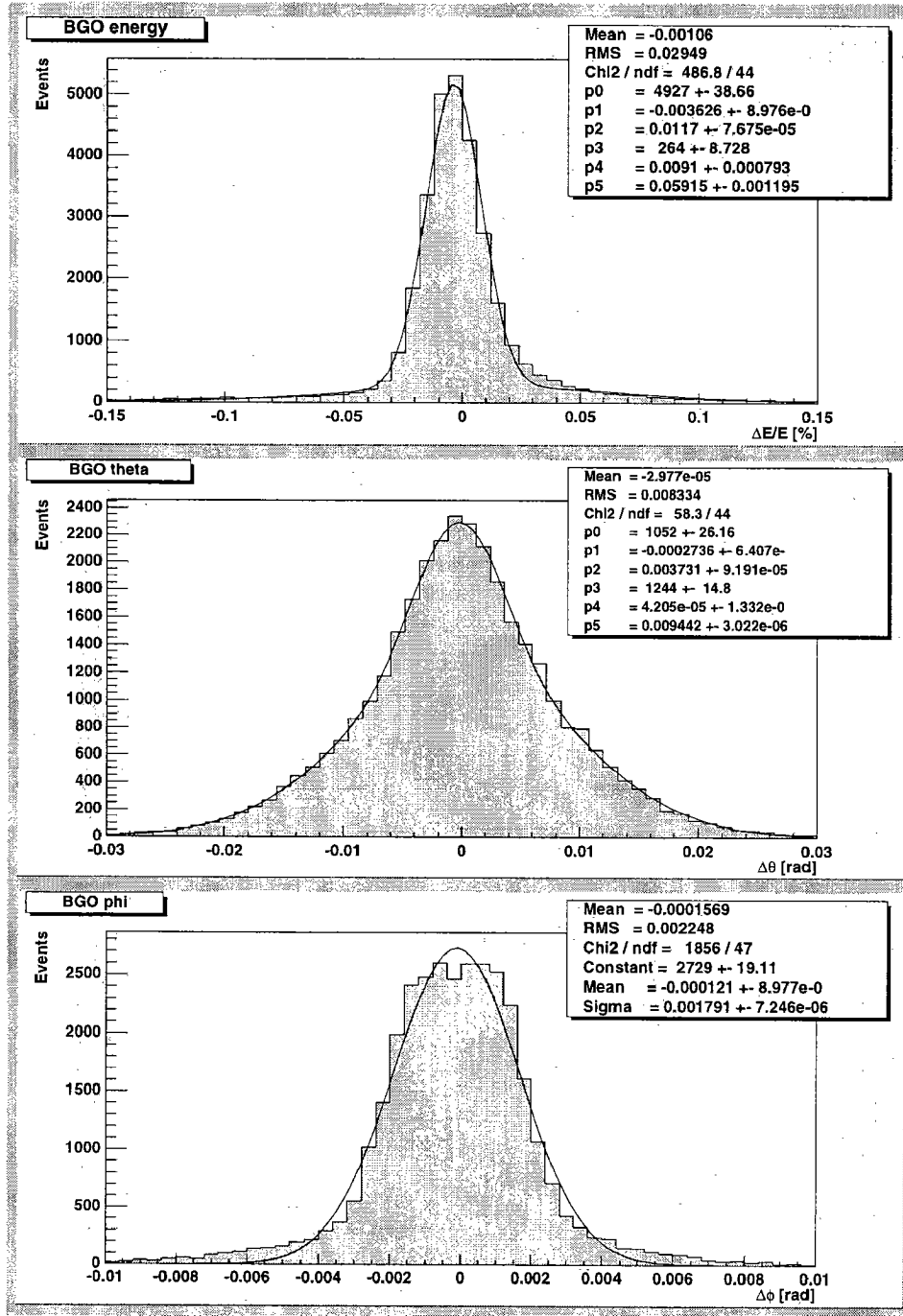Figure E.5: Muon azimutal angle resolution plots.

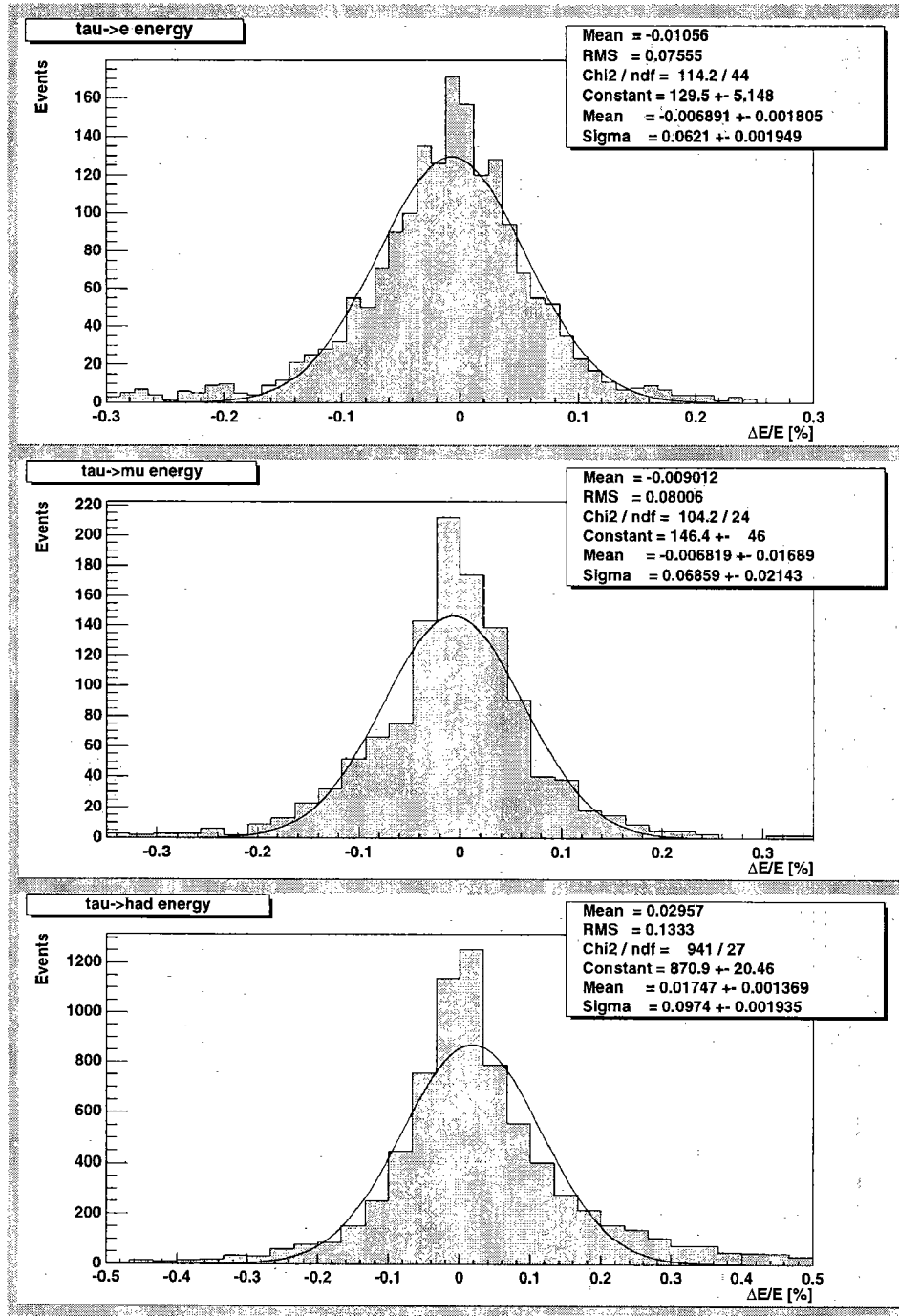Figure E.6: Electron resolution plots.

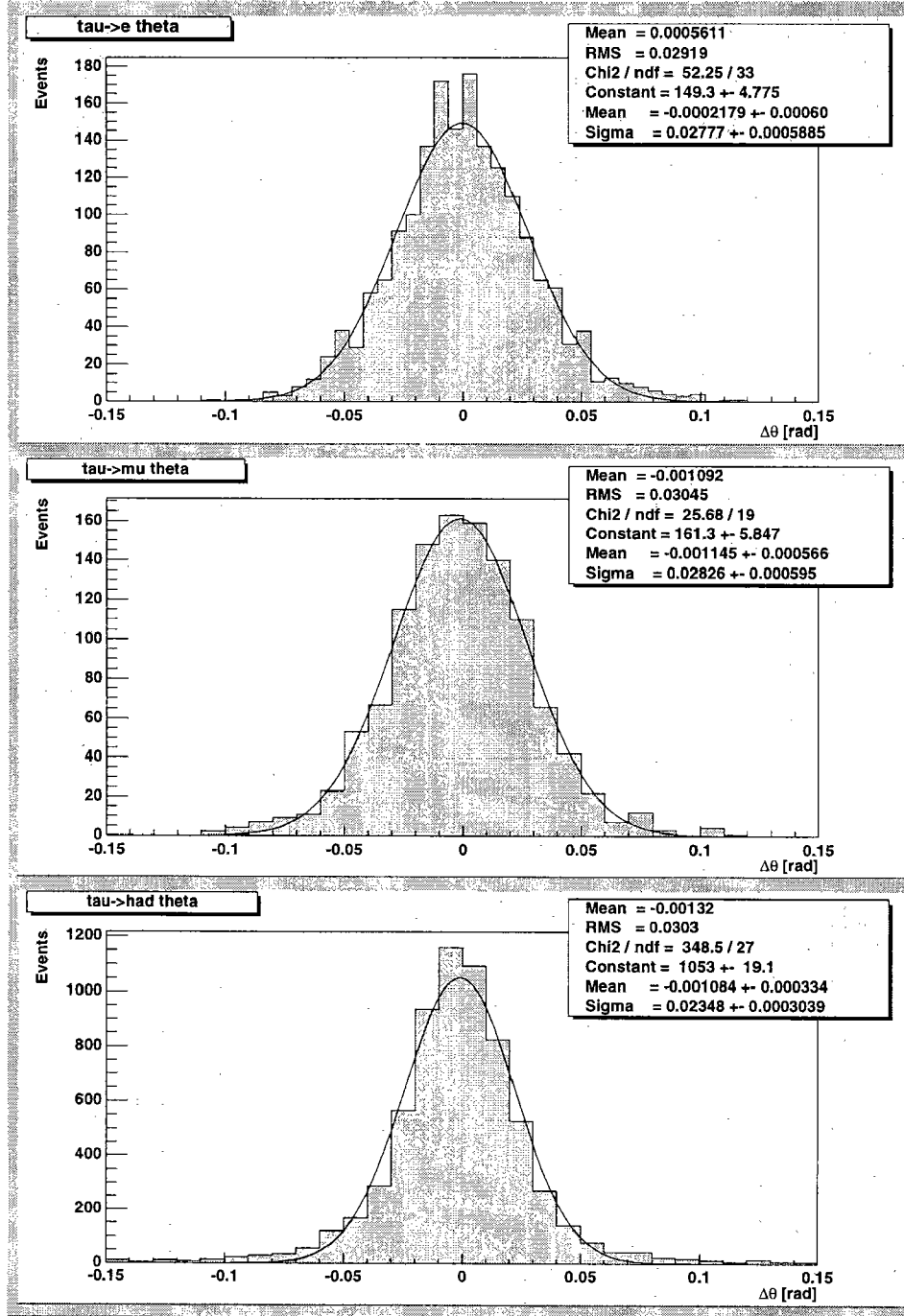Figure E.7: Tau energy resolution plots.

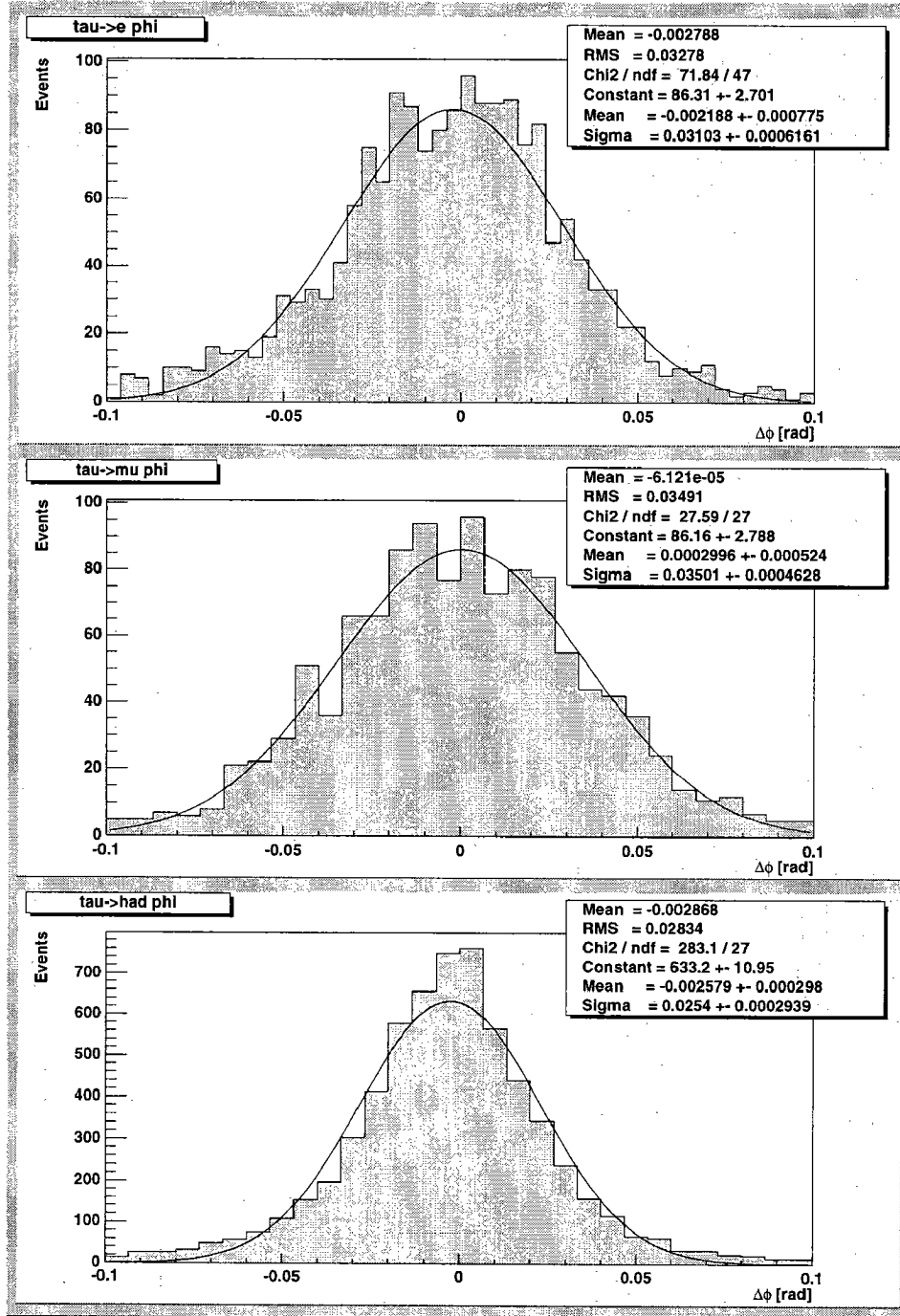Figure E.8: Tau polar angle resolution plots.

Figure E.9: Tau azimutal angle resolution plots.

E.2 Data/Monte Carlo Comparison

Figure E.10: Comparison of data with Monte Carlo events after full detector simulation in the WW $\to$ qqe$^-\nu$ channel.

Figure E.11: Comparison of data with Monte Carlo events after full detector simulation in the WW → qqe$^+\nu$ channel.

Figure E.12: Comparison of data with Monte Carlo events after full detector simulation in the WW $\to$ qq$\mu^-\nu$ channel.

Figure E.13: Comparison of data with Monte Carlo events after full detector simulation in the WW → qqμ⁺ν channel.
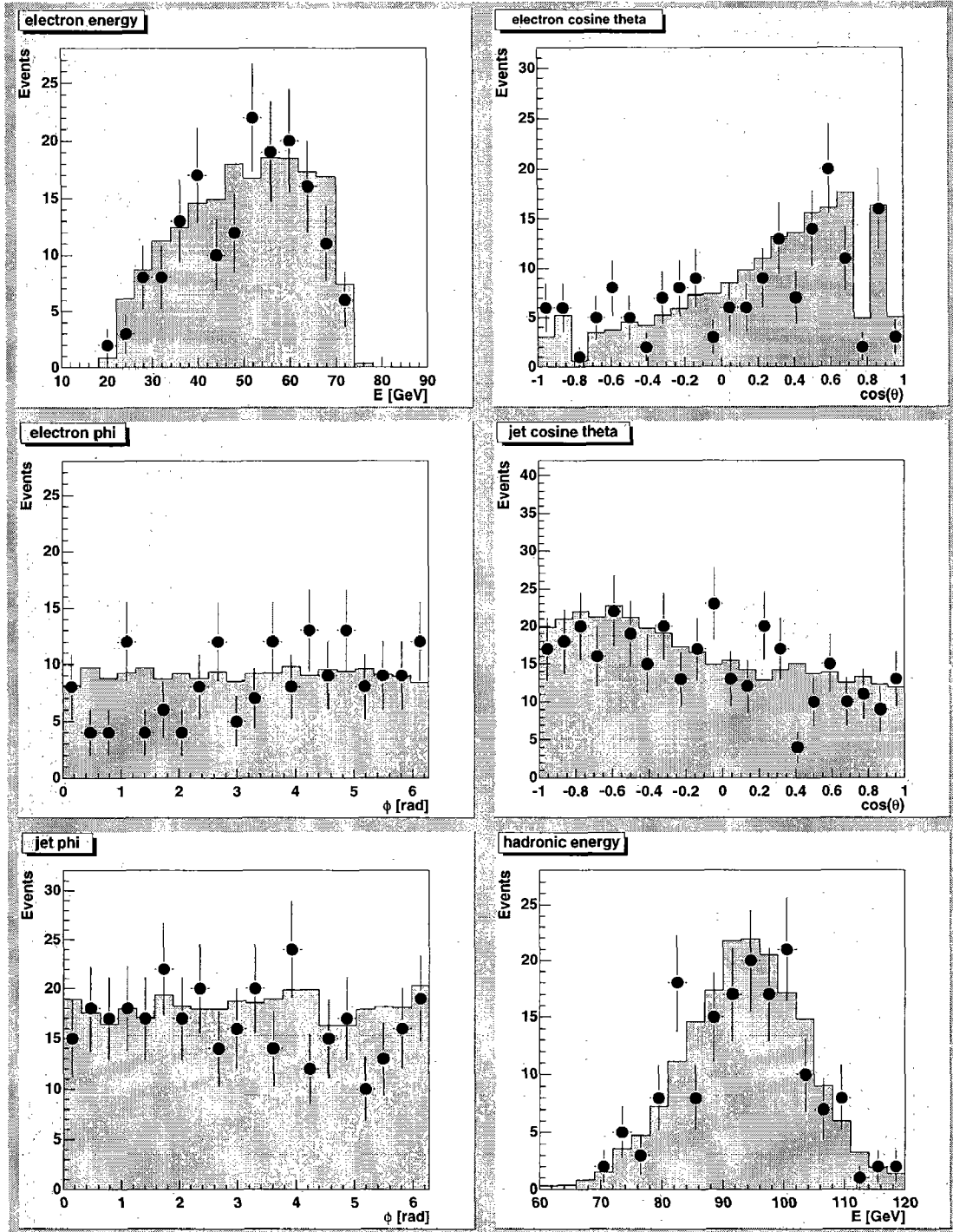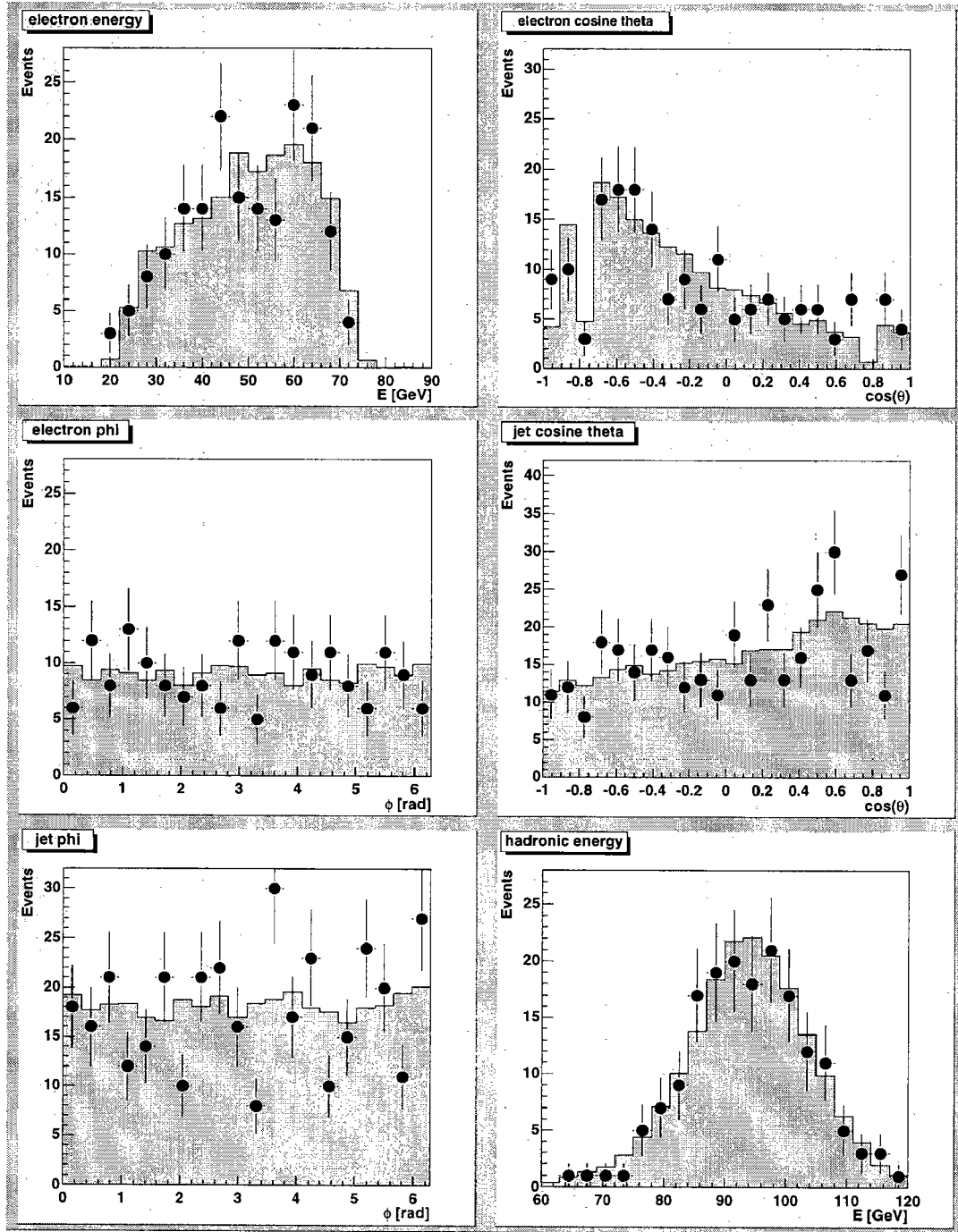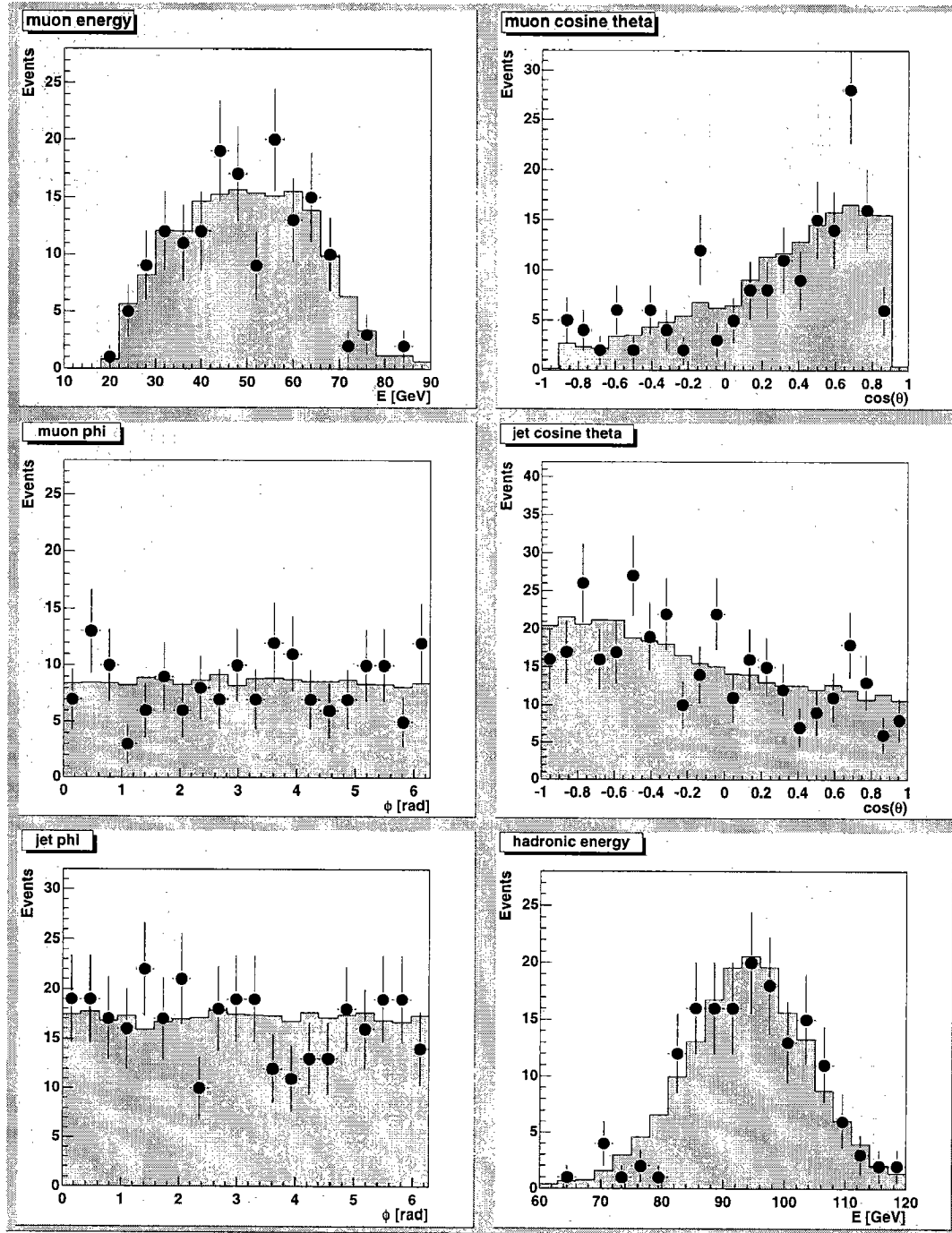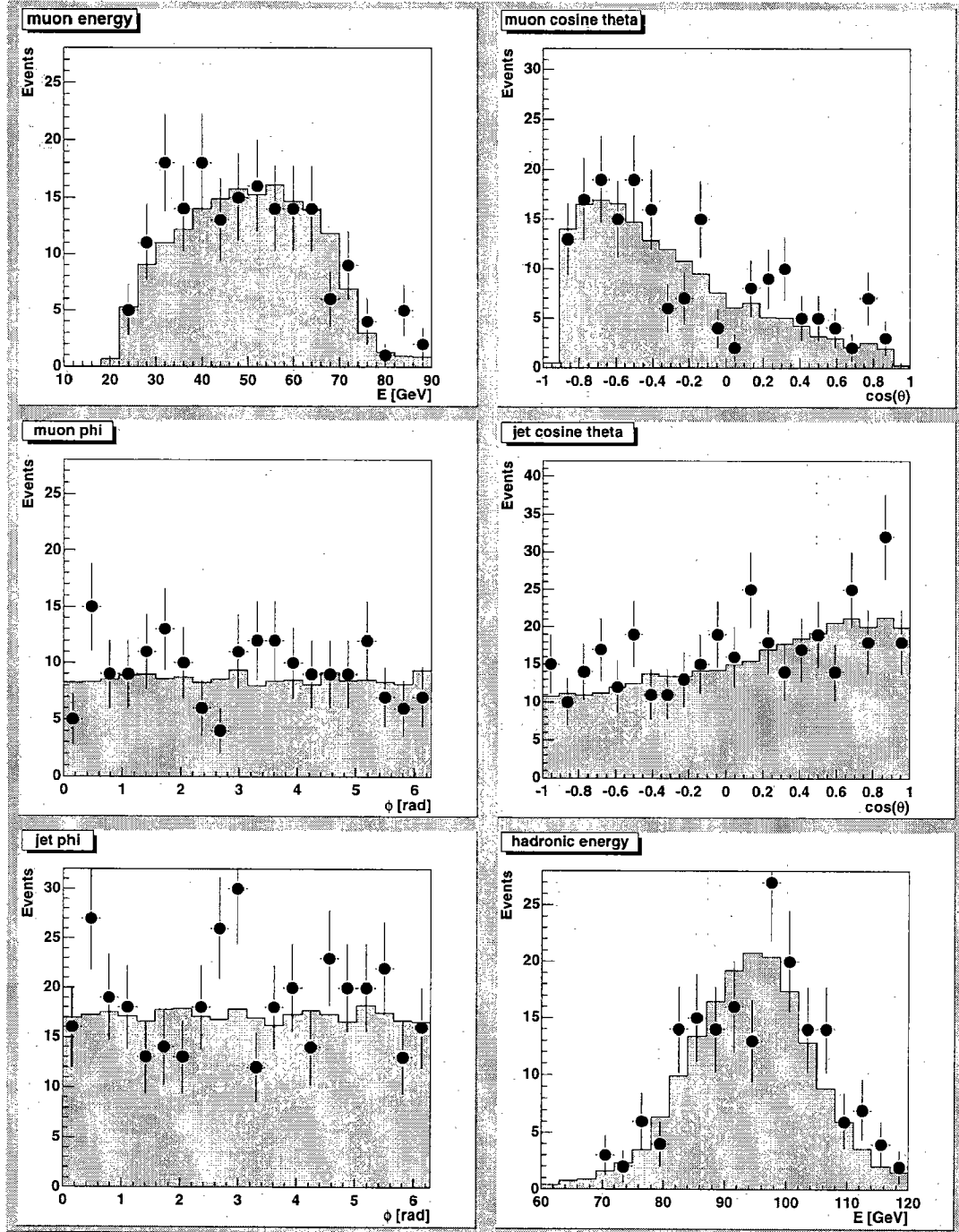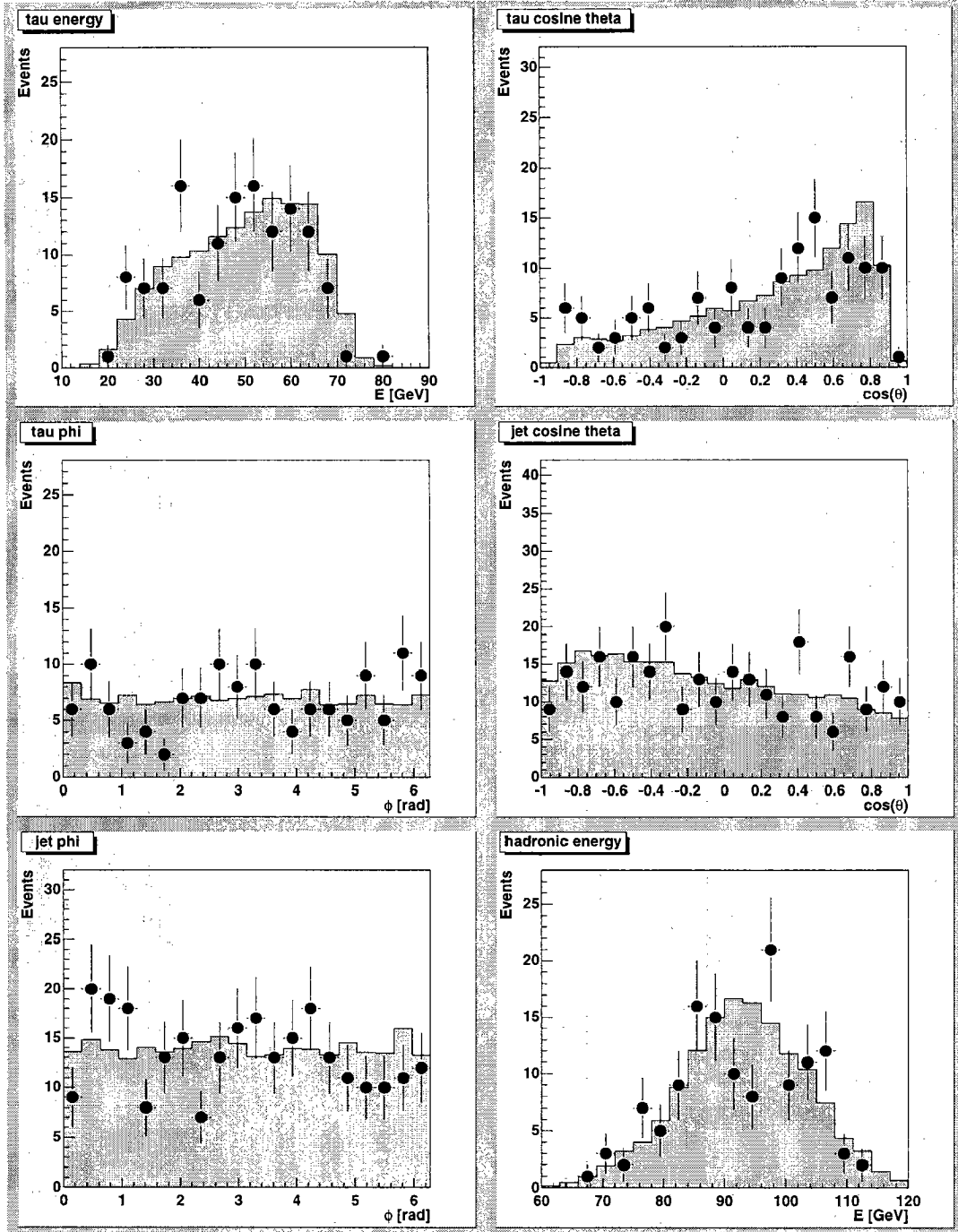
Figure E.14: Comparison of data with Monte Carlo events after full detector simulation in the
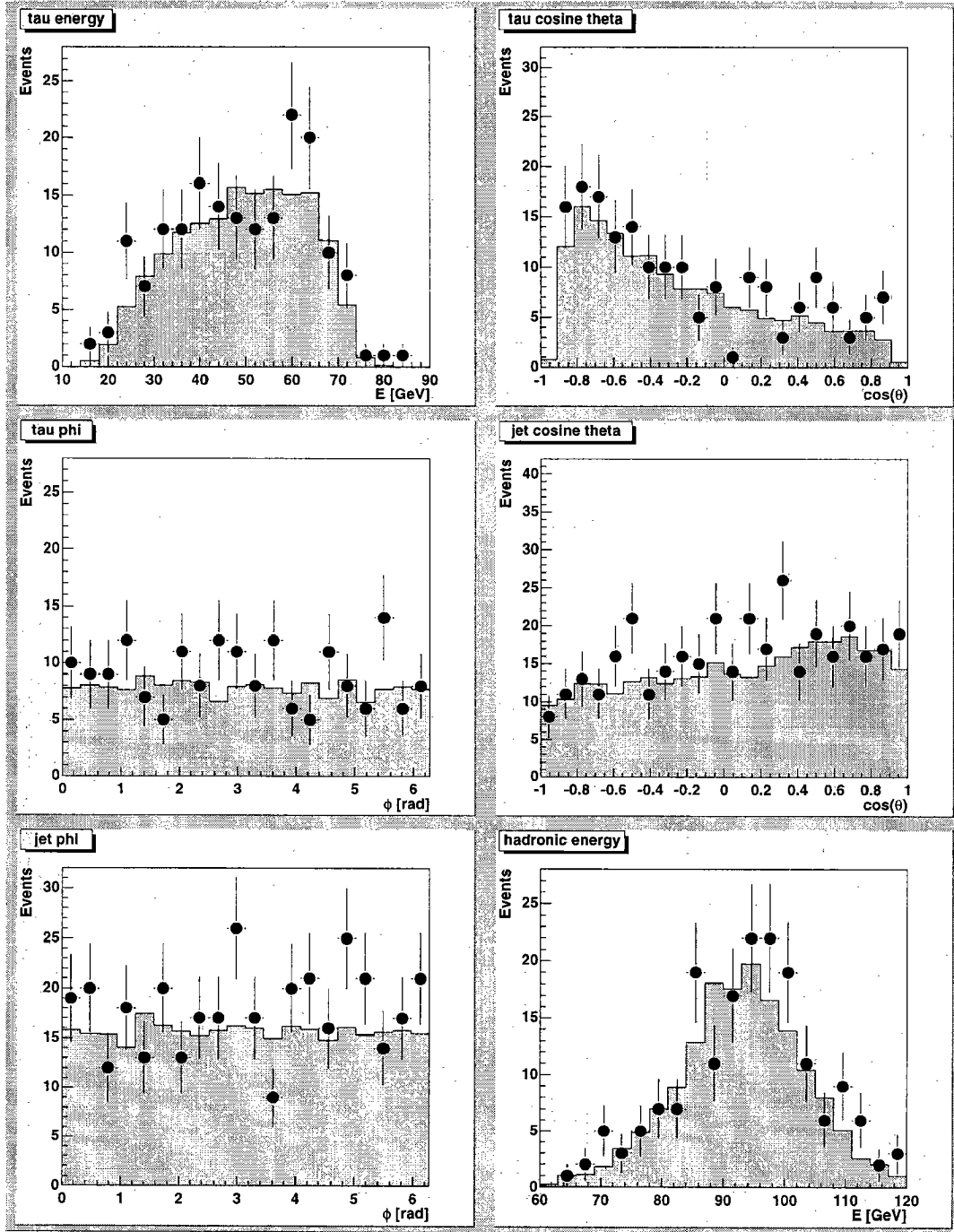WW $\rightarrow$ qq$\tau^-\nu$ channel.

Figure E.15: Comparison of data with Monte Carlo events after full detector simulation in the WW $\to$ qq$\tau^+\nu$ channel.

Bibliography

[1] S. Glashow, Nucl. Phys. **22** (1961) 579
S. Weinberg, Phys. Rev. Lett. **19** (19676) 1264
A. Salam, in *Elementary Particle Theory*, ed. N. Svartholm, Stockholm, Almquist and Wiksell (1968) 367

[2] G. Arnison et al., Phys. Lett. **B 126** (1983) 398

[3] P. Bagnaia et al., Phys. Lett. **B 129** (1983) 130

[4] P. Higgs, Phys. Lett. **12** (1964) 132; Phys. Rev. Lett. **13** (1964) 508

[5] C. Caso and A. Gurtu, in *Review of Particle Physics*, Eur. Phys. J. **C 3** (1998) 227

[6] D. Decamp et al., Nucl. Inst. Meth. **A 294** (1990) 121

[7] P. Aarnio et al., Nucl. Inst. Meth. **A 303** (1991) 233

[8] B. Adeva et al., Nucl. Inst. Meth. **A 289** (1990) 35

[9] U. Ahmet et al., Nucl. Inst. Meth. **A 305** (1991) 275

[10] R. Hausammann, Nucl. Inst. Meth. **A 263** (1988) 1

[11] M. Acciarri et al., Nucl. Inst. Meth. **A 351** (1994) 300

[12] D. Kamrad, 'Untersuchungen zur Ortsmeßgenauigkeit des Silizium Mikrovertex Detektors von L3', Diploma thesis, Humboldt-Universität zu Berlin, 1995

[13] F. Beissel et al., Nucl. Inst. Meth. **A 332** (1993) 33

[14] R. Summer et al., Nucl. Inst. Meth. **A2 65** (1988) 252

[15] L3 Collaboration, CERN-PPE/96-07

[16] U. Uwer, 'The L3 Scintillation Counter System: Description and Status', L3 Note 2003 (1997)

[17] O. Adriani et al., Nucl. Inst. Meth. **A 302** (1991) 53

[18] B. Adeva et al., Nucl. Inst. Meth. **A 323** (1992) 109

[19] M. Fabre, 'The Dimuon Mass Resolution of the L3 Experiment at LEP', ETH Zürich, Ph.D. Thesis 9696 (1992)

[20] A. Adam et al., Nucl. Inst. Meth. **A 383** (1996) 342

[21] A. Aloisio et al., Nucl. Inst. Meth. **A 379** (1996) 552

[22] I. Brock et al., Nucl. Inst. Meth. **A 381** (1996) 236

[23] X. Cai, 'Contribution to the trigger and data acquisition system of the L3 experiment at LEP', Université de Savoie, Annecy-Le-Vieux, Ph.D. Thesis (1994)

[24] T. Angelov et al., Nucl. Inst. Meth. **A 306** (1991) 536

[25] P. Béné, et al., Nucl. Inst. Meth. **A 306** (1991) 150

[26] L. Tauscher, S. Vlachos, M. Wadhwa, 'A charged particle trigger based on neural networks for the L3 experiment using the inner-TEC detector', L3 Note 2016 (1996)

[27] F.R. Leimgruber et al., Nucl. Inst. Meth. **365** (1995) 198

[28] M. Fukushima, 'L3 Level-1 Muon Trigger', L3 Note 515 (1987)

[29] H. Groenstege, 'The Muon Triggerinterface for L3: MPC,PCC', L3 Note 671 (1989)

[30] M. van Heijningen, 'Hardware description of the FBROC module for the L3 FBMUON read-out system', Electronics Department, NIKHEF-H, Amsterdam, EH 819.14.27 (1993)

[31] A. Aloisio et al., Nucl. Inst. Meth. **A 360** (1995) 340

[32] S. X. Wu, 'F/B Muon Trigger Processor', (1994), unpublished

[33] B. Smith, 'High Energy Pair Production of Muons in Electron-Positron Annihilation at Center of Mass Energies Ranging from 130 to 183GeV', Massachusetts Institute of Technology (1998), Ph.D. Thesis, App. C

[34] B. Smith, private communication

[35] D. Della Volpe, private communication

[36] http://pcl3on2.cern.ch/CEA

[37] R. Bizzarri et al., Nucl. Inst. Meth. **A 317** (1992) 463
P. Bagnaia et al., Nucl. Int. Meth, **A 344** (1994) 212

[38] P. Beingessner et al., Nucl. Inst. Meth, **A 340** (1994) 322

[39] A. Masserot, 'Mise en oevre et intégration dans l'expérience L3 d'un déclenchement de deuxième niveau avec assemblage de l'événement, développé autour d'un réseau de routers dynamiques C104 et de Transputers T9000', Université de Savoie, Annecy-Le-Vieux, Ph.D. Thesis (1995)

[40] D. Kirkby, 'π^0/γ Discrimination in L3 Using Shower-Shape Analysis', L3 Note 1816 (1995)

[41] GEANT version 3.15 is used: R. Brun et al., 'GEANT 3', CERN-DD/EE/84-1 revised (1987)

[42] F.A. Bardin, R. Kleiss, R. Pittau, Nucl. Phys. **B 424** (1994) 308

[43] W.J.Stirling, J. Phys. G. **17** (1991) 1537;
S. Catani et al., Phys. Lett. **B 269** (1991) 432;
S. Bethke et al., Nucl. Phys. **B 370** (1992) 310

[44] M.Acciarri et al., Phys. Lett. **B 436** (1998) 437

[45] C. Paus-Cecchi, 'Cross section measurement of $e^+e^- \rightarrow$ WW at $\sqrt{s} = 161, 172$ and 183 GeV and W mass determination with L3 at LEP', Perugia Univeristy, Ph.D Thesis (1998)

[46] M. Campanelli, 'W physics with the L3 detector at LEP', ETH Zürich, Ph.D. Thesis 12742 (1998)

[47] M. Acciarri et al., Phys. Lett. **B 403** (1997) 168

[48] M.Skrzypek et al., Comp. Phys. Comm. **94** (1996) 216

[49] Z. Kunszt et al., in *Physics at LEP 2*, eds G. Altarelli, T. Sjöstrand, F. Zwirner, Report CERN 96-01 (1996), Vol. 1, p. 141

[50] M. Acciarri et al., Phys. Lett. **B 398** (1997) 223

[51] A. Wong Chan et al., 'Limits on the W mass measurement using the leptonic decays of the W boson with the L3 detector at LEP-II', L3 Note 1761 (1995);
N. V. Batalova, A. V. Shvorob, 'Measurement of W Boson Mass with Lepton Energy Spectra in W $\rightarrow$ lν Decays', L3 Note 2482 (1999)

[52] D. Bardin et al., Comp. Phys. Comm. **104** (1997) 161

[53] F.A. Berends et al., CERN-TH/97-224

[54] F.A. Berends et al., CERN-TH/98-221

[55] F.A. Berends et al., Nucl. Phys. **B 424** (1994) 308; Nucl.Phys. B426 (1994); Comput. Phys. Comm. **85** (1995) 437

[56] L. Malgeri, private communication

[57] M. Acciarri et al., Phys. Lett. **B 454** (1999) 386

[58] A. Weber, 'How to Determine the W-Mass from the Mass Spectrum of the Decay Products - The Box Method -', L3 Note 2079 (1997);
M. Campanelli, 'The Box Method for W Mass Fit', L3 Note 2082 (1997)

[59] L3 Collaboration, 'Preliminary Results on the Measurement of the Mass and Width of the W Boson at LEP', L3 Note 2377 (1999)

[60] F.A. Berends et al., HEP-PH/0002249

[61] G. Gustafson, U. Petterson, P.M. Zerwas, Phys. Lett **B 209** (1988) 90

[62] G. Gustafson, J. Häkkinen, Z. Phys. **C 64** (1994) 659

[63] T. Sjöstrand and V. A. Khoze, Z. Phys. **C 62** (1994) 281

[64] S. Jadach, K. Zalewski, Acta Phys. Polon. **B 28** (1997) 1362

[65] L. Lönnblad, T. Sjöstrand, Phys. Lett **B 351** (1995) 293

[66] L3 Collaboration, 'Measurement of Bose-Einstein Correlations in $e^+e^- \to$ WW at $\sqrt{s} =$ 189 GeV', submitted to Phys. Lett. B (2000)

[67] L. Lönnblad, T. Sjöstrand, E. Phys. J. **C 2** (1998) 165

[68] PYTHIA version 5.7 is used: T. Sjöstrand, 'PYTHIA 5.7 and JETSET 7.4 Physiscs Manual', CERN-TH/7112/93 (1993) rev. Aug. 1995; Comp. Phys. Comm. **82** (1994) 74

[69] HERWIG version 5.9 is used: G. Marchesini et al., Comp. Phys. Comm. **67** (1992) 465

[70] F. James, 'Monte Carlo theory and practice', Reports on Progress in Physics, **43** (1980) 1145

[71] R. H. Landau, M. J. Páez, 'Computational Physics', Wiley-Interscience (1997)

[72] Al Geist, et al., 'PMV: Parallel Virtual Machine, A User's Guide and Tutorial for Networked Parallel Computing', MIT Press (1994)

[73] http://l3www.cern.ch/homepages/hafeez/computing.html

[74] http://www.asgard.ethz.ch/

Acknowledgements

I am deeply indebted to Prof. M. Pohl, my thesis supervisor, for leading me throughout the work connected to this thesis. I greatly enjoyed the scientific freedom he granted to me, still watching carefully the steps leading to the final success. It was always enlightning to hear his point of view, be it on the deeper insights of physics, be it on the more technical side of the work, be it on matters not related to any of the above.

I would like to thank Prof. H. Hofer for letting me work in his group as a memeber of the L3 team, and Prof. A. Rubbia for his review of this thesis.

One person, I'd like to particularly express my gratitude is Dr M. Fabre. From him I have learned the 'nooks and crannies' of L3, in particular of the muon chamber system. He was the one who has shown to me how to get the best out of a detector, and that the complicated device, such as a high energy physics detector, in not necessarily beyond understanding. Lots of the knowledge I needed for the work in the L3 online group I learned from him. I would also like to thank him, as well as Dr A. Robohm, for allowing this impossible person in their office. The final game of chess, in which I will win against the latter, is still to be played.

It was particularly pleasant to work in the ETH group at CERN. The very nice atmosphere was provided by all its members, but of all of them, I'd like to mention Dr V. Brigljevic, who was actually the first person to introduce me to the world of CERN and L3, still during my diploma thesis. Thanks a lot, and also for finding bugs in my vertex code (gee - that's a hard one to admit).

Working on a stubborn piece of hardware like the muon trigger, requires quite a lot of patience and some knowhow. My thanks for the latter goes to Dr B. Smith and Dr T. Dai, who have introduced me to the field of trigger electronics and the L3 muon trigger in particular. Clearly, to understand the trigger is a small part of the story. I would like to thank Prof. J.J. Blaising and Prof. C. Luci for sharing their knowledge about the L3 online system with me.

A very special 'thank you' goes to my girlfriend Heidi, for her patience (which was needed!), understanding (sometimes) and moral support (always). I would like to thank all my friends I met here in Geneva - Dario, Antonio, Mimmo, Luca, Stève, Christian, André, Tim, all the Michaels, Harald - just to name a few, who made the time here so great.

107

Seite Leer /
Blank leaf

Curriculum Vitæ

- born the 25th of December, 1969 in Warsaw, Poland

- 1976-1981 Primary School in Warsaw

- 1982-1985 Secondary School in Herisau, Switzerland

- 1985-1990 High School in Trogen, Switzerland

- 1990-1996 Physics studies at the ETH in Zürich, Switzerland

- 1994-1995 Exchange student at King's College, London, UK

- 1996-2000 Ph.D. student at ETH Zürich